Initial Design and Simulation of a Portable Breast Microwave Detection Device

Gabrielle Fontaine

A thesis submitted to the Faculty of Graduate Studies of

The University of Manitoba

In partial fulfillment of the requirements of the degree of

Master of Science

Department of Physics and Astronomy

The University of Manitoba

Winnipeg, Manitoba, Canada

Abstract

Breast cancer is the most commonly diagnosed cancer and the leading cause of cancer death for women in Canada. Access to breast cancer screening is limited in northern and First Nation communities in Canada, as well as low- and middle-income countries (LMIC) in the broader international community. Lack of accessible screening tools contribute to inequitable care and increased mortality rates. Microwave breast detection has shown promising results as a safe, low-cost breast cancer screening method. This thesis aims to design and simulate a portable microwave device suitable for use in remote and low-income areas. The device features a cylindrical array of patch antennas and, through machine learning, will require no trained personnel to operate or obtain a preliminary diagnosis. Tiny vector network analyzers were used to measure S-parameters from 0.7 - 3 GHz. A basic radar model was improved to incorporate spherical spreading, microwave attenuation, and secondary scattering. This radar model was used to simulate S_{11} sinograms of dual rod models. The rod models consisted of two point scatterers with assigned reflectivities of 100% & m% or m% & m%, where m was varied as: 10%, 30%, 50%, 70%, and 90%. The simulated sinograms were used to train a convolutional neural network to locate the rod responses. The network was able to easily detect and locate the 100% rod response, but struggled with the lower 10% and 30% reflectivities. The 100% and 90% rod models performed with an accuracy of 92%. The use of machine learning improved upon conventional reconstruction methods for breast microwave radar. Similar machine learning techniques can be performed on real scans with shell-based breast phantoms. The radar model simulations can be used to increase the data set size and improve training performance through transfer learning. Microwave sensing and machine learning methods offer promising possibilities to breast cancer screening accessibility for women in remote and low-income areas.

Contributions

The following are the primary contributions presented by the author in this thesis:

- Design and assembly of a portable, compact microwave sensing device. The device uses 3D printed materials to fasten and hold twenty-six patch antennas each connected to their own tiny vector network analyzer.
- Evaluation and characterization of antenna S-parameters, including quantifying the antenna coupling to determine the optimal spacing between antennas and monitoring responses in the time domain of copper rod reflections.
- Improvements to a radar model simulator though the addition of spherical wave propagation, microwave attenuation, and secondary scattering.
- Generation of time-domain sinograms from numerical rod models with the following reflectivities, m% & 100% or m% & m%, where m was varied as: 10%, 30%, 50%, 70%, and 90%.
- Training and testing of a convolutional neural network to locate rod responses from time-domain sinograms for the different reflectivity combinations.

Acronyms

ADAM Adaptive Moment Estimation. i, 10, 61, 64, 66

AI Artificial Intelligence. i, 11, 54, 55

CNN Convolutional Neural Network. i, x, 56, 60, 61, 63

DAS Delay-and-Sum. i, xi, 8, 12, 13, 16, 34, 35, 43, 49, 51, 52, 74, 75, 76, 77, 78, 79, 80, 81

ECC Envelope Correlation Coefficient. i, ix, 20, 26, 32, 75

FN False Negative. i, 65

FP False Positive. i, 65

ICZT Inverse Chirp Z-Transform. i, 7, 23, 35, 39, 41, 45, 58

KLD Kullback-Leibler Divergence. i, 60, 66, 83

LMIC Low and Middle-Income Countries. i, ii, 15, 17, 80, 82

MAE Mean Absolute Error. i, x, 68, 70, 83

MBI Molecular Breast Imaging. i, 2, 13, 15, 74

MRI Magnetic Resonance Imaging. i, 2, 13, 15, 54, 74

MSE Mean Squared Error. i, viii, 55, 64, 68, 72, 83

MWT Microwave Tomography. i, 6, 12

NanoVNA Nano Vector Network Analyzer. i, 19, 21, 23, 24

PET Positron Emission Tomography. i, 54

ReLu Rectified Linear Unit. i, 9, 60, 63

ROC Receiver Operating Characteristic. i, x, 65, 71

SGD Stochastic Gradient Descent. i, 9, 10

TN True Negative. i, 65

TP True Positive. i, 65

VNA Vector Network Analyzer. i, ix, 5, 16, 18, 19, 21, 23, 27, 31, 32, 44, 54, 74, 75, 76, 81, 82

Acknowledgments

I would like to thank Dr. Stephen Pistorius for acting as my supervisor during my B.Sc. and M.Sc. at the University of Manitoba. Through his guidance and expertise I was able to navigate my research and determine the optimal approach to various problems. Throughout the years he has shaped me to be a great researcher, student, and leader.

I would like to thank my colleagues in the lab who have helped with my project along the way. Sincerest gratitude to Tyson Reimer who created open-access codes which were necessary to my project and provided his expertise and wisdom for this research. I thank Jordan Krenkevich for his valuable assistance and encouragement throughout my degrees.

Sincerest thanks to Sangeev Selvaratam for his help in developing the 3D-printed materials which provided me with many possibilities while designing the physical device.

Lastly, I would like to thank my friends, family, and partner Michael Shepit, for their continuous support and encouragement over the past few years, without whom I would not be where I am today. Special thanks to my father, the late Vince Fontaine, whose love and support motivates me every day.

Contents

List of Tables

List of Figures

1. Introduction

1.1 Background and Motivation

Breast cancer is a global problem affecting millions of people yearly [1]. Access to breast cancer screening is limited in low- and middle- income countries (LMIC) [2–4]. While approximately 50% of breast cancer cases occur in LMIC, they account for 62% of mortality rates [5]. Limitations on early detection resources in LMIC result in late stage diagnosis, and the survival rate of breast cancer is approximately 57% in LMIC compared to 73% in developed countries [5]. Currently, x-ray mammography is the most widely used breast cancer detection method [6]. However in LMIC, mammograms are not performed often because of the public healthcare system limitations, prohibitive cost, overall accessibility to health services, and difficulty in implementing follow-up tests. Because of these difficulties, tumours are often large and palpable at the time of diagnosis.

In Canada, it is estimated that 28,600 women will be diagnosed with breast cancer in 2022 [7]. Over the years, mammography screening uptake and availability have reduced women's mortality rates [8,9]. However for women of lower socioeconomic status, poor access to mammography has resulted in higher mortality rates. In Manitoba, it is estimated the uptake of mammography for First Nation women is 62.8% compared to 86.0% for rural Manitoba women of the same age [10]. Studies in Ontario have shown survival rates for First Nation women on reserves are poorer than those off-reserve, likely due to late-stage diagnoses [11].

Mammography uses ionizing x-rays to irradiate the breast and measure contrast in attenuation. This method is commonly used, but it has disadvantages and limitations. Its use of ionizing radiation poses a health risk to patients, and so the age requirement and frequency of scans are limited to balance the risks and benefits. In Canada, it is recommended women aged 50-74 receive a mam-

mography every two to three years [12]. Mammography has a typical sensitivity of 63 - 95% [5], but sensitivities down to 48% are associated with high-density breasts [8]. Other factors such as poor positioning, incorrect interpretations, slow-growing tumours, and obscure lesions affect the detection accuracy. Approximately 10-30% of breast cancer cases are not detected with mammography [8]. Additionally, mammography uses fragile equipment, is relatively expensive, and needs highly trained personnel to operate.

Other breast imaging modalities include magnetic resonance imaging (MRI), molecular breast imaging (MBI), and ultrasound. MRI uses strong magnetic fields instead of ionizing radiation to image the body. Specifically, MRI applies nuclear magnetic resonance techniques to measure proton density and relaxation parameters allowing for obvious contrast within soft tissues. This modality has an increased sensitivity to detection and is primarily used to screen high-risk women, such as those with high-density breasts [13]. MRI has a good sensitivity, however its poorer specificity results in higher false positives [1]. The high cost, large size, slow acquisition time, and low specificity makes it unsuitable for breast cancer screening in the general population.

MBI uses radioactive material to detect metabolically active cells within the breast. After the injection of a radioactive tracer, the breast is placed between detectors with light compression. MBI has a similar sensitivity and specificity to MRI, but the use of ionizing radiation poses health risks similar to mammography [8]. For high-risk women, MBI may be used if the patient cannot undergo MRI.

Ultrasound is a low-cost and relatively compact modality typically used as a primary or secondary screening tool in addition to mammography. It may be used as the primary screening tool for women who are younger, lactating, or pregnant [8]. As a secondary screening tool ultrasound is typically used for women of high-risk groups. Additional screening may increase detection sensitivity but also decrease specificity due to increased false positives [1]. Also, ultrasound requires highly skilled personnel to operate and interpret the images. The disadvantages in mammography, MRI, MBI, and ultrasound make it challenging to use these devices in remote and low-income

areas. Existing challenges with implementing safe, low-cost breast cancer screening methods have motivated the design and development of a portable breast microwave detection device.

1.2 Breast Microwave Sensing

Research dedicated to breast cancer detection is continuously advancing [14]. Challenges with current methods have prompted exploration into breast microwave sensing. The use of microwaves has many advantages, including the relatively low cost and lack of ionizing radiation allowing for safe and frequent screening. The type of sensing equipment, measurement protocol, and reconstruction/detection method can vary [15]. Optimizing these variables is crucial in providing a safe, efficient, and accurate screening method for breast cancer.

1.2.1 Terminology and Methods

Microwave sensing has shown promising results as a safe and low-cost breast cancer detection modality [16]. This screening process measures reflected and/or transmitted microwave signals penetrating the breast. The scattering interactions of the microwave signals can be determined from the dielectric properties. For breast microwave detection, cancerous and healthy tissues differ in their complex permittivities, allowing for the distinction and detection of tumours.

The relative complex permittivity ε_r describes the electric polarizability of a material,

$$\varepsilon_r = \frac{1}{\varepsilon_0}\left(\varepsilon' - j\frac{\sigma}{\omega}\right) \tag{1.1}$$

where ε_0 is the permittivity of free space, ε' is the dielectric constant of the material, σ is the conductivity, and ω is the angular frequency of the microwave. We can rewrite this as a real, ε_r', and imaginary term, ε_r'',

$$\varepsilon_r = \varepsilon_r' + j\varepsilon_r''. \tag{1.2}$$

The predominant healthy tissues in the breast are skin, adipose, and fibroglandular tissue. The dielectric properties of the different breast tissues vary due to water content differences and the microwave frequency. Initially, the dielectric contrast between healthy and cancerous tissues was reported to be 10:1 [17]. This generated enthusiasm for breast cancer detection, suggesting tumours may be distinguished with higher accuracy than mammography, particularly for denser breasts. Recent studies have confirmed this high contrast between malignant and adipose tissue. However the contrast between malignant and fibroglandular tissue is approximately 10% [17].

The complex relative permittivity of tissues can be simulated with the Debye model:

$$\varepsilon_r = \varepsilon_\infty + \frac{\varepsilon_s - \varepsilon_\infty}{1 + j\omega\tau} - j\frac{\sigma}{\omega\varepsilon_0} \tag{1.3}$$

where ε_∞ is the permittivity of the tissue, ε_s is the static permittivity of the tissue, and τ is the relaxation time of the medium. This model may be used to estimate the dielectric properties of different breast tissues.

Clinical studies with human subjects provide realistic testing and validation of breast microwave sensing. However, before clinical trials are implemented, numerical simulations or physical breast phantoms may be used to examine the system's performance. Ideally, these phantoms should mimic the morphology and dielectric properties of the breast. The primary healthy tissues within the breast include adipose tissue and fibroglandular tissue. Early physical phantoms were simple and consisted of homogeneous cylinders that did not accurately represent the morphology or dielectric properties of the breast [18]. Advancements in breast phantom material and manufacturing have allowed for phantoms with improved morphology and dielectric properties [19–21]. Solid, gel, or shell-based phantoms have been developed to describe the various tissues within the breast. In addition to accurately representing the tissue types, the phantoms must also appropriately vary in breast size, breast density, tumour size, and tumour type.

1.2.2 Equipment and Design

Microwave sensing requires various equipment to enable measurements of the breast. While designing, the microwave sensor, sensor array, size, and configuration are variable [14]. Vector network analyzers (VNA) are often connected to antennas to supply and measure the microwave signals. The VNAs measure the scattering parameters (S-parameters) that describe the reflected or transmitted responses. We can define the incident waves as **a**, and the reflected waves as **b**. If we assume a 2-port system we can initially assume port 1 is stimulated by the incident wave and port 2 is not, i.e., $a_1 \neq 0$, $a_2 = 0$. The reflection incident at port 1 (S_{11}), and transmission at port 2 (S_{21}) can be described as follows:

$$S_{11} = \frac{b_1}{a_1};\ S_{21} = \frac{b_2}{a_1}. \tag{1.4}$$

Conversely, we can consider the case where port 2 is stimulated by the incident wave such that $a_1 = 0$, $a_2 \neq 0$. The transmission incident to port 1 (S_{12}), and reflection to port 2 (S_{22}) can be described as followed:

$$S_{12} = \frac{b_1}{a_2};\ S_{22} = \frac{b_2}{a_2}. \tag{1.5}$$

In general, we can obtain the S-parameters matrix **S** from the wave vectors **a** and **b**:

$$\begin{pmatrix} b_1 \\ b_2 \end{pmatrix} = \begin{pmatrix} S_{11} & S_{12} \\ S_{21} & S_{22} \end{pmatrix} \begin{pmatrix} a_1 \\ a_2 \end{pmatrix} \tag{1.6}$$

$$\mathbf{b} = \mathbf{Sa} \tag{1.7}$$

During a measurement, the VNAs may sweep through a range of frequencies to measure the S-parameters. The frequencies used in breast microwave sensing typically range between 0.5 - 10 GHz. The type of antenna may vary. Some common types include monopole, Vivaldi, horn, and patch antennas. These antennas may be used in monostatic, bistatic, or multistatic modes [16]. Monostatic systems incorporate one antenna and one port, only measuring S_{11} values. Bistatic

systems use two antennas, a two-port system, and can measure S_{11}, S_{21}, S_{12}, and S_{22} values. Lastly, multistatic antennas can include any number of antennas and measure a wide range of reflection and transmission S-parameters.

Device designs may also vary, most operating in a circular configuration. To achieve this, the antenna arrays may be stationary or require moving parts [15]. Synthetic arrays can be created by rotating the transmitting and/or receiving antennas in a circular pattern. Fully stationary devices include multiple antennas fixed in an array. Mixed systems do not rotate the individual antennas, but may rotate or shift the entire array. Incorporating a rotational component allows for sampling at a finer angular resolution, but increases the complexity and cost of the device. Devices may operate in open air or in a coupling medium. A coupling medium, such as a water-glycerine mix, can reduce unwanted reflections at the skin interface but also increases microwave attenuation due to higher conductivity values [22]. The configuration of the sensing device may vary to elaborate designs. For example, McGill University has developed a wearable hemispherical shell that contains many antennas to detect scattered signals [23]. This is advantageous as the antennas are attached close to the skin.

1.2.3 Image Reconstruction

There are currently two approaches for microwave imaging that are widely researched: microwave tomography (MWT) and microwave radar. Numerical phantoms [24, 25], physical phantoms [22, 26], and human subjects [27, 28] have been used to test MWT systems. MWT uses the transmitted signals to reconstruct complex permittivity maps of the object in question. This method may be categorized as using a single frequency or multiple frequencies. In MWT, the forward problem models the total electric field as a sum of the incident field and scattered field. The object function is described as the dielectric contrast between the scatterer and the background. MWT aims to solve this non-linear inverse scattering problem.

Approximations, such as the first-order Born approximation, can be used to create a linear

problem [29]. Physically, this approximation assumes the scattered field is negligible compared to the incident field, and so the scattering object and contrast must be small compared to the background. These approximations are not accurate for large regions of heterogeneous permitivities, and so non-linear solutions may be needed. This poses challenges as no unique solution exists and the solution may be unstable.

Radar-based imaging has been widely researched and tested with simulations [30, 31], breast phantoms [32–35], and human subjects [36, 37]. This method uses electromagnetic scattering to find reflection maps based on the scatterer's dielectric properties and radar cross-section. Typically, a microwave source is used to illuminate the breast with ultra-wideband signals and the S_{11} signals (or other S-parameters) are detected. The $S_{11}(f)$ in the frequency domain can be converted to the time domain $S_{11}(t)$ through the inverse Fourier transform. In this work, the inverse chirp-z transform ICZT was used [38].

$$S_{11}(t_k) = \sum_{n=0}^{N-1} S_{11}(f_n) A^{-n} W^{nk} \tag{1.8}$$

$$A = exp\Big(\frac{-2\pi j t_0 f_0}{N}\Big) \;\; ; \;\; W = exp\Big(\frac{-2\pi j (t_{M-1} f_{M-1} - t_0 f_0)}{N^2}\Big) \tag{1.9}$$

where f_{M-1} is the stopping frequency, f_0 is the starting frequency, and N is the total number of frequency points, allowing the array of frequencies to be described as,

$$\{f_{start}, \ldots, f_{stop}\} = \{f_0, \ldots, f_{N-1}\}. \tag{1.10}$$

And similarly, the total number of time points, M, can describe the times as,

$$\{t_{start}, \ldots, t_{stop}\} = \{t_0, \ldots, t_{M-1}\}. \tag{1.11}$$

The ICZT allows for the transformation from a fixed number of frequency points, N, to an arbitrary number of time points, M. The same transformation may be used for other S-parameters if a

multistatic system is used.

The time-domain reflected signals are processed with a beamformer to determine high scatter locations. A common beamformer is the delay-and-sum (DAS) beamformer [39]. This method estimates the time delay from each antenna to a position within the breast by assuming straight-line propagation and an average propagation speed. Typically, the average propagation speed is estimated from the average dielectric properties of the breast at the centre frequency of the microwave bandwidth. In a monostatic system, an intensity profile I is created by summing and squaring the time responses associated with a point $\mathbf{r_0}$ within the breast:

$$I(\mathbf{r_0}) = \Big(\sum_{m=1}^{M} x_m(t_m(\mathbf{r_0})) \Big)^2 \tag{1.12}$$

where M is the total number of antennas, x_m is the radar signal from the m^{th} antenna position, and $t_m(\mathbf{r_0})$ is the time delay to and from antenna position $\mathbf{a}$ to position $\mathbf{r_0}$,

$$t_m(r_0) = \frac{2|\mathbf{r_0} - \mathbf{a}|}{v}, \tag{1.13}$$

where v is the estimated propagation speed. Most beamformers are an extension of the DAS beamformer. For example, the delay-multiple-and-sum beamformer involves pair-wise multiplication of the radar signals [40], and the improved-delay-and-sum beamformer incorporates positional dependant weights into the intensity values [41]. These beamformers do not account for the physics of microwave propagation and antenna properties. More advanced beamformers may incorporate microwave attenuation and time delay errors [16].

1.2.4 Machine Learning

In recent years, machine learning has shown exciting potential for medical image restoration, segmentation, and analysis applications [42–45]. Current research has focused on automated microwave detection that determines the presence or absence of a tumour through artificial intel-

ligence (AI) based machine learning [46–48]. This process does not reconstruct permittivity or reflection maps but instead trains a machine learning network to detect, classify, and/or locate a breast abnormality.

A convolutional neural network is a class of neural network used for machine learning [49]. This type of network incorporates convolutional layers that are most commonly used to analyze and extract image features. The neural network can be trained to reproduce a specific output when given the corresponding input. The convolutional neural network consists of an input layer, an output layer, and multiple hidden layers. In a hidden layer, the network takes an input X and produces an output Y through a function F,

$$Y = F(X, W) \tag{1.14}$$

where W is a weighted vector representing the strength of interconnection between the input and output neurons. In supervised learning, the weighted vector W is optimized by training the network with multiple XY pairs. The optimization process consists of two elements; the loss function and the optimizer. The loss function compares the neurons from the output layer to the ground truth neurons. The optimizer adjusts the weights of each hidden layer to minimize the loss function.

Common hidden layers may include convolutional, dense, drop-out, and activation [50]. Convolutional layers convolve the input with a filter and pass the result to the next layer. The filter size can be varied, while the values of the filter, known as *weights*, are adjusted during training. Dense layers connect every neuron in the input layer to every neuron in the output layer by adjustable weights. Drop-out layers are used to reduce the weights of randomly selected neurons to zero or close to zero. The random drop of neurons can help reduce noise within the network. Activation layers are used to filter each neuron in the layer. Common examples of filters are rectified linear unit (ReLu); $f(x) = max(0, x)$, sigmoid; $f(x) = 1/(1 + e^{-x})$, and softmax; $f(x) = x/\sum_i(x_i)$.

Training optimizers use stochastic gradient descent (SGD) to adjust the weights within the

hidden layers. SGD optimizers seek to minimize the loss function, which has the form of a sum,

$$L(w) = \frac{1}{n}\sum_{i}^{n} L_i(w) \tag{1.15}$$

where the overall loss function, L, sums over each loss between the prediction ith neuron and ground truth neuron. The SGD method minimizes the loss function by performing the following iterations,

$$w := w - \frac{\eta}{n}\sum_{i}^{n} \Delta L_i(w) \tag{1.16}$$

where η is the learning rate of the machine learning process. In SGD, the true gradient of L(w) is estimated by taking the gradient at a single neuron. For advanced training, adaptive learning rates, such as the adaptive moment estimation (ADAM) optimizer, can be used. ADAM uses estimations of first and second moments of gradient to adapt the learning rate for each weight of the neural network [51]. This helps speed up convergence of minimizing the loss function and improve upon network training.

While training, the network performance may be evaluated with an independent XY validation set. The loss values from the training and validation sets may be monitored to determine if under- or over-fitting is present. Under-fitting refers to the networks inability to accurately describe the problem. Over-fitting occurs when the model attempts to fit irrelevant noise during training. If no under- or over-fitting is present, the loss values of the two sets should follow the same pattern. If under-fitting is present, the loss values will not converge to a minimum. If over-fitting is present, then the training loss will decrease to a minimum, while the validation loss increases. Training may be stopped early if over-fitting starts to occur, therefore ensuring the network weights are optimized without fitting to noise. Additionally, drop-out layers, lower learning rates, or regularization parameters may be used to address over-fitting.

For small training sets which may be insufficient for network training, transfer learning may be used to train the network. Traditional machine learning recognizes patterns from training sets

and uses that to predict outputs. Transfer learning has been shown to improve traditional methods through the transfer of knowledge from a related task that has already been learned [52]. Instead of training a blank network, transfer learning uses patterns from a network that has been trained with a similar problem. Weights within the previously trained network may be frozen while the rest are optimized with the smaller training set. For imaging purposes, analytical simulations may be used to initially train the network to perform image reconstruction. From here, real scans can train the partially frozen network to reconstruct the images. Analytical imaging data can supplement physical scans to improve AI image reconstruction through transfer learning.

1.3 Microwave Groups

There are numerous groups currently researching different techniques for breast microwave sensing. For these groups, the type of antenna, number of antennas, operating frequency range, configuration, measurement protocol, and signal processing approaches vary. Some examples of microwave tomography groups include:

- **Dartmouth College** [28, 53, 54]: A cylindrical array of 16 monopole antennas has been developed. One antenna acts as the transmitting antenna while the remaining 15 act as receivers. The device is submerged in a coupling medium consisting of water and glycerine. Scans are performed between 0.5 - 3 GHz and can operate in a 2D or 3D mode. Previously, images were reconstructed using the finite-difference time-domain (FDTD) algorithm. However, more recently, the discrete dipole approximation has been employed to reduce computational time. The system is currently in clinical trials and has been evaluated on over 500 human subjects.

- **Keele University** [55, 56]: Cylindrical array of 24 open-ended waveguides has been developed. One antenna acts as the transmitter while the remaining 23 act as the receiver. Through a switch, each antenna can act as the transmitter. The system operates from 1.0 - 2.3 GHz.

The chamber is filled with a matching solution of fatty liquids and salt. This group has introduced 4D functional imaging with three dimensions in the spatial domain and one in the time functional dynamic domain. Testing with animals was performed at the Carolina Medical Centre.

- **Electronics and Telecommunications Research Institute** [26, 57]: This system was inspired by the Dartmouth College system. It incorporates an array of 16 monopole antennas that move vertically to 7 different imaging planes . The imaging tank is filled with a coupling liquid of propylene glycol and distilled water. A microwave switch controls which antenna acts as the transmitter while the remaining 15 act as receivers. Scans are performed from 0.5 - 3 GHz. Images are reconstructed with the FDTD algorithm in a limited imaging zone to reduce computational time. Results have been published with phantoms and small animals.

- **University of Manitoba** [58–61]: Two-dimensional and three-dimensional systems have been developed and evaluated. The 2D system features a cylindrical array of twenty-four antennas. Experimental measurements were performed with human forearms from 0.8 - 1.2 GHz. The 3D system uses twelve Vivaldi antennas fixed in a middle cylindrical array and 120 probes along upper, middle, and lower cylindrical arrays. Deep-learning techniques have been investigated to remove artifacts and improved the quality of the reconstructed images.

MWT has proven to be a well-rounded and accurate reconstruction method. However, the computational time can be long, so research groups have focused on reducing the complexity of the reconstruction. Microwave radar too has shown promising results with experimental and clinical work. Some examples of microwave radar groups include:

- **Bristol University** [62, 63]: A semi-spherical system that incorporates 60 antennas has been developed. The antenna system uses a fitting cup to connect with the breast. A paraffin coupling medium is used between the antennas, fitting cup, and the breast. The system operates in the 4 - 8 GHz frequency range. A DAS beamformer is used to reconstruct images. Testing with human subjects has been performed with this device.

- **University of Calgary** [37, 39, 64]: This system uses a single Vivaldi antenna to perform monostatic radar. Canola oil is used as a coupling medium. The system rotates to collect measurements along a cylindrical plane. Measurements are performed with a frequency range from 50 MHz - 15 GHz. The reconstruction algorithm estimates the skin response and reconstructs the intensity within this region through the DAS beamformer. Results from 8 patients have been reported.

- **McGill University** [23, 65, 66]: A clinical prototype of a wearable microwave radar system has been developed. The semi-spherical system includes 16 flexible monopole antennas. Time-domain measurements are recorded using an oscilloscope instead of frequency measurements. The system has been assessed on multiple patients over an 8-month period.

- **University of Manitoba** [67–69]: Monostatic radar system with a single horn antenna has been developed. The antenna rotates to 72 positions along a cylindrical plane. The system operates in the 2 - 9 GHz frequency range. An iterative DAS beamformer is used to reconstruct images. This Health Canada Licensed device has been evaluated with MRI-derived shell-based breast phantoms and eight volunteers.

Microwave radar has progressed far in terms of experimental work. However, the method itself does not to incorporate the physics of microwave propagation and equipment parameters. Recently, some groups have tried to bridge the gap between tomography's complexity and radar's simplicity [69, 70].

1.4 Thesis Question

Current imaging modalities for breast cancer include x-ray mammography, MRI, MBI, and ultrasound. However, these methods have many limitations that prevent the development of portable devices. This includes high equipment cost, large size and infrastructure, health risks, and the need

for trained personnel to operate and obtain a preliminary diagnosis. A portable microwave sensing device may be designed and developed to address the issues of current imaging modalities.

Hypothesis: Advances in microwave and machine learning technologies can be harnessed to create an early breast cancer detection device that is suited for use by women in remote and low-income locations.

This research project aims to design, develop, and evaluate a portable breast microwave detection device suitable for use in remote locations and LMIC. The feasibility of machine learning reconstruction will be monitored for different contrasts in rod materials. Information from this may be used to modify and optimize the performance of the physical device to enable future measurements of more complex phantoms. This thesis has three key objectives:

- The design, construction, and testing of a small microwave-based breast cancer detection device (Chapter 2).
- The simulation of time-domain S_{11} data to mimic the parameters of the physical device (Chapter 3).
- The training and testing of a machine learning network to locate rod responses from numerical rod phantoms (Chapter 4).

2. Designing and Characterizing a Portable Microwave Device

2.1 Introduction

In Canada, it is estimated that 1 in 8 women will be diagnosed with breast cancer in their lifetime, a condition more easily treated if detected in its early stages [7]. Access to early breast cancer detection is limited in northern communities in Canada [10] and LMIC in the broader international community [5]. Although the relative incidence of breast cancer is currently lower in LMIC, the lack of access to breast cancer screening in these areas results in inequitable care and disproportionately high mortality rates for women that will worsen as the incidence rates increase [5].

Current breast cancer screening methods include x-ray mammography, MRI, MBI, and ultrasound [8]. These modalities are of high cost, large size, incorporate fragile equipment, use ionizing radiation, and/or require trained personnel to work. These disadvantages make current modalities difficult to bring to low-income and remote areas. This has prompted research into alternative methods for breast cancer screening. Specifically, breast microwave sensing has shown encouraging results as a small, safe, and low-cost modality.

Different microwave methods have been evaluated with numerical simulations [24, 30] and breast phantoms [32–34], with some progressing to human trials [53]. The reconstruction style, configuration, measurement protocol, and equipment vary between research group. Common designs include a cylindrical array of antenna positions that individually measure reflections and/or transmissions within the breast. These arrays may be synthetically created through a rotational

component or physically created with a stationary array. Microwave groups operate their systems using different bandwidths with most in the range of 0.5 - 10 GHz.

Microwave tomography and radar imaging lie on opposite ends of the spectrum, with microwave tomography incorporating the full electromagnetic model and radar simplifying to a model that does not to incorporate the physical aspects of microwaves and the equipment. An optimal system can be created by bridging the gap between the inaccuracies of radar and the complex computational requirements of tomography. It has been shown that an iterative DAS beamformer can be modified to incorporate the physics of antenna gain, beam pattern, and VNA characteristics [68, 69]. This improves upon the traditional DAS beamformer and further research can implement other properties of antennas, VNAs, and microwaves. Machine learning techniques may also improve upon current detection methods. With this process, a machine learning network can be trained to effectively and accurately detect breast abnormalities by incorporating physical aspects of microwaves and the device.

This chapter focuses on designing and characterizing a portable microwave system that may be used for early detection in remote and low-income areas. The device uses low-powered non-ionizing radiation, is small and compact, and will require no trained personnel to operate. It features a cylindrical array of patch antennas operating in the 0.7 - 3 GHz range. The coupling between adjacent antennas was quantified for varying antenna spacings to identify the optimal number of antennas. The ideal number of antennas was found by minimizing the unwanted coupling while maximizing the angular sampling.

Additionally, copper rod measurements were performed to monitor the time domain responses. To estimate the antenna cable time delay and propagation speed, measurements of S_{11} reflections in the time domain were performed for varying distances between the antenna and the copper rod. Further characterization, calibration, and testing of the device will allow for a complete set of measurements to be taken with breast phantoms. These measurements may then be used in a machine-learning algorithm to automate breast abnormality detection and allow for the device's

portability. As a result, women in LMIC and remote areas may have improved access to breast cancer screening through the design, characterizing, and testing of a portable microwave device.

2.2 Methods

A portable microwave detection device was designed to address current issues with breast cancer screening accessibility. While designing the device the following aims were considered:

- The overall size, weight, and cost of the device should be minimized.
- The chamber of the device should be sized so that it may scan large breasts.
- The device should have no rotational components to reduce complexity and cost.
- Machine learning will be used to automate the response to the presence or absence of a breast abnormality.
- The device should feature a user-friendly graphical interface so that the patient can use it on themselves.

The first three aims described in this chapter were achieved through carefully considering the equipment and design of the device. Initial research into the fourth aim is outlined in Chapter 4 through machine learning detection of rod materials. Future research for this aim includes the progression to breast phantoms and, eventually, human subjects. The final aim may be completed in the future through advanced computer technology.

2.2.1 Equipment and Antenna Coupling Minimization

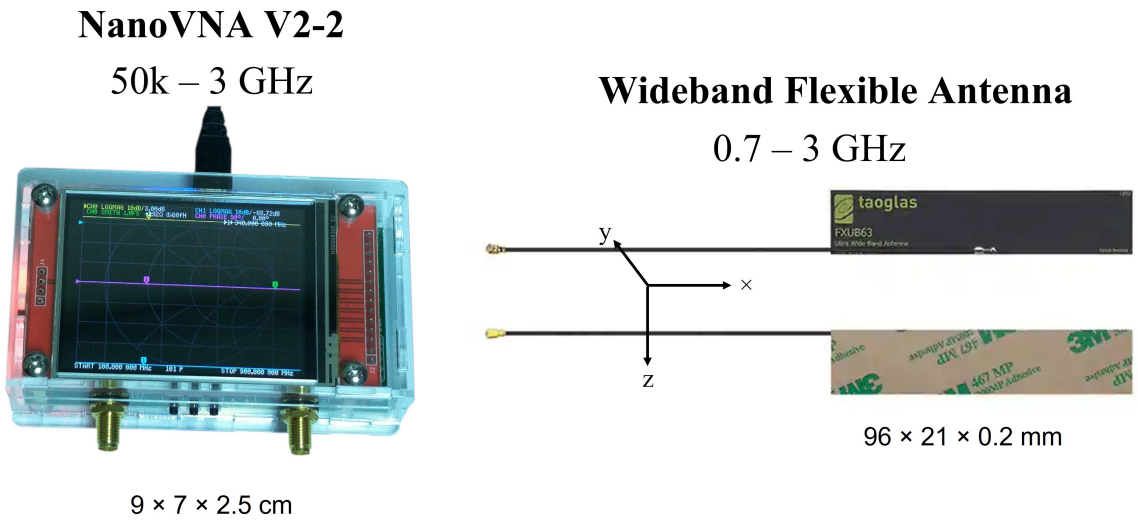

Figure 2.1: Portable device equipment including the NanoVNA V2-2 and flexible patch antennas.

Version	Frequency range	Dynamic range (<1GHz)	Dynamic range (>1GHz)	Sweep Points
NanoVNA-H4	50k - 1.5 GHz	40 dB	40dB	101
NanoVNA V2-2	50k - 3 GHz	70 dB	60 dB	1024
NanoVNA V2 Plus4	50k - 4.4 GHz	90 dB	80 dB	1024

Table 2.1: Specifications of the NanoVNA-H4 [71], NanoVNA V2-2 [72], and NanoVNA V2 Plus4 [72].

The equipment for the portable device was carefully chosen to reduce overall cost, size, and complexity. Tiny compact vector network analyzers (VNA) and flexible wideband patch antennas were selected to construct the device (Fig. 2.1). Initially the NanoVNA-H4 [71] was chosen because of its low cost, compact size, and small weight. This VNA was replaced by the newer version, NanoVNA V2-2 [72]. This version allowed for higher frequency scans with a better dynamic range. Recently the NanoVNA V2 Plus4 [72] was released, opening possibilities for improvements in the future. The specifications of the VNAs are outlined in Table 2.1.

Patch antennas were chosen to transmit and measure the microwave radiation patterns. These

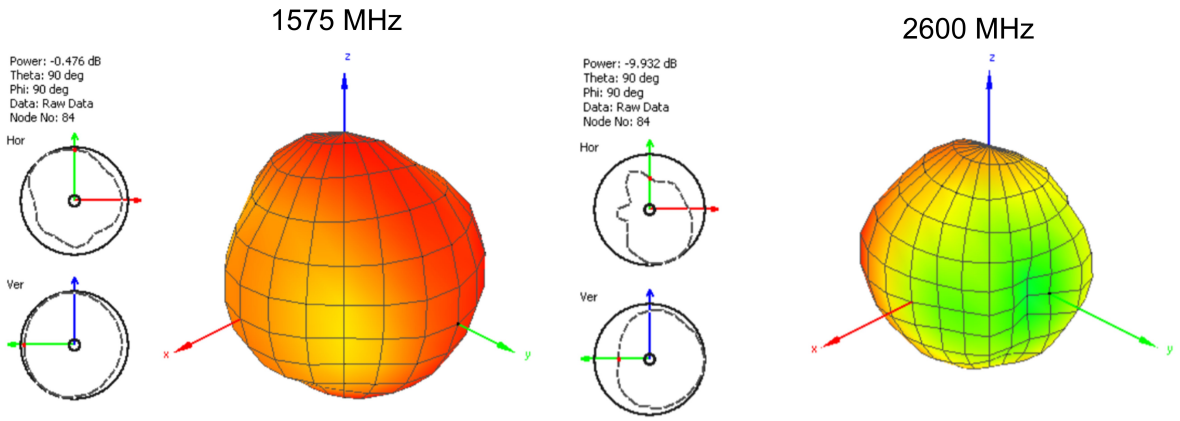

Figure 2.2: Radiation pattern of the patch antennas for 1.575 and 2.600 GHz.

antennas are flexible, rectangular in shape, and can be easily mounted to surfaces. They are 9.6 $\times$ 2.1 $\times$ 0.2 cm and work in the 0.7 - 3 GHz range. The antennas use a mini coaxial cable and U.FL termination. An SMA adapter was used to connect the antenna to the VNA port. The radiation patterns are omnidirectional and reasonably symmetric in the YZ plane. Examples of the radiation patterns for 1.575 and 2.600 GHz are shown in Figure 2.2.

Before the device was designed and assembled, the optimal number of antennas was determined by minimizing the antenna coupling while maximizing the angular sampling. Coupling between adjacent antennas refers to the energy absorbed from one operating antenna to another. This is unwanted as it reduces the antenna's performance and efficiency. The antenna coupling can be reduced by using different radiation patterns, polarizations, or increasing the antenna spacings. On the other hand, it is desirable to place the antennas close together so that more may fit within the device, thus increasing the angular sampling.

To monitor the coupling for various antenna spacings, measurements were taken with the NanoVNA and patch antennas. The two-port system was used to measure S-parameters between two adjacent antennas. The coupling between adjacent antennas was quantified through the Enve-

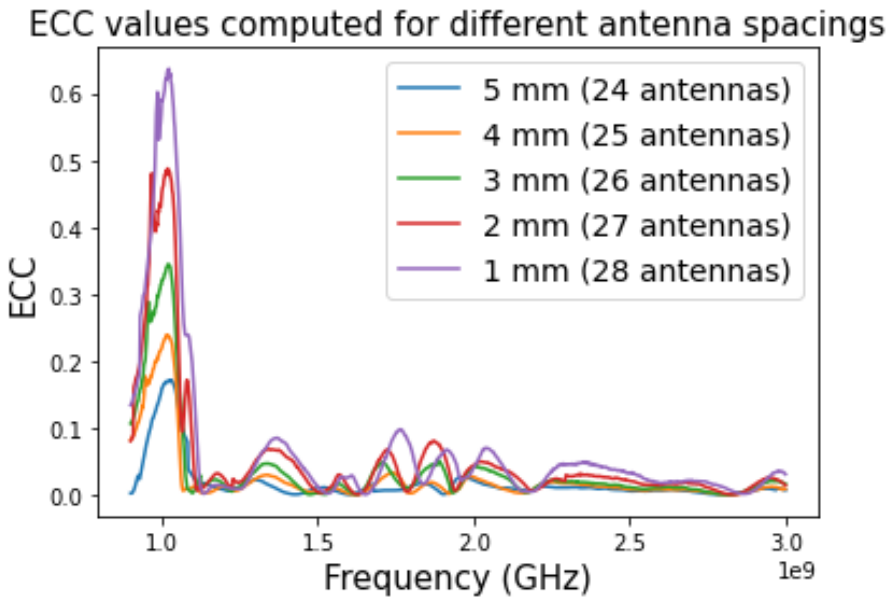

Figure 2.3: ECC values for five different antenna spacings over 700M - 3 GHz. The corresponding number of antennas that would fit in the device was determined for each antenna spacing.

lope Correlation Coefficient, ECC [73]:

$$\mathbf{ECC} = \frac{|S_{11}^* S_{12} + S_{22} S_{21}^*|^2}{(1 - |S_{11}|^2 - |S_{21}|^2)(1 - |S_{22}|^2 - |S_{12}|^2)} \tag{2.1}$$

where S_{11}^* and S_{21}^* are the complex conjugate of S_{11} and S_{21} respectively. S-parameter measurements were performed between two adjacent antennas suspended on graph paper and surrounded by microwave absorbers. The ECC between the two antennas was obtained for eight antenna separations ranging from 1 - 8 mm in 1 mm increments. The number of antennas that would fit within a 20 cm diameter was determined for each antenna spacing.

The ECC was calculated for 1024 frequency points between 0.7 - 3 GHz and reached a peak at 1.02 GHz. Five of these antenna spacings and their corresponding number of antennas are shown in Figure 2.3. At the peak frequency, the normalized ECC values, ρ_n, were plotted as a function of the normalized antenna spacings, d_n. The optimal antenna spacing was found by minimizing the following equation, $\rho_n^2 + d_n^2$. From here, the optimal number of antennas was determined to be twenty-six.

2.2.2 Device Design and Assembly

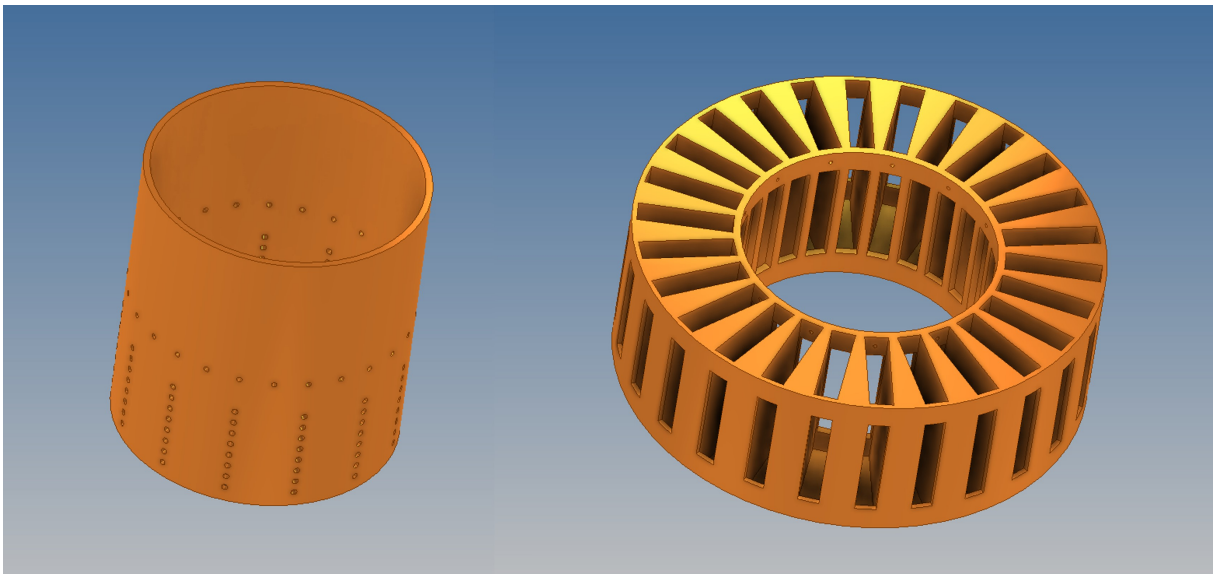

Figure 2.4: 3D printed materials for the physical device consisting of an inner cylinder (left) for scanning and an outer shell (right) to fasten the VNAs.

The overall system was assembled using 3D printed materials, patch antennas, VNAs, absorbers, cables, and a 28-port USB hub. The design consists of a cylindrical array of twenty-six stationary patch antennas each connected to its own NanoVNA. To minimize noise associated with cable motion, the antennas were mounted on the inside of a 3D printed cylinder while the VNAs were fastened into holders that were radially close to the antenna. Each antenna was connected to a NanoVNA, allowing S_{11} reflections to be easily measured. However for future measurements, the power received by the remaining antennas can be recorded, resulting in 26 reflection and 26x25 transmission signals for a single frequency.

The backbone of the device was developed using 3D printed materials made from polylactide thermoplastic (Fig. 2.4). The models were designed using Autodesk Inventor 2022 and sliced for 3D printing using Ultimaker Cura. After the design, the Prusa i3 MK3S was used to print the materials. Two cylinders were created to mount the antennas and fasten the VNAs. The first cylinder has an inner diameter and height of 20 cm and 20 cm respectively. This allows antennas

to be mounted on the inner surface so that scans can be performed radially inwards. The cylinder incorporates twenty-six holes halfway down the length of the material to allow for the antenna cables to pass through. Additional holes underneath are used to fasten the first cylinder to the second at variable heights. The 20 cm diameter allows for breasts larger than a D-cup size to be included.

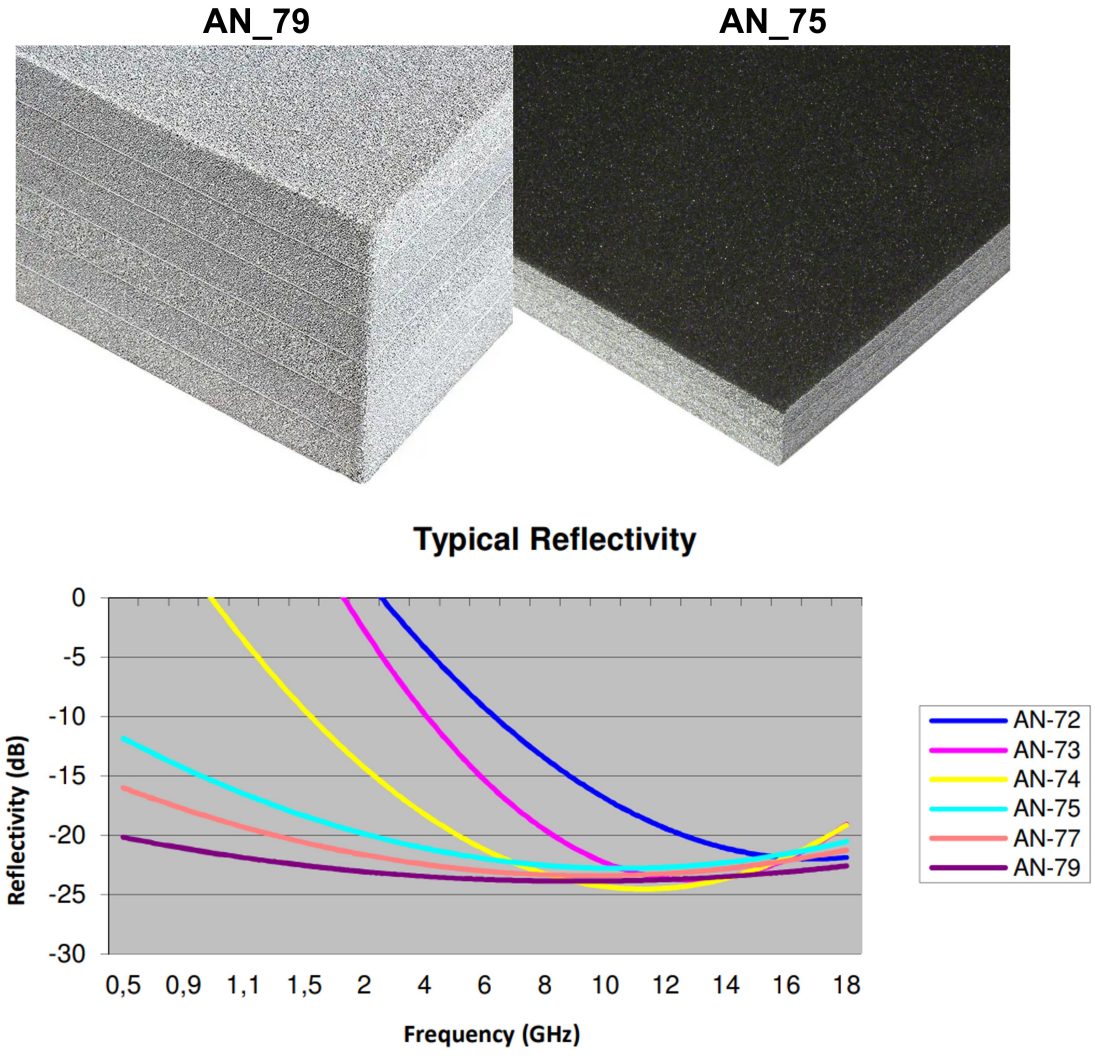

Figure 2.5: Eccosorb absorbers AN-79 and AN-75 incorporated to the physical device to minimize external signals and multiple reflections.

The second cylinder has an inner diameter that corresponds to the outer diameter of the inner cylinder. The outer diameter and height of the second cylinder are 40 cm and 12 cm, respectively. Carved into the cylinder are twenty-six rectangular cavities to hold the NanoVNAs. Beneath each cavity lies an opening for the VNA cables to connect to a USB hub for communication.

Microwave absorbers were chosen to reduce unwanted reflections and external signals. Two Eccosorb radar absorbing materials were incorporated into the device (Fig. 2.5). AN-79 absorbers (11.4 cm thickness) were placed at the bottom of the air chamber to absorb immediate microwaves and scatter towards the bottom. These absorbers have reflectivities smaller than -20 dB for the entire bandwidth. Thinner AN-75 absorbers (2.9 cm) were wrapped into a cylindrical shape so that they may be placed concentrically with the device during a scan. The AN-75 materials absorb poorer than the thicker absorbers, but the reflectivity is lower than -13 dB for the entire bandwidth.

2.2.3 Rod Measurements and Antenna Cable Delay

Individual S_{11} antenna measurements were performed on copper rods. To begin, the VNA port was calibrated with short, open, and load S_{11} measurements from 0.7 - 3 GHz. After calibration, open-air S_{11} values were swept from 0.7 - 3 GHz using 230 frequency points. This was transformed to 101 time points ranging from 0 - 5 ns using the ICZT. For the open-air scans, a significant response occurred due to reflections at the antenna-cable interface (Fig. 2.6). The maximum value from this response provided the time delay and the uncertainty was estimated from the standard deviation of a Gaussian fit. The time location of the response was found to be 1.61(26) ns.

Next, copper rods were placed within the device chamber to measure the responses from a single antenna. For these measurements, the center of the copper rod was placed at the following distances along the Y-axis of a single antenna: 2.5 cm, 5.0 cm, 7.5 cm, 10 cm, 12.5 cm, 15 cm, 17.5 cm, and 19.5 cm. S_{11} values were recorded from 0.7 - 3 GHz for 230 frequency points. Afterwards, the rod was removed and a similar open-air scan was performed. The frequency S_{11} values were transformed to the time domain. In the time domain, the open air and rod scans were subtracted

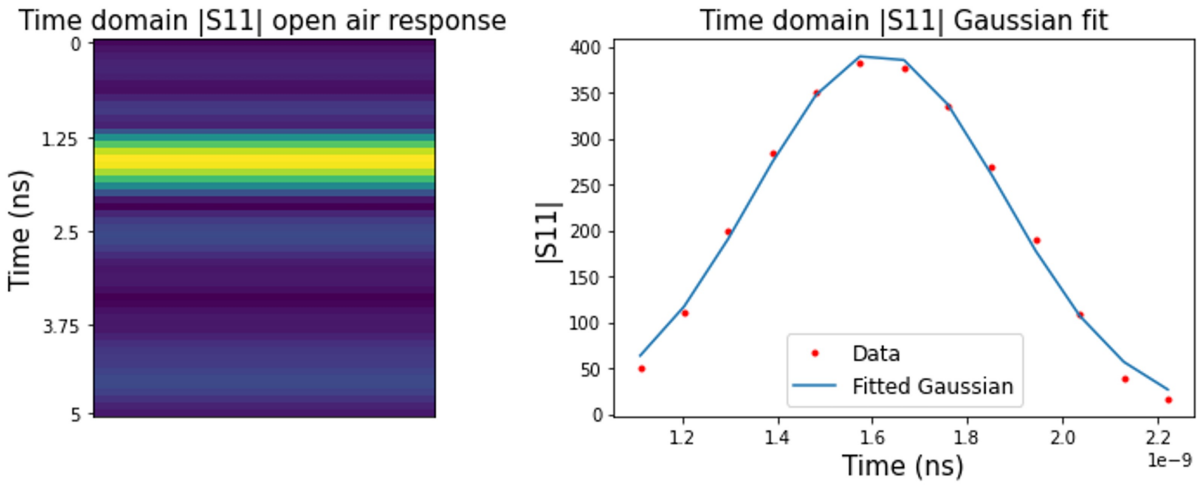

Figure 2.6: Physical open-air S_{11} measurement converted to the time domain and extended along the x-axis. The magnitude of the S_{11} values were fit with a Gaussian curve to estimate the uncertainty in the response.

from each other. From the magnitude of the S_{11} values, the time locations of the rod responses were easily visible.

By varying the distance between the rod and antenna, linear shifts of the rod responses were apparent in the time-domain. In the time domain, the location of the reflected signals were given by the maximum value within the response peak. Each response was fitted with a Gaussian curve. The uncertainties in the distances were given by the radius of the rod (0.5 cm), while the uncertainties in the time responses were given by the standard deviation of the Gaussian fit. The time responses were plotted as a function of rod distances. Weighted linear regression was used to determine the slope and y-intercept of this relationship. The slope allowed the microwave propagation speed to be calculated. The y-intercept estimates the total time delay between the NanoVNA port and transmission plane.

2.3 Results and Discussion

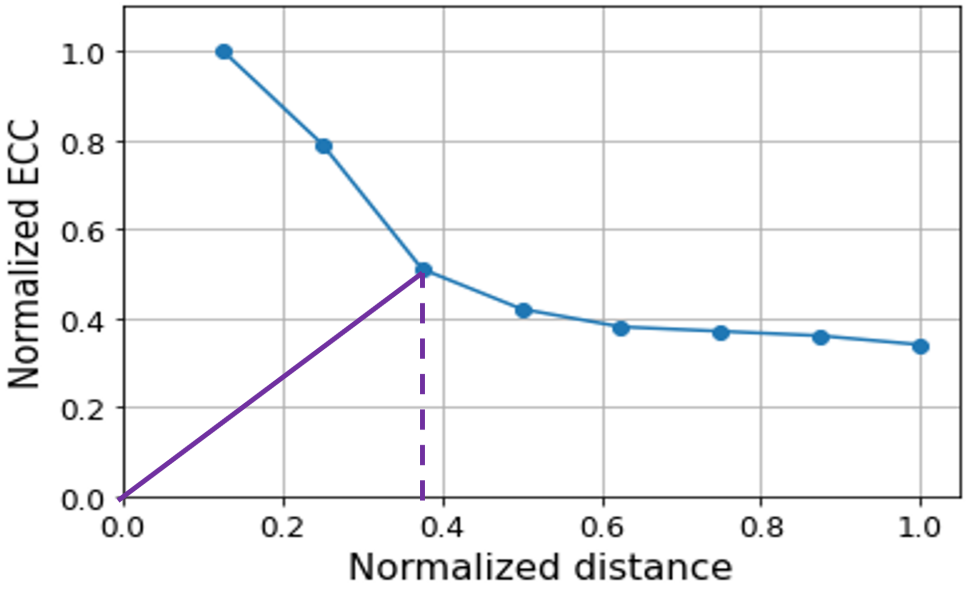

Figure 2.7: Normalized ECC value as a function of normalized antenna spacing. The optimal antenna spacing was obtained using a weighted-sum objective to minimize the ECC and antenna spacing.

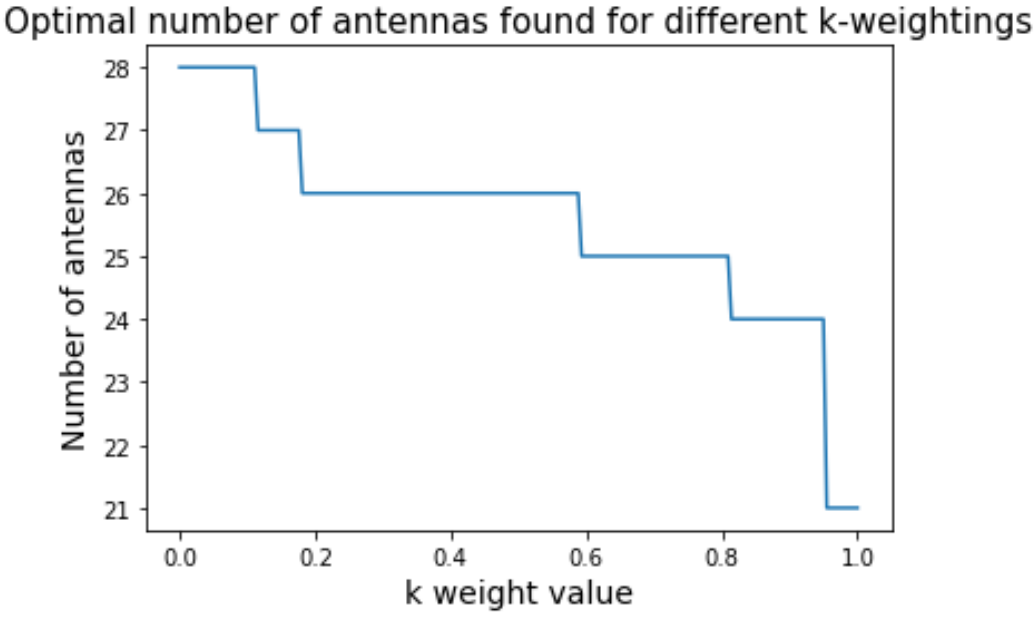

Figure 2.8: Optimal number of antennas determined by simultaneously minimizing the ECC and antenna spacing for different k-weightings described by equation 2.3.

At 1.02 GHz, a maximum ECC value of 0.71 occurred with 1 mm spacing. Each ECC value was normalized to 0.71 and plotted for each antenna spacing normalized to 8 mm (Fig. 2.7). The optimal data point o was found from the normalized ECC, ρ_n, and normalized distance, d_n,

$$o(\rho_n, d_n) = min(\rho_n^2 + d_n^2) \tag{2.2}$$

From this, the optimal spacing was found to be 3 mm, corresponding to twenty-six patch antennas within the 20 cm diameter. However, this method assumes an equal weighting between the normalized ECC and normalized distance. Instead, we can use a weighting factor, k, to weight the effects of the ECC and antenna spacing distance.

$$o(\rho_n, d_n) = min(k\rho_n^2 + (1-k)d_n^2) \tag{2.3}$$

This equation was minimized for k weightings varying from zero to one. The optimal number of antennas as a function of k is shown in Figure 2.8. For small k, the weighing is focused on minimizing the antenna spacing. In this case, the optimal number of antennas is twenty-eight as this is the maximum number of antennas that fit within the device. For large k, the weighting is focused on minimizing the coupling between antennas. In this case, the optimal number of antennas decreases to twenty-one, although the ECC does not vary much between twenty-one and twenty-five antennas. For k = 0.5, we received the same weighting as our previously determined spacing.

By examining the optimal values for varying k, we can visualize twenty-six as the most frequent result. In Figure 2.7, there is a steep decrease in the ECC values that plateaus after the third data point. Data points after this value will not drastically improve the antenna performance, and only further decrease the angular sampling. Therefore, it was determined that twenty-six patch antennas would be incorporated into the device.

Following this, the device was assembled by mounting the antennas on the inside of the smaller

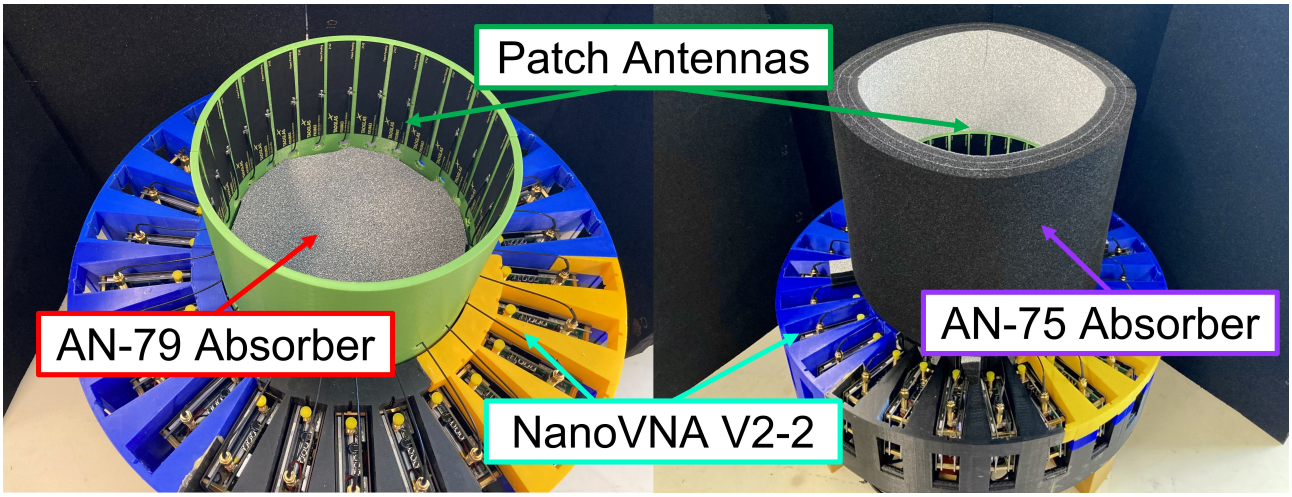

Figure 2.9: Physical setup of the portable detection device consisting of a cylindrical array of patch antennas connected to their own NanoVNA V2. Absorbers were placed at the bottom of the cavity and concentrically with the device during a scan.

3D printed cylinder and inserting the VNAs inside the cavities of the larger cylinder (Fig. 2.9). The two cylinders were fastened together to bring the antennas and VNAs radially close to one another. Mini coaxial cables connected the patch antennas to the first port of their VNAs. Each VNA was connected to a 28-port USB hub underneath the device. A computer was used to switch between USB ports to collect measurements from different antennas.

Initially, the patch antennas featured a U.FL termination and SMA adapter. The antennas mini coaxial cables passed through the first cylinder and connected to the SMA adapter at the VNA port. However, with this set up there was an upward tension on the cable that made the connection between the U.FL termination and SMA adapter unstable. This caused noisy and inaccurate S_{11} measurements. To solve this problem, the manufacturers made custom patch antennas to feature an SMA termination instead of U.FL The inner cylinder was re-printed with larger holes to allow the SMA termination to pass through.

The absorbers' effects were checked by performing multiple S_{11} measurements with and without the absorbers in place. Scans were performed with half of the patch antenna array from antennas #1 - 13. Frequency S_{11} values were recorded for three different orientations of the device. This was done by physically rotating the device 0°, 120° and 240° with respect to its surroundings. At

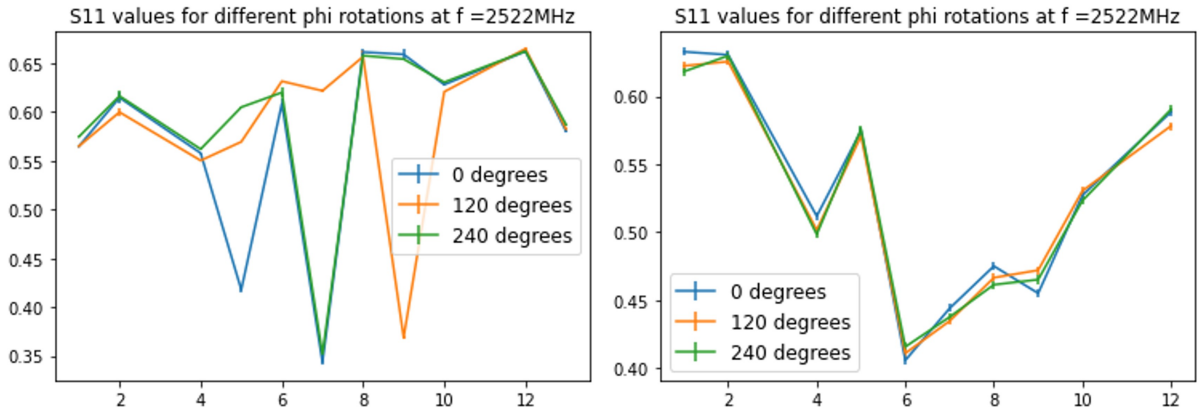

Figure 2.10: Raw S_{11} values from patch antennas #1-13 for 0°, 120° and 240° rotations of the device. Measurements were performed with and without microwave absorbers.

a single frequency, the measurements were repeated three times to determine the mean and estimate the uncertainty from the standard deviation. These measurements were performed with and without the microwave absorbers to display the effect of external environments.

The corresponding S_{11} values for the different orientations at 2522 MHz are displayed in Figure 2.10. It was clear that rotating the device without absorbers affects the measurements. For the measurements with absorbers, the effects from rotation are significantly reduced, and each antenna was able to measure roughly the same value when shifted with respect to their surroundings. Slight deviations with the S_{11} values give an estimation of the system's accuracy capabilities with these particular absorbers. Through the addition of absorbers, the effect of external surroundings is minimized, allowing for rotational symmetry.

Copper rod measurements were performed to monitor the corresponding reflection responses. After converting to the time domain, the open-air measurements were subtracted from the copper rod scans to extract the rod response. This was repeated for eight different rod-to-antenna distances. The peak value of the responses was used to determine the time delay. Each rod response was fit with a Gaussian curve to assess the uncertainty in the time response (Fig. 2.11 and 2.12).

The time location of the S_{11} reflection responses were plotted as a function of rod distance (Fig. 2.13). From this plot, a linear relationship between the antenna-to-rod distance and the corre-

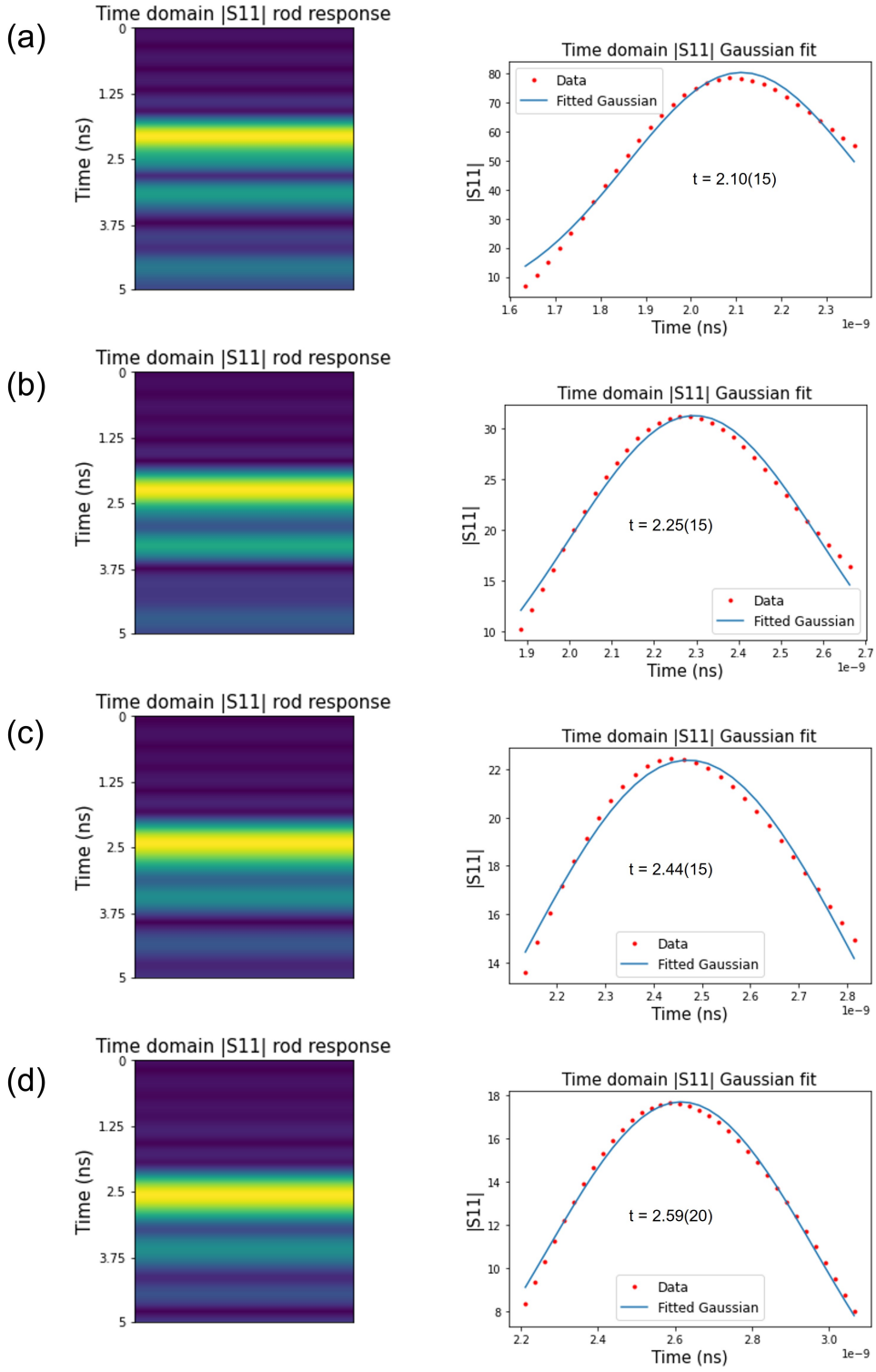

Figure 2.11: S_{11} responses and Gaussian fits for different rod-antenna distances: (a) 2.5 cm, (b) 5.0 cm, (c) 7.5 cm, (d) 10.0 cm.

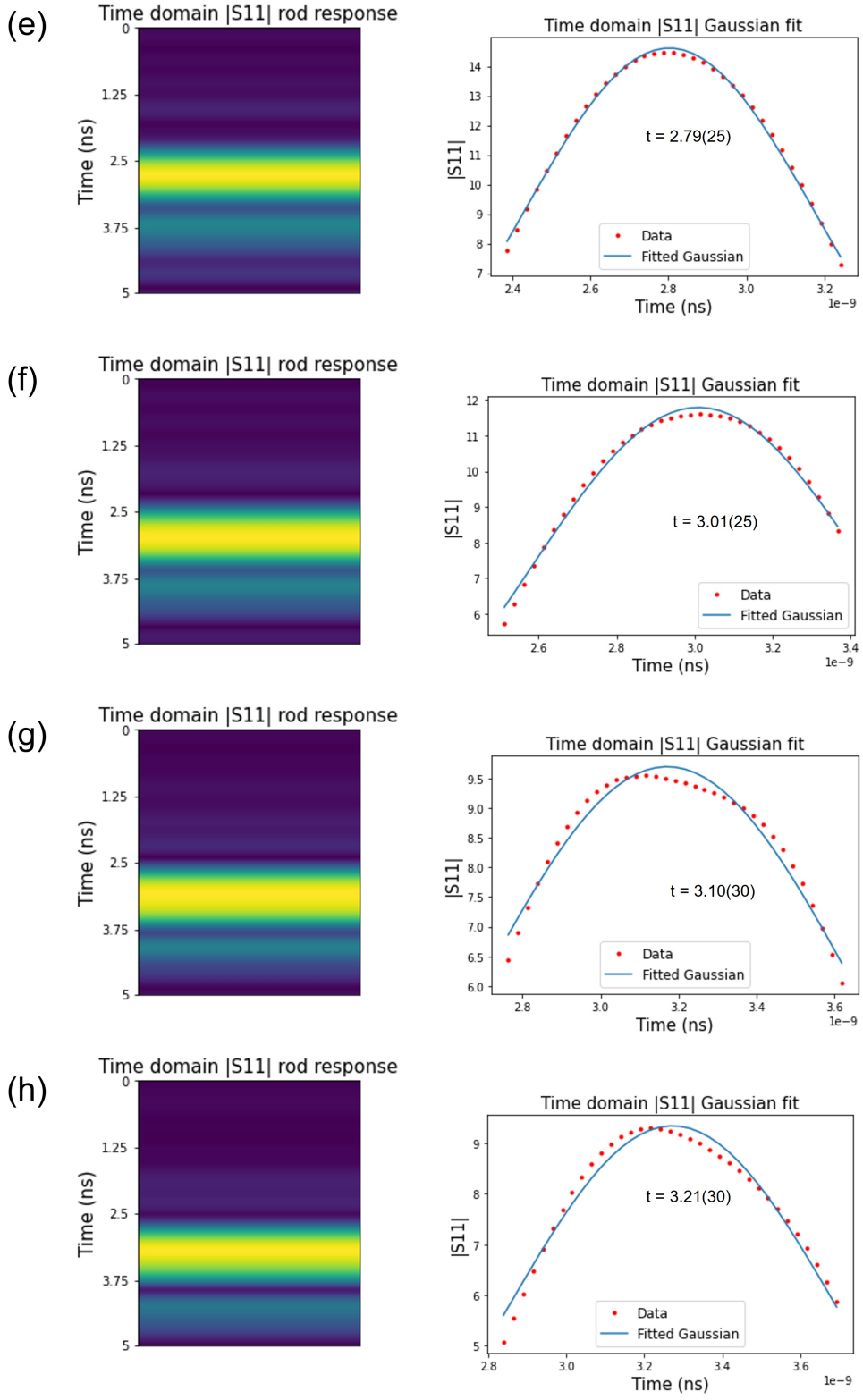

Figure 2.12: S_{11} responses and Gaussian fits for different rod-antenna distances: (e) 12.5 cm, (f) 15.0 cm, (g) 17.5 cm, (h) 19.5 cm.

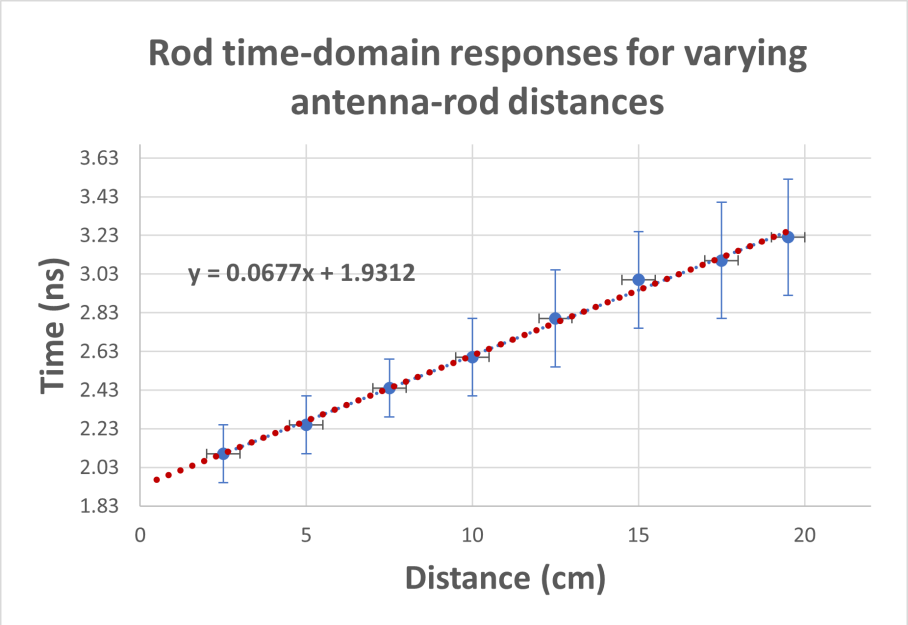

Figure 2.13: Location of the S_{11} time peak as a function of antenna-to-rod distance. The time delay and slope were determined from weighted linear regression.

sponding time delay is observed. Weighted linear regression was used to determine the slope and y-intercept as 0.0677(19) ns/cm and 1.93(3) ns respectively. From the slope, m, the propagation speed v is calculated to be

$$v = \frac{2}{m} = 2.95(8) \times 10^8 m/s \tag{2.4}$$

which agrees with the speed of light in air, 299,792,458 m/s. More accurate measurements for this parameter can be performed using a rod with a smaller radius. From the y-intercept, the time delay between the VNA port and the antenna's plane was determined to be 1.93(3) ns. This value is larger than the open-air Gaussian response of 1.61(26) ns since the open-air response occurs at the antenna-cable interface, and the time delay is determined up to the point of transmission. This allows for full scans to be performed at the plane of the antenna array. Again, this parameter can be re-measured with a smaller rod to decrease the uncertainty in the position. One way to decrease the uncertainties in the time response is to use a larger bandwidth during measurements. Since the NanoVNA technology is improving the bandwidth, testing other patch antennas could be advantageous.

2.4 Conclusion

A portable microwave device was designed and characterized to address issues with breast cancer screening in remote and low-income areas. The overall cost, size, and weight of the device were minimized. The device was assembled with multiple 3D printed materials to mount and fasten the flexible patch antennas and inexpensive NanoVNAs. Microwave absorbers were placed on the bottom and surroundings of the device to minimize external signals and multiple reflections within the chamber.

S-parameter measurements were performed to check the coupling between two adjacent antennas for varying antenna spacings. The ECC coupling parameter was calculated at eight antenna spacings ranging from 1 to 8 mm. The optimal spacing between antennas was found by minimizing the sum of the ECC squared and spacing squared. From here, the optimal number of antennas was determined to be twenty-six. The weightings for the ECC and antenna spacing were varied. However, further investigation may be needed to quantify the effects of coupling versus angular sampling.

Copper rod measurements were performed to determine the corresponding reflection locations in the time-domain. Shifting the distance between the antenna and rod corresponded to a linear shift in the time-domain. The measurements determined the propagation speed to be $2.95(8) \times 10^8$ m/s. The time delay was found to be 1.93(3) ns, allowing for measurements to be performed from the plane of the antenna. From here, full measurements with the device may be performed on different types of rods to determine the systems sensitivity.

The next chapter describes how parameters from the portable device and microwave properties were used to create a radar simulator. The simulated S_{11} values of rod-like objects were compared to measurements of copper rods with the physical device. In Chapter 4, large data sets of numerical rod phantoms and simulated S_{11} data were used to train a convolutional neural network to reconstruct the rod images. This network can supplement training for the physical scans through

transfer learning.

For the next steps, scans may be performed on shell-based breast phantoms to train a machine learning network to detect the presence or absence of a tumour. The development of a portable microwave breast cancer detection device will enable women in remote and low-income areas to access an easily operated, safe, and low-cost breast screening device, allowing early detection of breast abnormalities.

3. Radar-model Simulations and Physical Comparison of S_{11} Measurements

3.1 Introduction

Breast microwave radar spatially focuses reflection signals into the imaging domain to reconstruct high areas of scattering. Typically, radar systems operate in a monostatic or multistatic mode. Monostatic systems transmit and receive with the same antenna to measure the S_{11} reflections. The system can operate using a single antenna [32, 37] or a fixed array of antennas [62, 74]. The antenna(s) illuminates the breast with a broad beam angle to locate backscattering areas. Multistatic systems have multiple antennas in an array [65, 75]. Each antenna, in turn, operates as the transmitting antenna while the remaining antennas receive S_{nm} signals from various scattering angles.

The measured signals are processed with a radar beamformer to identify scatterers within the breast. The DAS beamformer is commonly used to reconstruct reflection responses from monostatic systems [39]. Extensions of this beamformer have been implemented to improve the contrast between fibroglandular and cancerous tissues. Specifically, the delay-multiple-and-sum beamformer improves the contrast through pair-wise multiplication between signals, rewarding high coherence between signals and reduces background clutter [40].

For a monostatic system, the S_{11} reflections can be described using a basic radar model [76]. By using numerical phantoms, the radar model can be used to simulate frequency-domain S_{11} signals. The frequency range and antenna positions within this model can be modified to mirror a physical device. The model assumes each position in the imaging domain acts as a point scatterer,

with plane wave propagation within a homogeneous medium. For complex numerical phantoms, this model neglects many physical aspects of the imaging process.

In this Chapter, S_{11} data was simulated with an improved radar model and results were compared to measurements with the physical device described in Chapter 2. The basic radar model was modified to include multiple scattering, microwave attenuation, and spherical spreading. Frequency domain S_{11} data was transformed to time-domain sinograms using the inverse chirp-z transform (ICZT). Two types of numerical phantoms were used to generate time-domain sinograms: Breast phantoms and rod phantoms.

Simple breast phantoms were created to represent the cross-section of a breast. These 2D arrays consisted of three types of tissues: adipose, fibroglandular, and cancerous. The permittivities of these tissues were calculated using the Debye model [77]. Simulated scans were performed from 1 - 5 GHz to emphasize the effect of attenuation at higher frequencies. These phantoms were used to evaluate the impact of secondary scattering, attenuation, and spherical propagation on the radar model.

Digital rod phantoms were created from two-dimensional images of circular objects representing the cross-section of metal rods. Using the modified radar model, frequency-domain S_{11} signals were simulated from 0.7 - 3 GHz. Physical S_{11} scans of copper rods were performed with the same bandwidth using the device described in Chapter 2. Time-domain sinograms were generated from both the simulated and real S_{11} data. The DAS beamformer was used to reconstruct images of the rods. The simulated and physical sinograms were found to follow a similar pattern, although, for more complex phantoms, further modifications may be needed to improve the accuracy of the radar model.

3.2 Methods

3.2.1 Radar-model Simulation

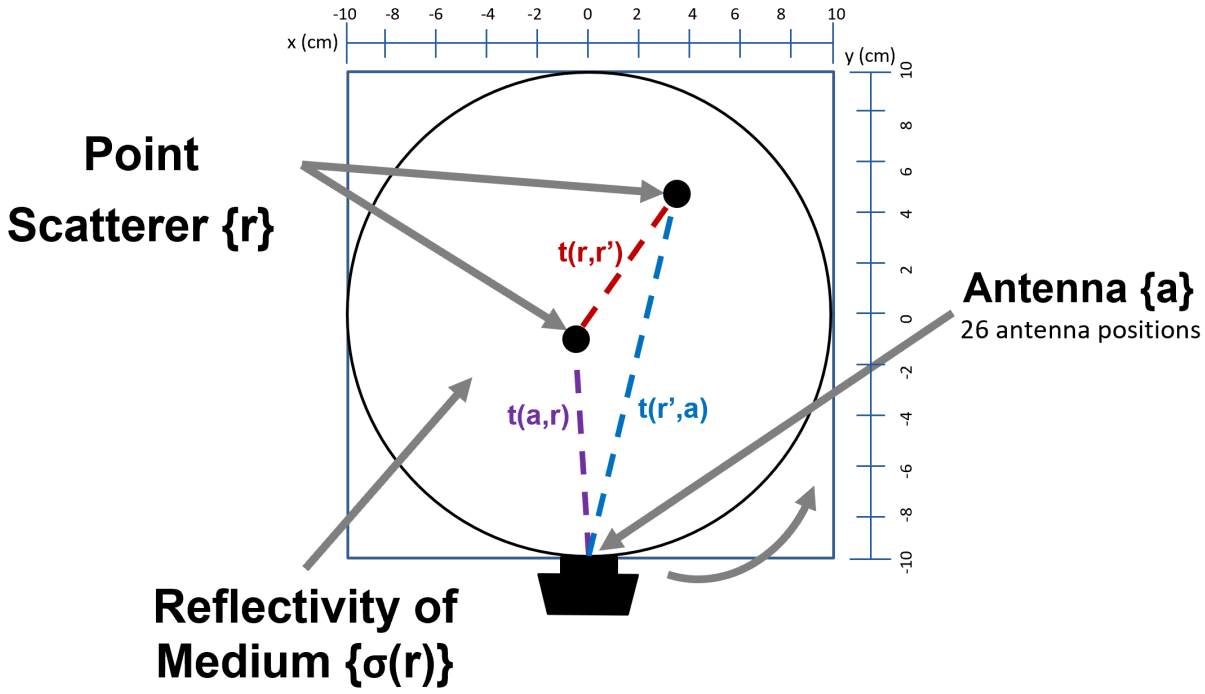

Figure 3.1: Primary scattering shown from antenna position **a** to **r** and back; Secondary scattering from **a** to **r** to a secondary position **r'** and back to antenna **a**.

The measured S_{11} reflections may be simulated using a radar model. In the simplest form, the primary scatter received at emitting antenna position **a** can be described as [76],

$$S_{11}^{1}(f,\mathbf{a}) = \int d\mathbf{r}\sigma(\mathbf{r})e^{-2\pi jf2t(\mathbf{a},\mathbf{r})} \tag{3.1}$$

where σ(r) is the reflectivity at r, f is the frequency of the microwave signal, and t(**a**, **r**) is the propagation time from the antenna position to position r. The propagation speed (v_0) in a material

can be estimated from the speed of light in a vacuum (c) and the relative permittivity (ε_r):

$$v_0 = \frac{c}{\sqrt{\varepsilon_r}} \tag{3.2}$$

To simplify calculations, we assume a homogeneous phantom by calculating the average propagation speed throughout the imaging domain. From here, the propagation time can be estimated by,

$$t(\mathbf{a},\mathbf{r}) = \frac{|\mathbf{r}-\mathbf{a}|}{v_0} \tag{3.3}$$

This basic model assumes far-field, plane wave propagation, a homogeneous phantom, and no multiple scattering or attenuation effects. The model may be modified to incorporate realistic features. Firstly, we can incorporate multiple scattering into the model. The secondary scatter component received at the emitting antenna is,

$$S_{11}^2(f,\mathbf{a}) = \int d\mathbf{r}\sigma(\mathbf{r})e^{-2\pi jft(\mathbf{a},\mathbf{r})} \int d\mathbf{r'}\sigma(\mathbf{r})e^{-2\pi jf(t(\mathbf{r},\mathbf{r'})+t(\mathbf{r'},\mathbf{a}))} \tag{3.4}$$

The complex exponentials describe the propagation of a signal from the antenna position **a** to position **r**, and then from position **r** to position **r'**, and finally from position **r'** back to the antenna position **a**. Calculating the time delays $t(\mathbf{r},\mathbf{r'})$ for all **r** and **r'** is computationally expensive, so we assume that the time delay that occurs between the primary scatter and secondary scatter positions is small compared to the sum of the time delays from each scatter position to the antenna, ie. $t(\mathbf{r},\mathbf{r'}) << t(\mathbf{a},\mathbf{r}) + t(\mathbf{r'},\mathbf{a})$. From this assumption, the time delay from r to r', $t(\mathbf{r},\mathbf{r'})$, may be neglected,

$$S_{11}^2(f,\mathbf{a}) = \int d\mathbf{r}\sigma(\mathbf{r})e^{-2\pi jft(\mathbf{a},\mathbf{r})} \int d\mathbf{r'}\sigma(\mathbf{r})e^{-2\pi jft(\mathbf{r'},\mathbf{a})} \tag{3.5}$$

The two integrals are identical and can be combined to form one term. The simplified secondary

scattering component then becomes,

$$S_{11}^2(f,\mathbf{a}) = \Big(\int d\mathbf{r}\sigma(\mathbf{r}) e^{-2\pi j f t(\mathbf{a},\mathbf{r})} \Big)^2 \tag{3.6}$$

Next, we assume spherical propagation towards the point scatterer and spherical propagation back towards the antenna. For the primary scatter term, we first consider the field F_1 intercepted by a point scatterer from an initial field F_0,

$$F_1 = \Big(\frac{r_0}{|r-a|} \Big) F_0 \tag{3.7}$$

where r_0 is a reference position, taken to be 1 m. The field F_2 intercepted by the antenna after scattering is then,

$$F_2 = \Big(\frac{r_0}{|r-a|} \Big) F_1 \tag{3.8}$$

$$F_2 = \Big(\frac{r_0}{|r-a|} \Big)^2 F_0 \tag{3.9}$$

The constant term in the numerator can be factored out and we are left with the following,

$$S_{11}^1(f,\mathbf{a}) = \int d\mathbf{r}\sigma(\mathbf{r}) \frac{e^{-2\pi j f 2t(\mathbf{a},\mathbf{r})}}{|r-a|^2} \tag{3.10}$$

For the secondary scattering term, we have spherical propagation in one direction, either towards the point scatterer or towards the antenna. Thus, the S_{11} signal can be modelled as,

$$S_{11}^2(f,\mathbf{a}) = \Big(\int d\mathbf{r}\sigma(\mathbf{r}) \frac{e^{-2\pi j f t(\mathbf{r},\mathbf{a})}}{|r-a|} \Big)^2 \tag{3.11}$$

Next, we incorporate microwave attenuation into our model. Exponential attenuation can be described by $e^{-\alpha|\mathbf{r}-\mathbf{a}|}$, where the attenuation coefficient α is given by [78],

$$\alpha = \frac{2\pi}{\lambda_0} \Big[\frac{\varepsilon'}{2} \Big(\sqrt{1 + (\frac{\varepsilon''}{\varepsilon})^2} - 1 \Big) \Big]^{1/2} \tag{3.12}$$

where λ_0 is the free space wavelength, and ε' and ε'' are the real and imaginary components of the relative complex permittivity. We apply the attenuation term to each propagation term within the integrals of the primary and scattered radar models:

$$S_{11}^1(f,\mathbf{a}) = \int d\mathbf{r}\sigma(\mathbf{r})e^{-2\pi jf2t(\mathbf{a},\mathbf{r})-\alpha|\mathbf{r}-\mathbf{a}|} \tag{3.13}$$

$$S_{11}^2(f,\mathbf{a}) = \Big(\int d\mathbf{r}\sigma(\mathbf{r})e^{-2\pi jft(\mathbf{a},\mathbf{r})-\alpha|\mathbf{r}-\mathbf{a}|/2}\Big)^2 \tag{3.14}$$

Altogether, the following expression describes the S_{11} signals received at the antenna position $\mathbf{a}$:

$$S_{11}(f,\mathbf{a}) = \int d\mathbf{r}\sigma(\mathbf{r})\frac{e^{-2\pi jf2t(\mathbf{a},\mathbf{r})-\alpha|\mathbf{r}-\mathbf{a}|}}{|r-a|^2} + \Big(\int d\mathbf{r}\sigma(\mathbf{r})\frac{e^{-2\pi jft(\mathbf{r},\mathbf{a})-\alpha|\mathbf{r}-\mathbf{a}|/2}}{|r-a|}\Big)^2 \tag{3.15}$$

Twenty-six antenna position were equally spaced around the imaging chamber when simulating the physical device. A Cartesian coordinate system was used to record distances and time delays. The first measured antenna angle started at 270° on the Cartesian coordinate system [x = 0 cm, y = -10 cm] and progressed counter-clockwise (Fig 3.1). Frequency domain S_{11} values were simulated using variable bandwidths. The inverse chirp-z transform (ICZT) was used to transform the frequency-domain $S_{11}(f, \mathbf{a})$ values to the time-domain $S_{11}(t, \mathbf{a})$.

3.2.2 Breast Phantom S_{11} Simulation

Breast phantoms were computationally generated to monitor the modifications on the radar model. These phantoms consisted of two-dimensional arrays of 128 $\times$ 128 pixels corresponding to 20 $\times$ 20 cm in the imaging domain. Three types of tissue permittivities were simulated in the phantoms; adipose, fibroglandular, and cancerous. The mean breast diameter of a D-cup breast is 13.7(2) cm [79], and using this diameter, an elliptical object was placed in the center of the array to represent the outline of the breast. Within this object, two more elliptical objects were placed randomly within the breast outline. One of these ellipses corresponded to a section of

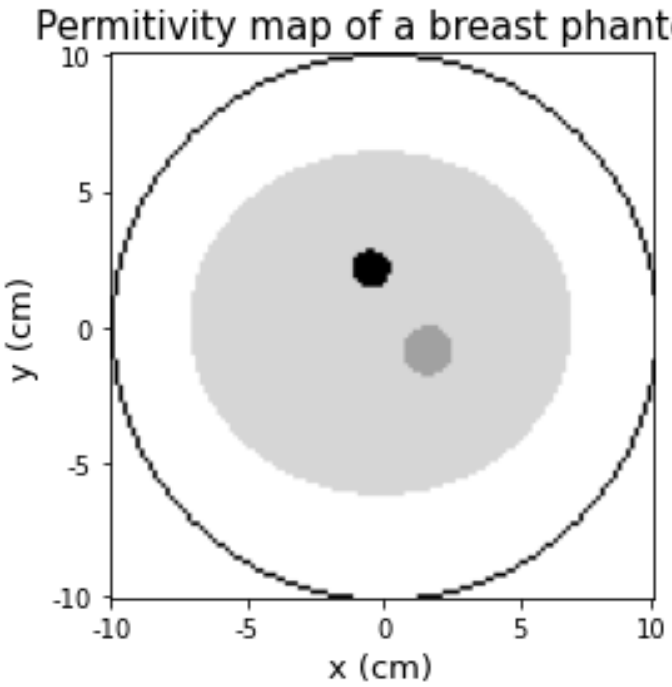

Figure 3.2: Permittivity map of a breast phantom consisting of air, fatty tissue (adipose), fibroglandular tissue, and cancerous tissue.

fibroglandular tissue, and the other represented cancerous tissue. The remaining breast tissue was assumed to be adipose and outside the breast was assigned as air.

The permittivities of the various breast tissues may be estimated using the Debye model:

$$\varepsilon_r = \varepsilon_\infty + \frac{\varepsilon_s - \varepsilon_\infty}{1 + j\omega\tau} - j\frac{\sigma}{\omega\varepsilon_0} \tag{3.16}$$

The Debye model parameters of different breast tissues [77] are outlined in Table 3.1. For these simulations, we used a bandwidth of 1 - 5 GHz, sampling every 20 MHz. The wider bandwidth allows the more significant attenuation at these higher frequencies to be incorporated. The tissue permittivities can be estimated using the Debye model parameters in Table 3.1 and the center frequency of 3 GHz:

$$\varepsilon_r = 9.95 - 1.29\,j \text{ (Adipose)}$$

Material	ε_∞	ε_s	τ(ps)	σ
Adipose	7.0	10	7.0	0.15
Fibroglandular	6.14	21.57	7.0	0.31
Cancerous	3.99	54.00	7.0	0.70

Table 3.1: Debye model parameters for various breast tissues [77].

$$\varepsilon_r = 21.31 - 3.86j \text{ (Fibroglandular)}$$

$$\varepsilon_r = 53.14 - 10.68j \text{ (Cancerous)}$$

An example of a permittivity breast model is shown in Figure 3.2. From here, a reflectivity map can be determined by calculating maximum permittivity shifts in neighbouring pixels. For a single interface, the reflectivity (Γ) is determined between the two neighbouring permittivities ε_r^1 and ε_r^2,

$$\Gamma = \left| \frac{\sqrt{\varepsilon_r^2}/\sqrt{\varepsilon_r^1} - 1}{\sqrt{\varepsilon_r^2}/\sqrt{\varepsilon_r^1} + 1} \right| \tag{3.17}$$

The corresponding reflectivity map of the breast model from Figure 3.2 is shown in Figure 3.3. Using the radar model, frequency-domain S_{11} data was developed from this reflectivity map, and converted to the time domain using the ICZT. The time-domain S_{11} data was used to create an image map of the reflections known as a sinogram, where the y-axis refers to the time delay and the x-axis refers to the antenna angular position.

Five different sinograms were created for the same breast phantom to monitor the effect of the modifications added to the radar model. The first uses the basic radar model described by in Equation 3.1. The second uses the basic radar with the addition of the secondary scatter outlined in Equation 3.6, while the third simulation utilizes the spherical spreading on the primary scatter shown in Equation 3.10. The fourth incorporates the exponential attenuation in the primary scatter as described by Equation 3.13, while the final simulation combines all the modifications represented by Equation 3.15. These different sinograms aim to illustrate each change's improvement to the simple radar model.

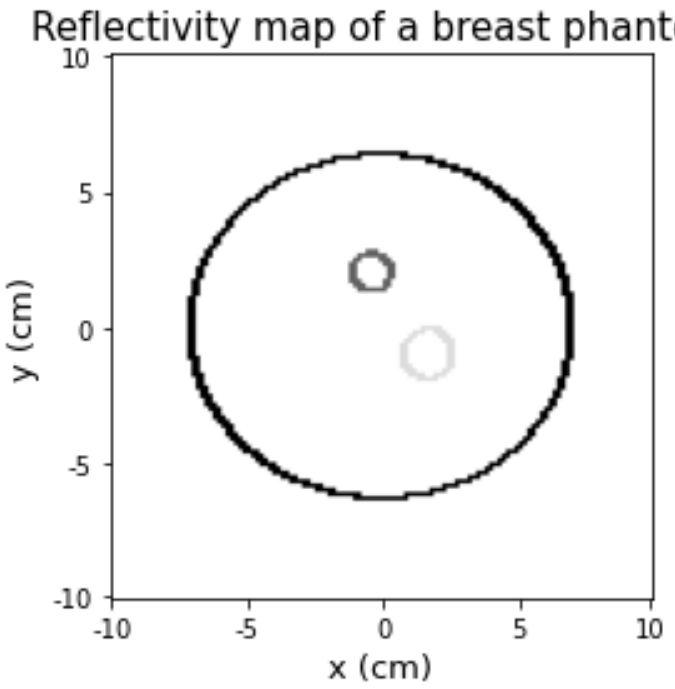

Figure 3.3: Reflectivity map of the breast model created from the permittivities of neighbouring pixels.

3.2.3 Rod S_{11} Simulation

Time-domain reflection data can be simulated with the radar model and measured with the physical device. First, using the radar-model, simulated results were generated for simple rod phantoms. These phantoms consist of a 128 $\times$ 128 pixel array, representing a 20 $\times$ 20 cm imaging chamber, resulting in a resolution of 1.56 mm/pixel. The imaging domain consists of the circular region within the array, centered with a radius of 10 cm. Within this domain we may represent rods by creating 3 mm circular objects. If we assume a copper rod with 100% reflectivity, then a reflectivity map may be generated at the interfaces between the rod and air. These interfaces will have values of 1, whereas everywhere else has a reflectivity of 0.

From this reflectivity map, the radar model may be used to simulate S_{11} data from 0.7 - 3 GHz using 115 frequency points. Since most of these phantoms consist of air, the effects of attenuation are negligible. Therefore, the secondary scatter with the spherical propagation model is sufficient.

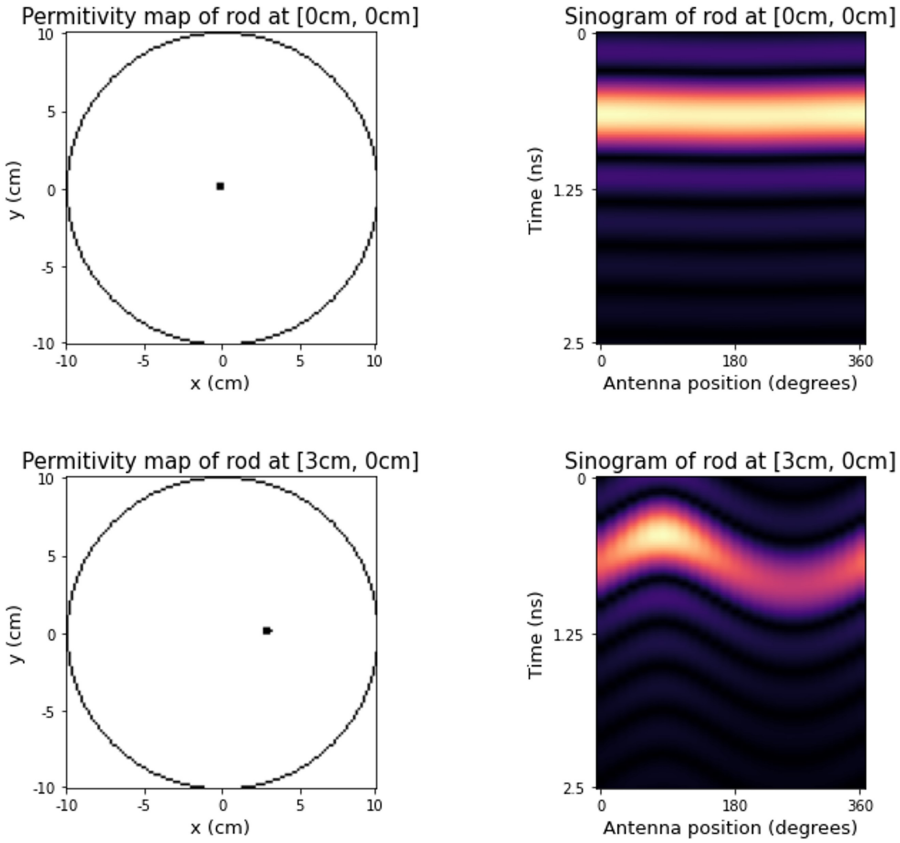

Figure 3.4: Rod permittivity model and time-domain sinograms for two rod models centered at [0cm, 0cm] and shifted to [3cm, 0cm].

An example of the sinograms for two different rod models, first with the rod centered in the device and secondly with the rod shifted 3 cm to the right, are illustrated in Fig. 3.4.

For the first sinogram example, a constant reflection response at 0.67 ns for each antenna is obtained (Fig. 3.4). This is expected as each antenna is 10 cm away from the rod, so the signal would travel 20 cm total. If the rod is shifted 3 cm to the right, the reflection responses follow a sinusoidal pattern as the relative distance between the rod and antenna varies (Fig. 3.4).

From these simulated sinograms, a simple DAS reconstruction can be performed. The rod offsets and angles were varied to visualize the corresponding shifts in the time domain. Reconstructions were performed for the follow rod positions [x(cm), y(cm)]: [0,0], [0,3], and [3,0]. These were compared to results from the physical device where similar scans were performed with copper rods.

3.2.4 Rod S_{11} Physical Measurement

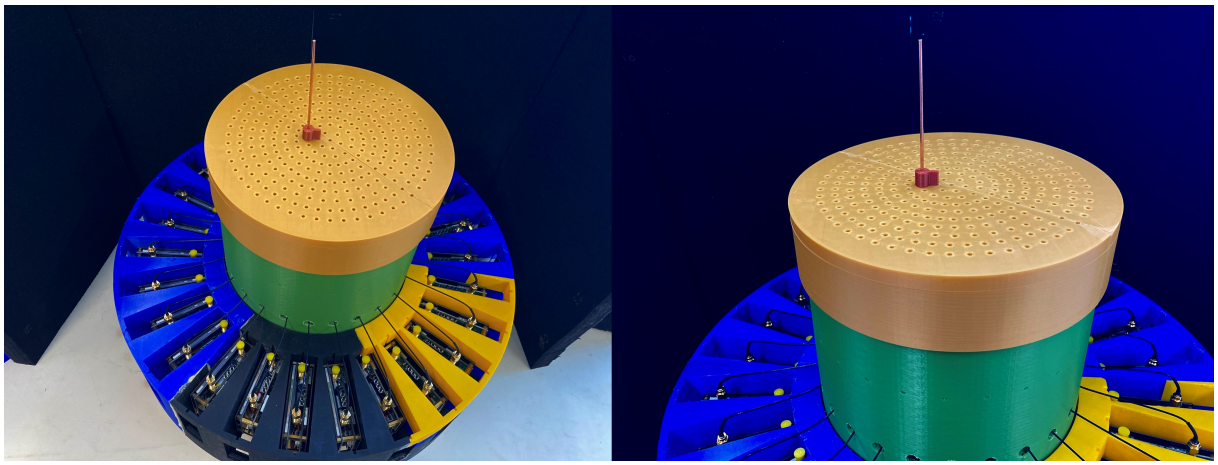

Figure 3.5: Cylindrical lid for positioning, securing, and straightening rods for physical measurements.

The physical device developed in Chapter 2 was enabled to perform full scans. Each antenna was connected directly to port 1 on their NanoVNA. A USB hub was used to communicate with each VNA individually. A SOL calibration was performed on every VNA and the antenna cable time delay was implemented to initialize S_{11} measurements from the plane of the antenna array. To enable accurate rod positioning, a rod holder was 3D printed (Fig. 3.5). This consisted of a cylindrical lid, tightly fastened onto the device. Cylindrical cavities were located through the top of the lid in a polar coordinate system, repeating every 1 cm along the radial direction. The radius of the cavities were sized to be 3.1 mm so that 3 mm rods could easily fit through. Tighter plugs were created to fasten around the 3 mm rod while securing an upright position with respect to a neighbouring hole 1 cm away. Ridges on the inside of the lid allow for the placement of AN-75 absorbers. The addition of the rod holder ensures accurate positioning of the rods while maintaining security in an upright position.

After the initial setup, full scans were performed by sequentially selecting each VNA to act as the transmitter and receiver. Physical rod scans were performed to mimic the S_{11} simulations from the numerical rod phantoms. Measurements were taken with each antenna from 0.7 - 3 GHz

using 115 frequency points. Initially, an open-air scan was performed with the device shielded with AN-75 radar absorber material placed concentrically around the device. A copper rod was inserted through the lid and into the imaging chamber for the following rod coordinates: [0,0], [0,-4] [x(cm), y(cm)]. From the ICZT, time-domain sinograms were created for each rod position. Using the DAS beamformer, reflection images were reconstructed and compared to the results from the radar simulations.

3.3 Results and Discussion

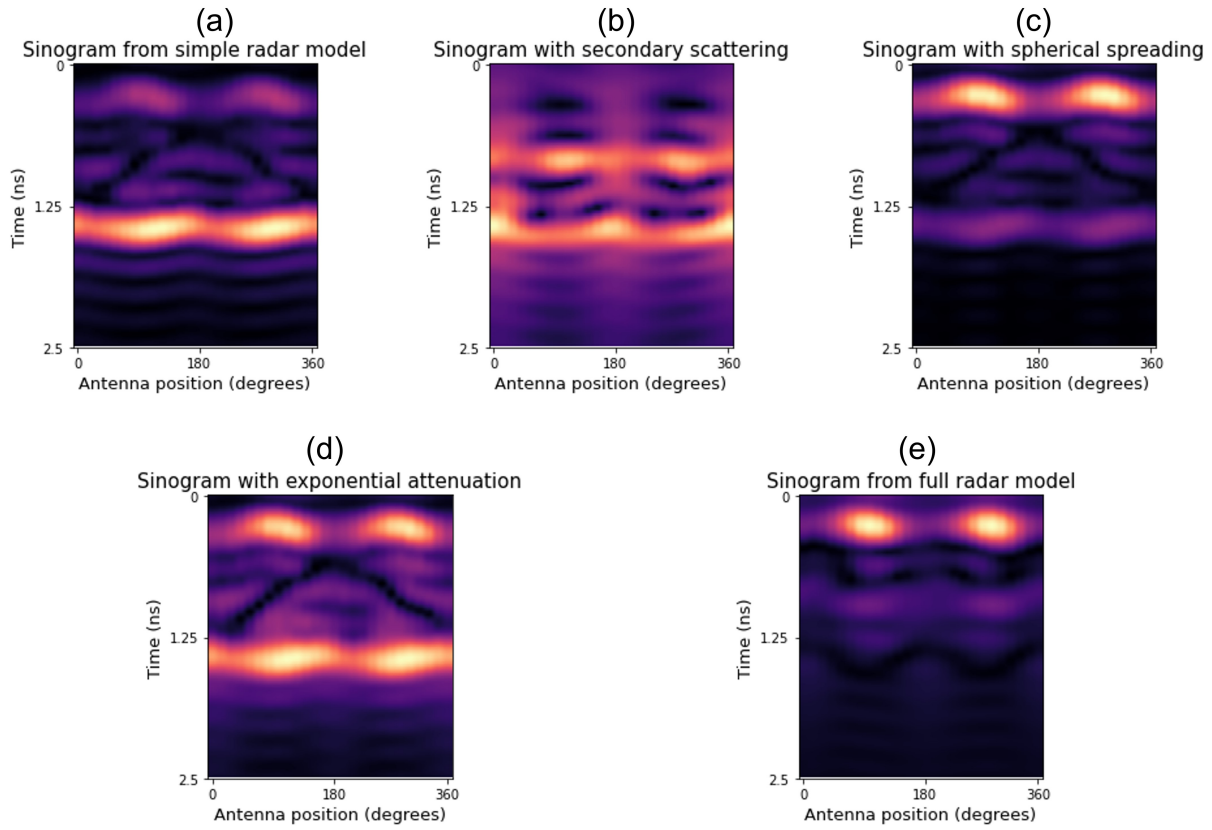

Figure 3.6: Radar model sinograms of a breast phantom using (a) the simple radar model, (b) secondary scattering, (c) spherical spreading, (d) exponential attenuation, and (e) the full radar model.

This section describes the results of modifying a basic radar model to incorporate different physical components when simulated with a 2D numerical breast phantom. The results from the modifications to include secondary scattering (b), spherical wave propagation (c), and exponential microwave attenuation (d), are displayed in Figure 3.6.

For the simplistic radar model, the highest intensity reflections are due to the air-to-breast and breast-to-air interfaces. The responses from the tumour and fibroglandular tissue are located between these times. Since the reflectivity is the highest at the air-to-breast interface, this response is higher than the remaining interfaces. However, this response would be lessened if the breast were in a matching medium. The secondary scattering component features multiple reflections along and within the breast. Most of the secondary scattering is between the different components along the air-to-breast interface.

The accuracy of the secondary scattering component is limited by the assumptions made in the derivation. This assumed that the time travelled between point scatterers is negligible compared to the total travelled time. However, this is not always true, especially for scatterers further from the centre of the chambers. The model could be adjusted to represent the scattered times more accurately, but this increases computational time by N^{th} power. Therefore, a further modification can be made by only incorporating secondary scattering that satisfies this assumption. The spherical spreading and exponential attenuation models both decrease the intensity for longer time delays, emphasizing reflectors closer to the plane of the antenna. The overall (full) model focuses on the first air-to-breast interface, with the deeper reflection points overpowered by those from shallow depths.

The radar model was performed on multiple numerical rod phantoms. As these phantoms consist 99% in air, the effects of attenuation are negligible. First, the 3 mm circular object was shifted along the y-axis of the chamber for the following amplitudes: 5 cm, 3 cm, 0 cm, -3 cm, and -5 cm (Fig. 3.7). The corresponding sinograms resulted in a sinusoidal response from the circular array of antenna positions. The amplitude of the response varied as the rod shifted along the y-axis.

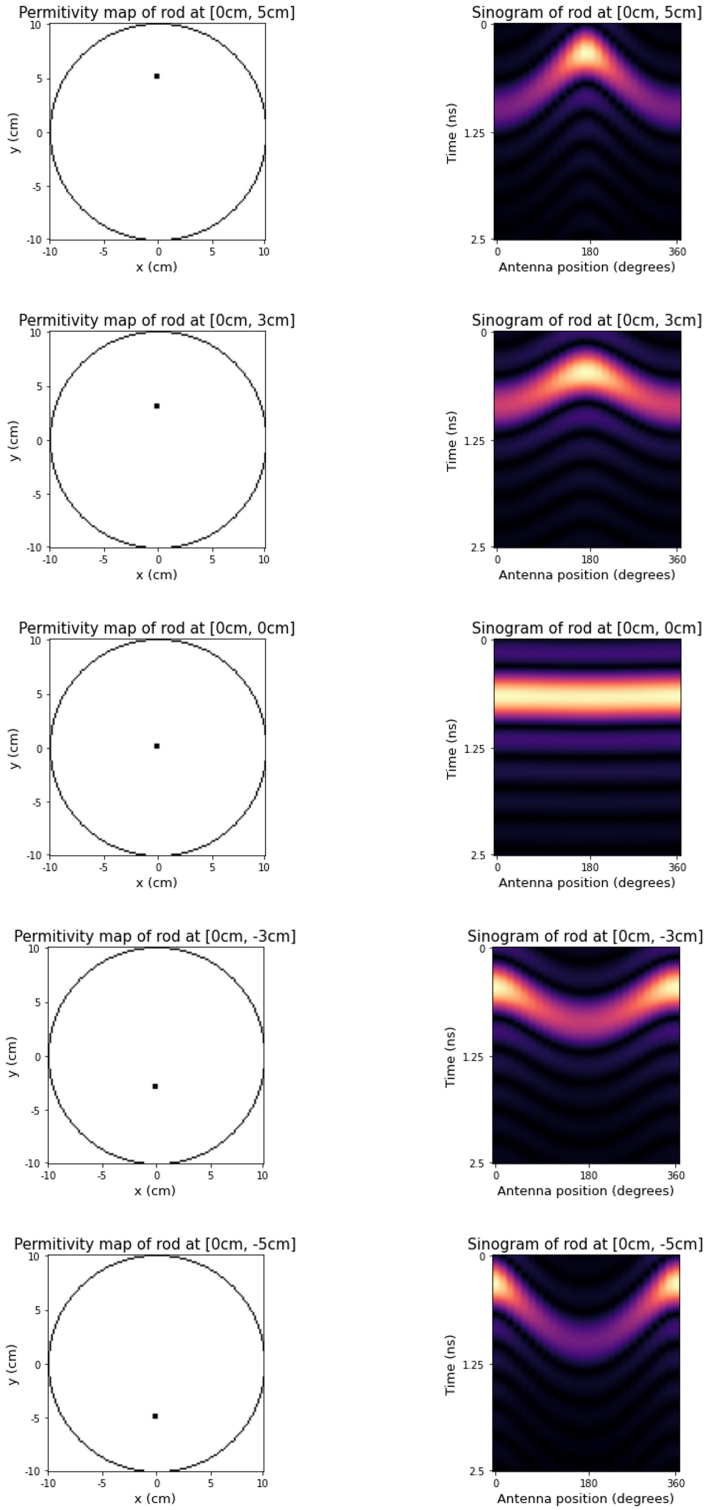

Figure 3.7: Radar model sinograms for shifts in rod offset for the following amplitudes: 5cm, 3cm, 0cm, -3cm and -5cm.

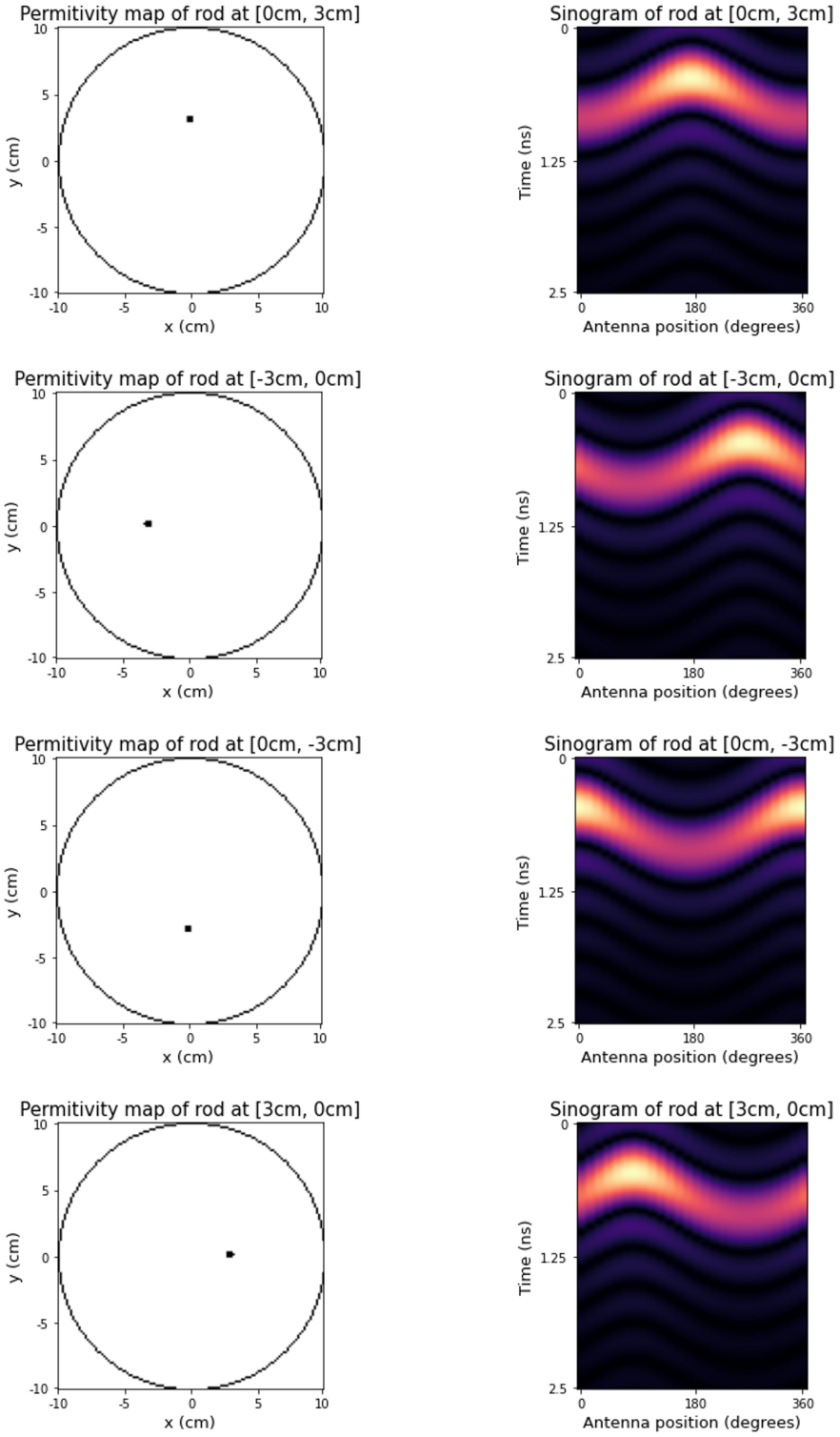

Figure 3.8: Radar model sinograms for shifts in rod phase at a constant amplitude of 3cm. The polar angles with respect to the first antenna position: 180°, 270°, 0°, 90°.

Following this, the rod was fixed at an amplitude of 3 cm while the polar direction was changed to the following angles: 180°, 270°, 0°, and 90° (Fig. 3.8). For these variations, the amplitude of the sinusoidal response remained the same while the phase shifted according to the polar angle with respect to the initial antenna position.

The simple DAS beamformer was used to reconstruct images from the simulated time-domain sinograms. Reconstructions were performed for the following rod locations: [0cm, 0cm], [3cm, 0cm], and [0cm, 3cm] (Fig. 3.9). The reconstructed images feature a large response with the center located at the position of the rods. The reconstructed responses are large because the time-domain sinogram responses are wide for this particular bandwidth. This suggests that reconstructions for more complex phantoms will produce images that are difficult to interpret. Therefore, radar imaging with a DAS beamformer may not be suitable for a smaller bandwidth from 0.7 - 3 GHz. However other reconstruction methods, such as machine learning, can be utilized to reconstruct with a finer resolution.

Physical scans were performed with the microwave device for rod positions [0cm, 0cm] and [0cm, -4cm]. The corresponding sinograms and a DAS reconstruction are displayed in Figure 3.10. With the rod centered in the middle of the device, high reflection responses are located at approximately the same time delay. However, there are some inconsistencies in the mean and standard deviation of the responses. This may suggest setup errors and/or slight variability with the antennas. When the rod is shifted towards the first antenna position by 4 cm, there are notable shifts in the time responses. As expected, the response follows a similar sinusoidal pattern as the simulations. The intensity falls off as the relative distance between the rod and antenna increases. However, as that distance increases there are more inconsistencies between this sinogram to the simulated ones. Specifically, around 180 degrees, the responses are not as focused and clear. The effects of multiple scattering between the rod and inner cylinder could introduce signals that would not be removed through an open-air reference scan.

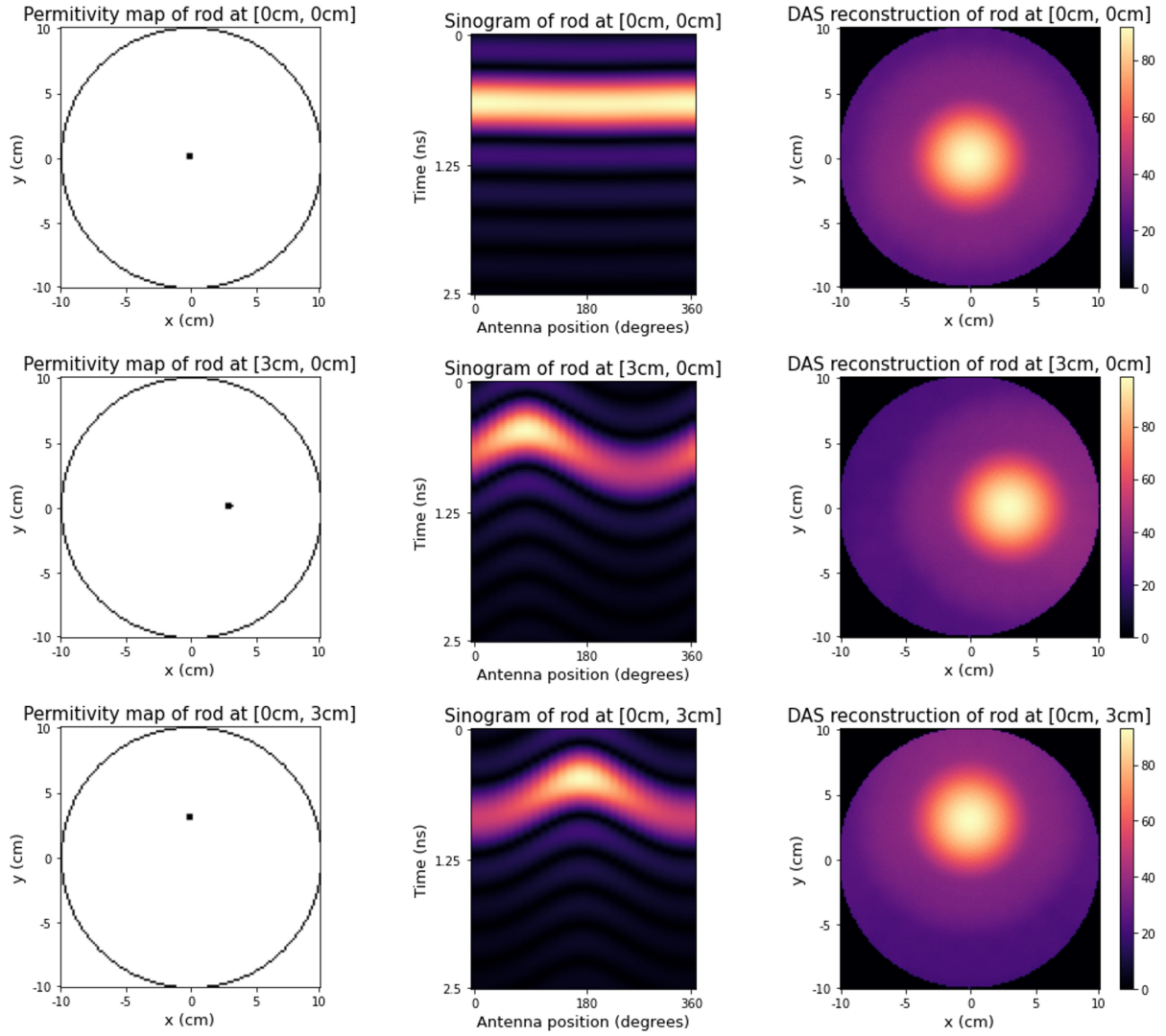

Figure 3.9: DAS reconstruction of radar model simulations for rod positions [0cm, 0cm], [3cm, 0cm], and [0cm, 3cm].

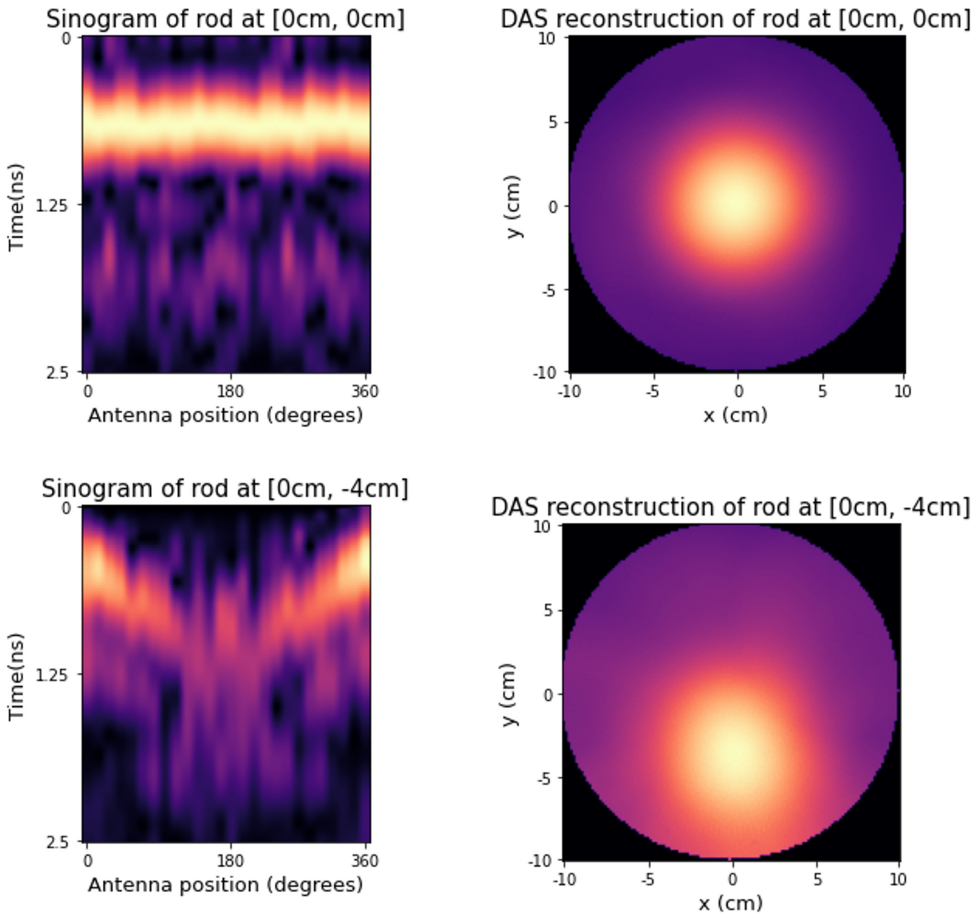

Figure 3.10: Physical device sinogram scans and DAS reconstruction for the following rod positions within the imaging chamber: [0cm, 0cm] and [0cm, -4cm].

The DAS reconstructions of the physical scans display high reflection responses centered close to the location of the copper rods. The responses are not as well confined as are the simulated sinograms, notably as the rod deviates from the center of the device. Rod positioning errors, calibration methods, antenna variations, scattering between the rod and device, and near-field effects may all contribute to the discrepancies between the physical and simulated measurements. Modifications to the physical device can improve the overall accuracy of the measurements. Specifically, individual antenna calibrations may be needed to ensure uniformity. Additionally, further improvements to the radar model can be performed to account for the antenna beam pattern, VNA properties, and microwave propagation.

3.4 Conclusion

A simplistic radar model was modified to account for secondary scatter, exponential attenuation, and spherical spreading. The radar model was used to simulate the parameters of the physical device described in Chapter 2. A simplistic numerical breast phantom was created to model the dielectric properties of fibroglandular, adipose, and cancerous tissue. This phantom was used to assess the effects of the various modifications to the simplistic radar model. Both spherical spreading and exponential attenuation reduced the signal intensity at distances further from the antenna plane. Secondary scattering created various reflection points within the time window of the breast, mostly due to the air-to-breast interface.

$S_{11}(f, \mathbf{a})$ reflections from numerical rod phantoms were simulated with the radar model and were transformed into time-domain $S_{11}(t, \mathbf{a})$ reflections. These measurements were compared to physical scans of copper rods. For the radar model simulations, shifts in the rod's radial and azimuthal position within the chamber corresponded to shifts in the amplitude and phase of the sinograms sinusoidal responses. Similar shifts were noted for the physical scans, as expected. In both scenarios, the DAS reconstruction was able to centre a high reflection response at the location of the rod. However, the responses were less defined for the physical scans due to additional effects and inconsistencies with the measurements.

Alterations to the radar model can account for frequency dependence, antenna gain, beam pattern, and heterogeneity. Creating 3D frequency dependant permittivity maps allows for realistic exponential attenuation calculations as a function of frequency. A frequency-dependant antenna gain, and beam pattern term can be added to the S_{11} integral. The time responses are estimated by assuming a homogeneous phantom and uniform propagation speed. However, the accuracy of these times may be improved by allowing heterogeneity in these calculations through ray line tracing. Improving the accuracy of the radar model would allow for an investigation into the optimal system bandwidth.

This radar model is also important for generating large data sets that may be used for machine learning. Chapter 4 investigates using a convolutional neural network to detect and locate rods from S_{11} time-domain data. For this type of training problem, a large data set is needed to transform S_{11} data to the imaging domain. The number of physical scans required for this type of problem would be time-consuming. Therefore, the radar model may supplement the physical scans to increase the training set size. Specifically, large data sets of sinogram-image pairs may be generated to train and test the machine learning network. Transfer learning may then be used to detect and locate rods within the physical device.

4. Machine Learning Detection from Rod S_{11} Simulations

4.1 Introduction

Artificial intelligence (AI) offers many possibilities for the medical imaging field. The use of machine learning has shown encouraging results for imaging modalities such as X-Ray, MRI, and positron emission tomography (PET) [43,44,80]. Deep learning can improve the quality of images by reducing unwanted artifacts, improving contrast, and minimizing noise, and can also be used to replace image reconstruction methods [42]. It has been demonstrated that a convolutional neural network can directly reconstruct PET images from sinogram data to improve image quality [81,82]. Within MRI research, deep learning as a reconstruction method has been shown to increase image sharpness and signal-to-noise ratio [83–85]. Aside from image processing, AI may also be used to interpret the measured data to detect diseases or abnormalities within the patient.

Current research has focused on automated tumour detection that determines the presence or absence of a tumour through AI-based machine learning [45,47]. This process does not reconstruct images but instead trains a machine learning network to detect, classify, and/or locate an abnormality. In resource-limited areas, this has advantages over AI-based image reconstruction because there is no need for a professional to interpret the images to obtain a diagnosis.

A small and low-cost microwave detection device was developed in Chapter 2. The VNAs and antennas were calibrated and tested to measure the S_{11} reflections of a copper rod. Chapter 3 used a radar model to simulate S_{11} signals of numerical phantoms. In particular, the model was applied to rod phantoms to simulate their corresponding time-domain sinograms, and results were compared

to sinogram measurements from the physical device.

This Chapter aims describes the training of a machine learning network to locate rod responses from the simulated sinograms. Numerical phantoms were generated with two circular objects representing the cross-section of a rod. The rod materials were varied to incorporate the various combinations of the following reflectivities: 10%, 30%, 50%, 70%, 90%, and 100%. The copper rod was represented as a "positive response" by the 100% reflectivity rod. The remaining reflectivities were assigned to the second rod so that the contrast between the two responses was varied. Half of the rod models consisted of a copper "positive" response, while the other half featured both rods the secondary reflectivity.

The radar model was used to generate time-domain sinograms from these rod models. Convolutional neural networks were designed and optimized to locate the copper rods using a) direct image reconstruction and b) parameter detection. With the first method, the convolutional neural network was trained to reconstruct a 128×128 array representing the reflectivity map of the rod model. In the second method, the convolutional neural network produced an 8×1 array of the rod's x position, y position, reflectivity, and radius. The MSE, accuracy, sensitivity, and specificity were monitored to determine the performance as the contrast of the rods was varied.

Actual scans from the physical device can be used to train the same convolutional neural network to locate rod responses. Through transfer learning, patterns learned from the simulated S_{11} data supplement the training process using the experimental scans. Similar training can be performed on complex breast phantoms that accurately represent the morphology and dielectric properties of the breast. Through AI, a portable microwave device can be trained to detect a breast abnormality, allowing for safe, low-cost, and accessible screening for women in remote and low-income areas.

4.2 Methods

A convolutional neural network (CNN) was designed to analyze radar time-domain sinograms. A machine learning network was trained to detect and locate rod responses using image reconstruction and rod-parameter detection. Both methods are described and tested in this Chapter.

4.2.1 Machine Learning Image Reconstruction

This section describes how the network was trained to reconstruct the corresponding numerical rod phantoms from their simulated sinograms. The rod images consisted of two rods with varying reflectivities. A copper "positive" response was represented by 100% reflectivity. The network reconstruction predictions were compared to the ground truth rod images.

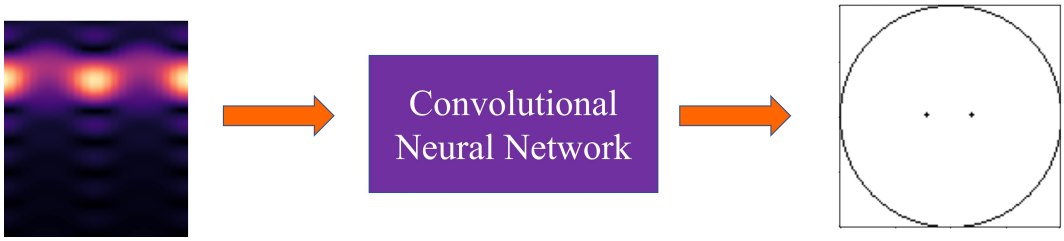

Figure 4.1: CNN image reconstruction from time-domain sinograms.

Training and Testing Set Development

Training and testing sets were generated using rod models and their simulated S_{11} sinograms. Similar to Chapter 3, the rod models consisted of 128 $\times$ 128 pixels representing a 20 $\times$ 20 cm array. The imaging chamber was defined by the outline of the 20 cm circular antenna array. Two 3 mm diameter circular objects were placed within this chamber to represent the rod cross-sections. The circular objects were assigned one of two reflectivity values: 100% representing a copper rod or a variable m% representing a second material with lower reflectivity.

The data set had equally distributed reflectivity combinations; 100% & m%, or m% & m%.

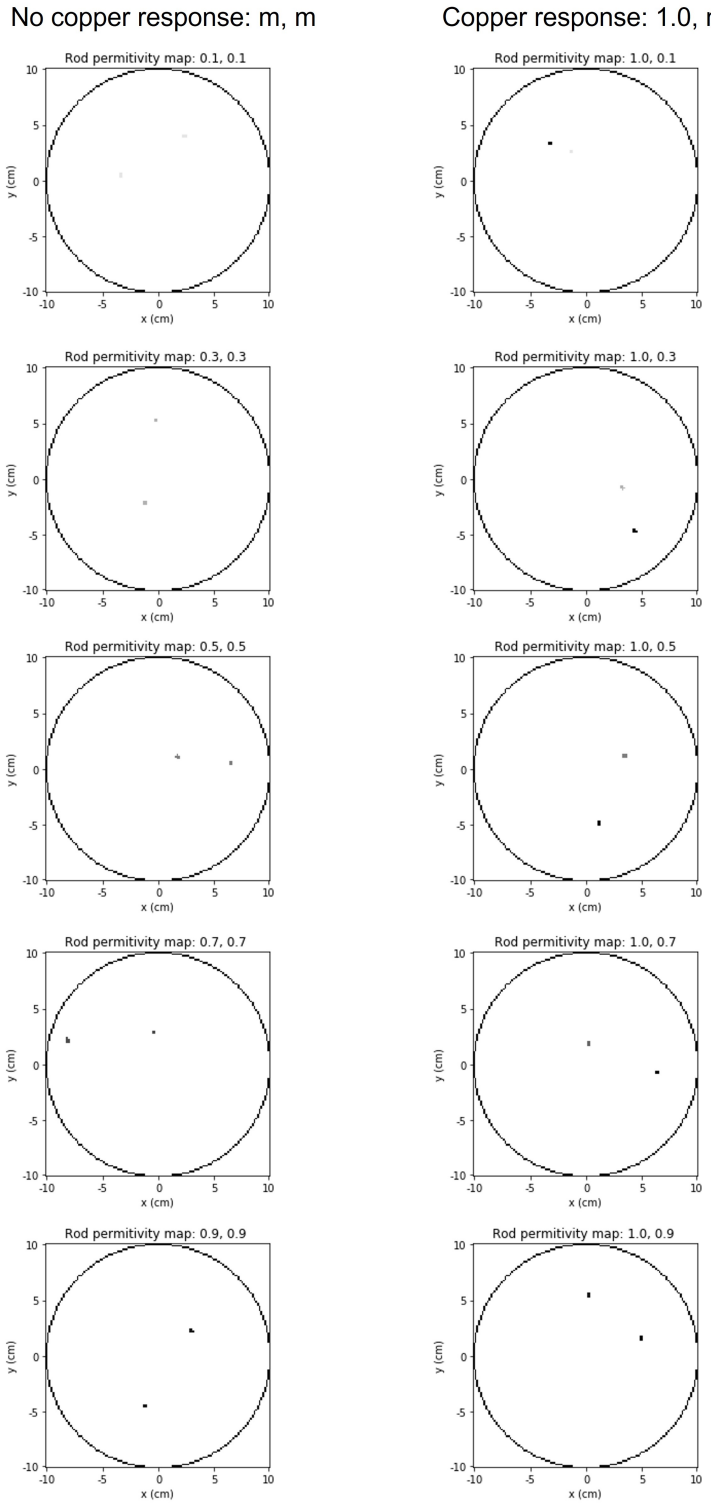

Figure 4.2: Rod model data set consisting of two rods with varying reflectivities. Half of the rod models included a copper rod with 100% reflectivity.

Reflectivity % Combination	Unique dual Rod Models	Augmentations Per Model	Total
10% & 100%	1000	25	25,000
30% & 100%	1000	25	25,000
50% & 100%	1000	25	25,000
70% & 100%	1000	25	25,000
90% & 100%	1000	25	25,000
10% & 10%	1000	25	25,000
30% & 30%	1000	25	25,000
50% & 50%	1000	25	25,000
70% & 70%	1000	25	25,000
90% & 90%	1000	25	25,000
All	10,000	25	250,000

Table 4.1: Total number of unique rod models and augmentations for various reflectivity combinations.

Therefore, half of the data set included the presence of a copper rod, whereas the other half lacked a copper rod. The m% reflectivity was equally varied between five values: 10%, 30%, 50%, 70% and 90% (Table 4.1). The second material was varied to monitor the performance of the machine learning network for different contrasts.

Overall, 10,000 unique rod models were created by randomizing the position of the rods (Fig. 4.2). The distance between adjacent rods was always larger than 1 cm. S_{11} data were simulated for each unique rod model using the radar simulation developed in Chapter 3. The ICZT was used to transform this into time-domain sinograms with 101 time points.

The data set was increased post-simulation by randomized rotation and flipping. Rotation on the image in discrete $360/26^{\circ}$ angles corresponded to shifting the columns to a new starting angle within the sinogram (Fig. 4.3d). Flipping the image about the y-axis corresponded to a horizontal flip in the sinogram (Fig. 4.3b). This was equivalent to scanning clockwise instead of counter-clockwise. Flipping the image about the x-axis required the starting sinogram angle to jump 180° and scan clockwise (Fig. 4.3c).

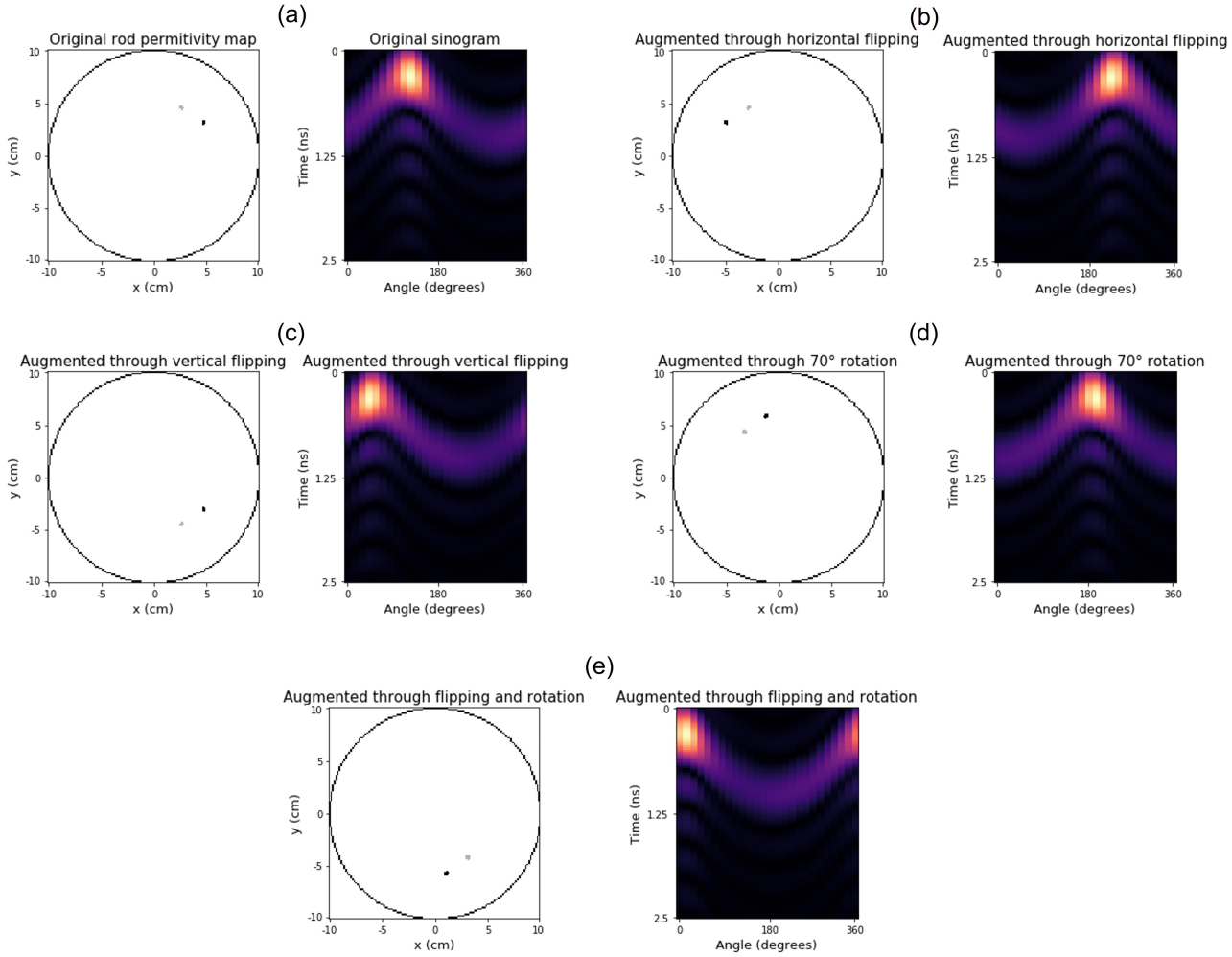

Figure 4.3: Rod position and sinogram augmentation of the (a) original through (b) horizontal flipping, (c) vertical flipping, (d) 70° rotation, and (e) all of the above.

Each unique sinogram-image pair was randomly augmented twenty-five times, increasing the data set to 250,000 sinogram-image pairs. The pairs were split 80-20 for the training and testing set, respectively.

Network Design and Training

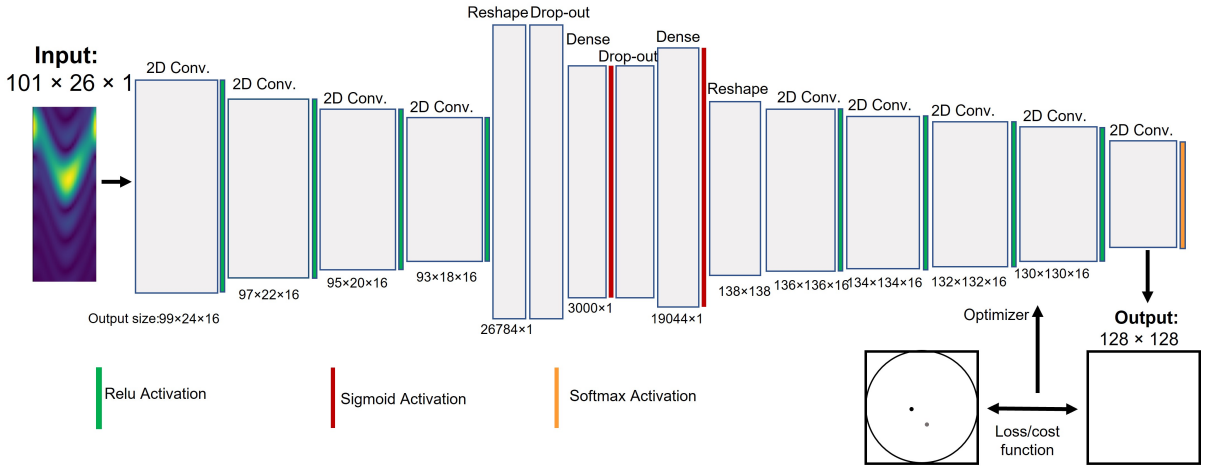

Figure 4.4: CNN architecture consisting of convolutional, reshaping/flattening, dense, drop-out, and activation layers.

The machine learning design and training was performed using Keras, an open-source software library within Python. A CNN was built to transform time-domain S_{11} sinograms to their corresponding rod reflectivity models. The network architecture was created using convolutional, activation, drop-out, flattening, dense, and reshaping layers (Fig. 4.4). Initially, the network was trained without drop-out layers. However, since over-fitting was identified, 30% drop-out layers were incorporated into the architecture. A ReLu activation was performed after each convolutional layer. Sigmoid activation layers were performed after the dense layers. The last activation layer of the network varied depending on the implemented loss function. The architecture was slightly adjusted as the training process progressed.

During training, the sinogram was forwarded to the first convolutional layer, which passed through all the remaining layers until a 128×128 image was produced. Poisson and Kullback-Leibler KLD loss functions (see Table 4.2 for the form of these functions) were used to compare the reconstructed image, $\hat{y}$, to the ground truth image, y. For the Poisson loss, a final ReLu activation layer was used. Training with the KLD loss required a final softmax activation layer as this loss assumes a normalized probability distribution. Of these loss functions, the KLD loss showed the

Loss function	Function $L(y, \hat{y})$
Poisson	$\frac{1}{n}\sum_i^n(\hat{y}_i - y_i log\, \hat{y}_i)$
KLD	$\frac{1}{n}\sum_i^n y_i log\, \frac{y_i}{\hat{y}_i}$

Table 4.2: Possion and KLD loss functions used to compare the network reconstruction $\hat{y}$ to the ground truth image y.

highest potential. Results from the Poisson loss are displayed in the Appendix.

During training, the weights were adjusted with an adaptive moment estimation (ADAM) optimizer. ADAM expands on the standard gradient descent method through adaptive estimates on first and second-order moments. The learning rate, η, and hyper-parameters, β_1 and β_2, were adjusted to ensure optimal network fitting.

The training was completed for the 200,000 training pairs in batch sizes of 32. Training on the entire set was repeated for 100 epochs. 50,000 sinogram-image pairs formed the validation set to monitor the network. After iterating through the entire training set in a single epoch, the validation set loss was calculated. During this calculation, no optimization was performed to ensure independence between the validation set and training process. The training and validation loss were found at each epoch to monitor under- and over-fitting.

4.2.2 Machine Learning Rod-parameter Detection

A similar CNN was designed to analyze radar time-domain sinograms. This section describes how the network was trained to reconstruct the rod information parameters. The rod-parameter array consisted of the two rods', x position, y position, reflectivity Γ, and radius r. The 250,000 sinogram-parameter pairs were split into 80/20 training and testing sets. Images were reconstructed from the network predictions for visualization purposes. The network predictions were compared to the ground truth parameters.

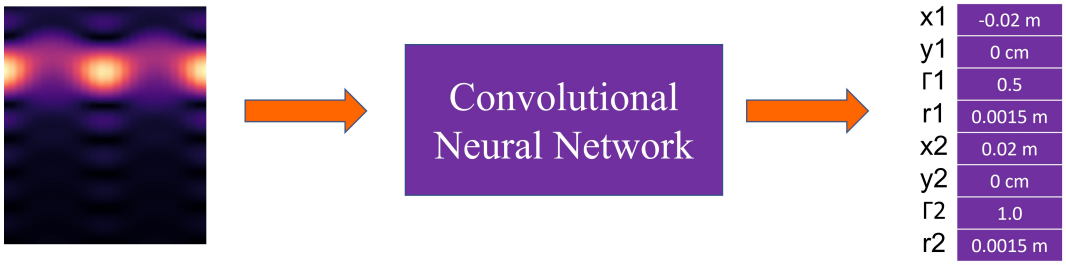

Figure 4.5: Convolutional neural network rod-parameter detection from time-domain sinograms.

Training and Testing Set Development

This section uses the same rod models and their corresponding radar sinograms from the previous section. However, instead of the Y output sets consisting of 128 $\times$ 128 reflectivity arrays, it consisted of 8 $\times$ 1 rod-parameter arrays. Specifically, the x position, y position, reflectivity Γ, and radius r were recorded for each rod. The positions were recorded in meters ranging from -0.1 to 0.1 m. The reflectivities were recorded as decimals ranging from 0.1 - 1.0. Each rod radius r was set to 0.0015 m, although, the rod size could be varied in the future. For data augmentation, the x and y positions were transformed mathematically. For θ rotation, the following transformation was performed:

$$x' = x\cos(\theta) - y\sin(\theta) \tag{4.1}$$

$$y' = x\sin(\theta) + y\cos(\theta) \tag{4.2}$$

For vertical flipping, the following was performed:

$$x' = x \tag{4.3}$$

$$y' = -y \tag{4.4}$$

Lastly for horizontal flipping, the following was performed:

$$x' = -x \tag{4.5}$$

$$y' = y \tag{4.6}$$

Similar to before, each unique rod-parameter model and their corresponding sinogram were randomly augmented twenty-five times to create 250,000 sinogram-parameter pairs.

Network Design and Training

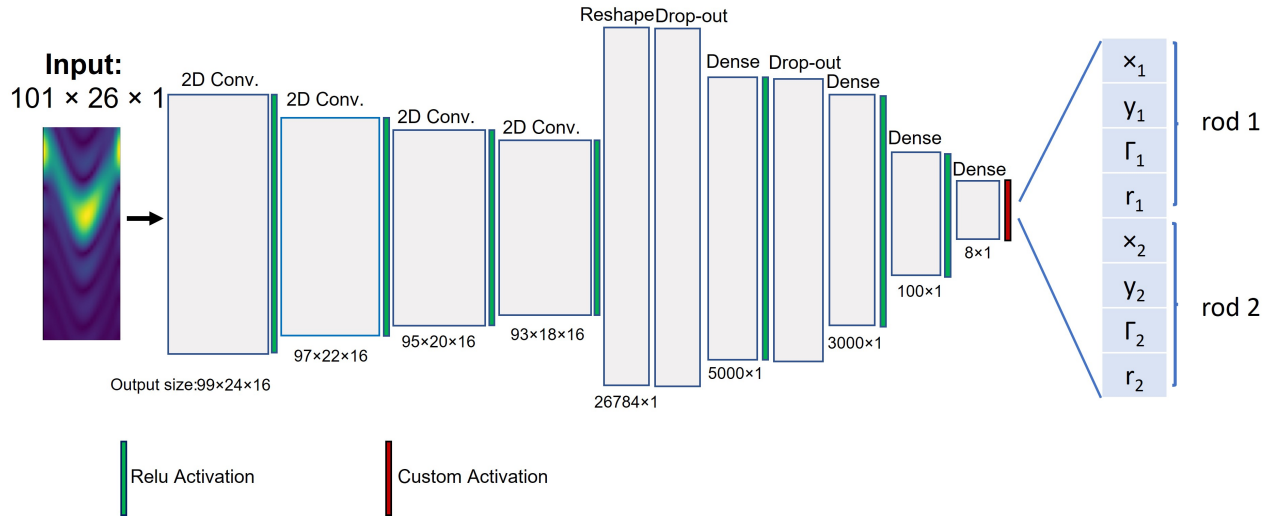

Figure 4.6: Convolutional neural network architecture for rod parameter reconstruction.

Loss function	Function $L(a,b)$
Mean Squared Error	$\frac{1}{n}\sum_i^n (a_i - b_i)^2$
Mean Absolute Error	$\frac{1}{n}\sum_i^n \lvert a_i - b_i \rvert$

Table 4.3: MSE and MAE loss functions used to compare the network parameter reconstruction to the ground truth parameters.

The CNN from the previous section was slightly modified to produce an 8×1 rod parameter array (Fig. 4.6). The network finishes with dense layers instead of convolutional ones. The network features a ReLu activation between most layers, with a final custom activation layer defined as a

sigmoid function ranging from -1 to 1:

$$f(x) = \frac{2}{1+e^{-x}} - 1 \tag{4.7}$$

This form of activation layer was used because the rod-parameter output features values within this range.

For this detection problem, regressive loss functions were used to compare the predicted neurons, a, to the ground truth neurons, b. Specifically, mean squared and absolute errors were investigated (Table 4.3). The ADAM optimizer was used to adjust the weights within the network. The training was completed using the entire training set for 100 epochs, and the training and validation losses were monitored at each training epoch.

4.2.3 Machine Learning Testing and Performance Evaluation

The performance of both machine learning networks were evaluated using the testing sets. For the image reconstruction network, the predicted reflectivity model was compared to the ground truth model. For the rod parameter network, each predicted parameter was individually compared to its corresponding ground truth. Four metrics were used to evaluate the performance: mean squared error (MSE), accuracy, sensitivity, and specificity.

For the image reconstruction network, the MSE was used to evaluate the prediction. The MSE was determined by subtracting the ground truth image (I) and the prediction (J) and summing over the squared difference for each pixel i,

$$\mathbf{MSE} = \frac{1}{N}\sum_{i=1}^{N}(I_i - J_i)^2 \tag{4.8}$$

where N is the total number of pixels in the images.

The accuracy, sensitivity, and specificity were determined for the rod parameter predictions.

For accuracy calculations, the rod locations and reflectivities were monitored:

- Correct Prediction - Correct location (within 1 cm) and reflectivity (within 10%) for both rods.
- False Prediction - Incorrect location or reflectivity of either rod.

The accuracy of the network prediction was given by:

$$\text{Accuracy} = \frac{\text{Correct}}{\text{Correct + False}} \tag{4.9}$$

The sensitivity and specificity were obtained using a positive response defined by the correct detection of the copper rod. Any other reflectivity was categorized as negative. When evaluating the predictions, four cases were present:

- True Positive (TP) - Correctly located (within 1 cm) the copper rod response when present.
- False Negative (FN) - Missed a copper rod when present.
- True Negative (TN) - Correctly identified a non-copper rod when no copper rod was present.
- False Positive (FP) - Incorrectly identified a copper rod response when no copper rod was present.

Therefore the number of copper rod responses is the sum of the TP and FN predictions, and the number of non-copper responses is the sum of the TN and FP predictions. The responses were categorized into one of the four cases with a variable reflectivity % threshold to determine the receiver operating characteristic (ROC) curves from the sensitivity and specificity:

$$\text{Sensitivity} = \frac{\text{TP}}{\text{TP + FN}} \tag{4.10}$$

$$\text{Specificity} = \frac{\text{TN}}{\text{TN + FP}} \tag{4.11}$$

4.3 Results and Discussion

4.3.1 Machine Learning Image Reconstruction

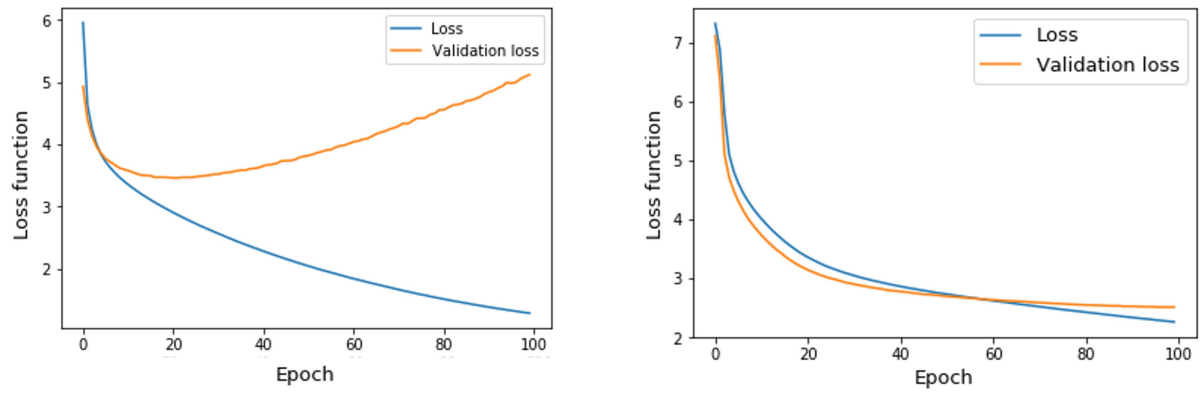

Figure 4.7: Training and validation loss using the default hyper-parameters without drop-out layers (left) and using η = 1e-5, β_1 = 0.88, β_2 = 0.98 with drop-out layers (right).

The KLD loss was the most promising training function. Hyper-parameters within the ADAM optimizer were varied to improve network performance. Initially, there were no drop-out layers, and the default parameters were used: η = 1e-3, β_1 = 0.9, β_2 = 0.999. However with this combination there was over-fitting within the network system (Fig. 4.7). Drop-out layers were added, and the learning rates were decreased. An optimal combination was found using the following parameters: η = 1e-5, β_1 = 0.88, β_2 = 0.98. With this new combination, both the training and validation losses decrease, following a similar pattern (Fig. 4.7).

After training 100 epochs, this network system was used to predict images from the testing set sinograms (Fig. 4.8). Overall, the network could locate the area of the point scatterers for both rod responses, but the rods were not well confined to the circular response regions. Also, for many predictions, the secondary reflectivity did not accurately represent the actual value. The hyper-parameters and network architecture were modified many times, without success, to try and obtain improved results.

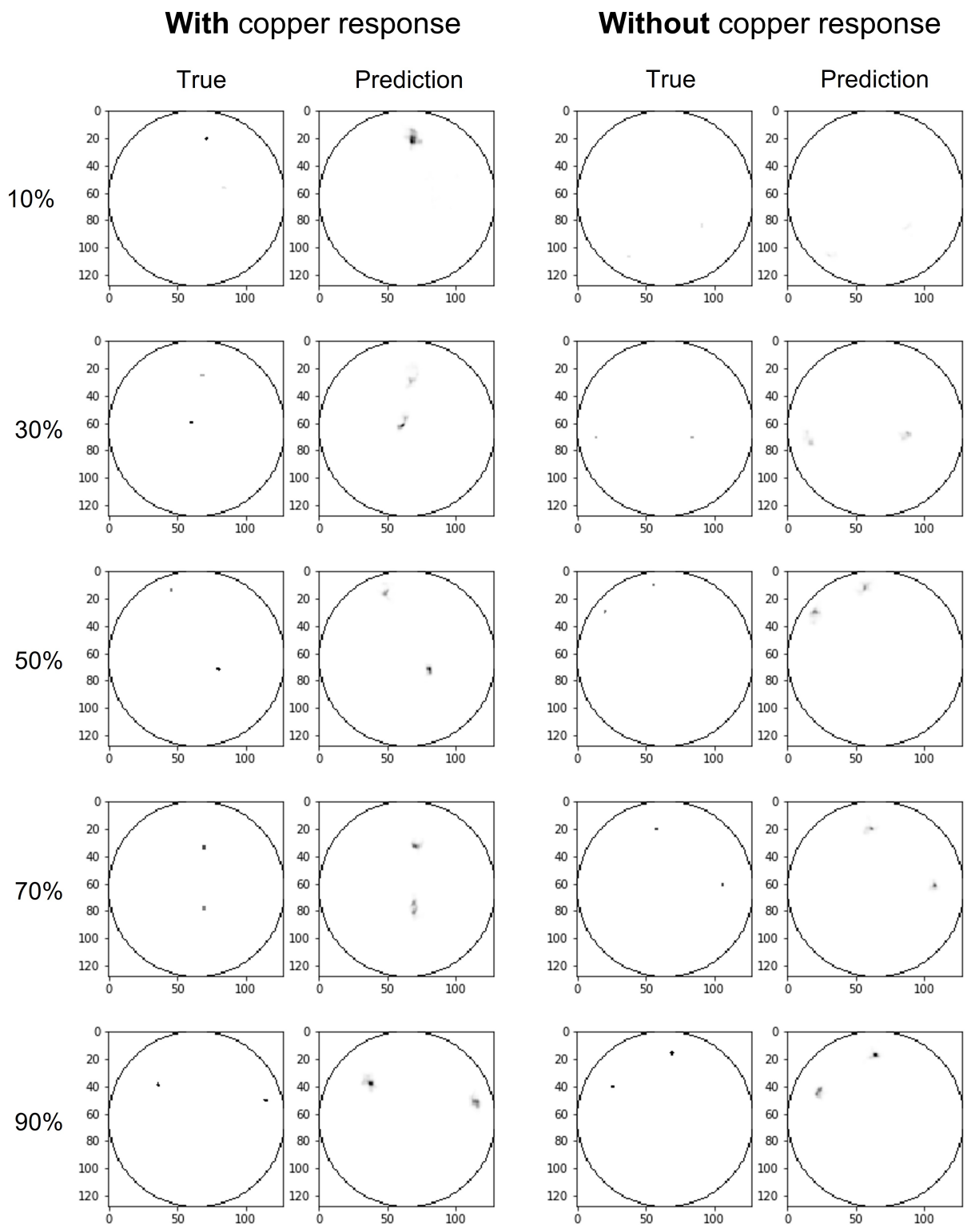

Figure 4.8: Machine learning prediction images and ground truth images for rods of different % reflectivity with and without the presence of a copper rod response.

Reflectivity Combination	MSE
10% and 100%	0.198
30% and 100%	0.127
50% and 100%	0.124
70% and 100%	0.119
90% and 100%	0.118
Total Set	0.137

Table 4.4: MSE calculated between the network predictions and ground truth rod models for various reflectivity combinations.

The MSE was calculated between the predictions and ground truth images for the different reflectivity values within the validation set. The MSE for each reflectivity is given in Table 4.4. The network had difficulty reconstructing the 10% reflectivity rods, especially in the presence of a copper rod. This is most likely because the copper reflection response over-powers the smaller reflectivity. In general, as the secondary reflectivity increased, the MSE improved. This implies that the network could reconstruct images better when the S_{11} reflections had higher reflectivities. This result could be due to a physical limitation in the resolving capabilities with this particular bandwidth, or a different loss function may be needed for this problem.

4.3.2 Machine Learning Rod-parameter Detection

The MAE loss produced the most accurate training results. The optimal performance occurred with the following hyper-parameters: η = 2e-5, β_1 = 0.9, β_2 = 0.999. The validation and training losses followed the same pattern, suggesting no over- or under-fitting (Fig. 4.10). The predicted and ground truth rod parameters were used to reconstruct images for visualization purposes (Fig. 4.9). In general, the network was able to detect and locate the copper response for any of the reflectivity combinations. However, the network had more difficulty locating the second-rod response, especially as the reflectivity decreased.

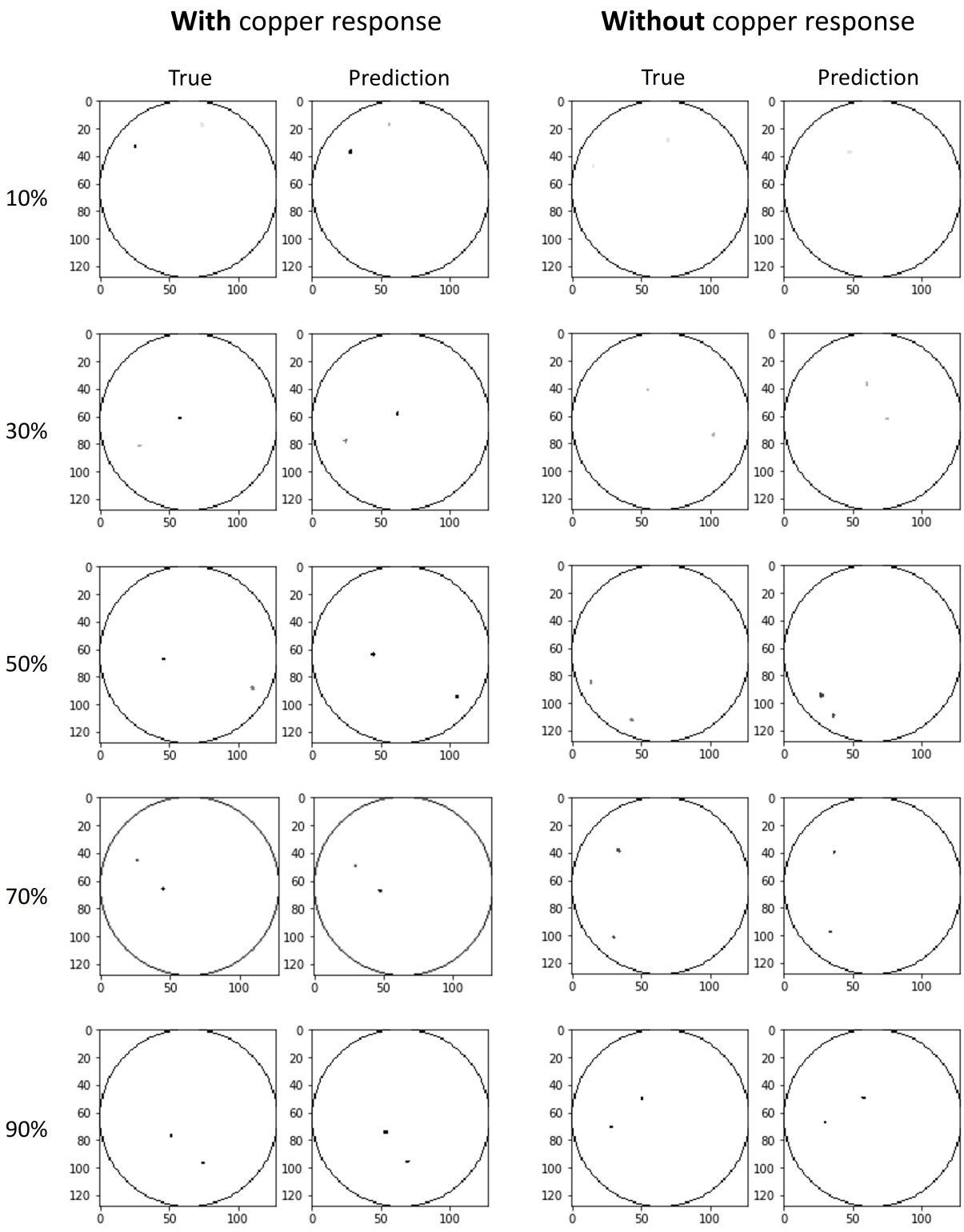

Figure 4.9: Machine learning rod-parameter predictions and true parameters were used to reconstruct images for visualization purposes.

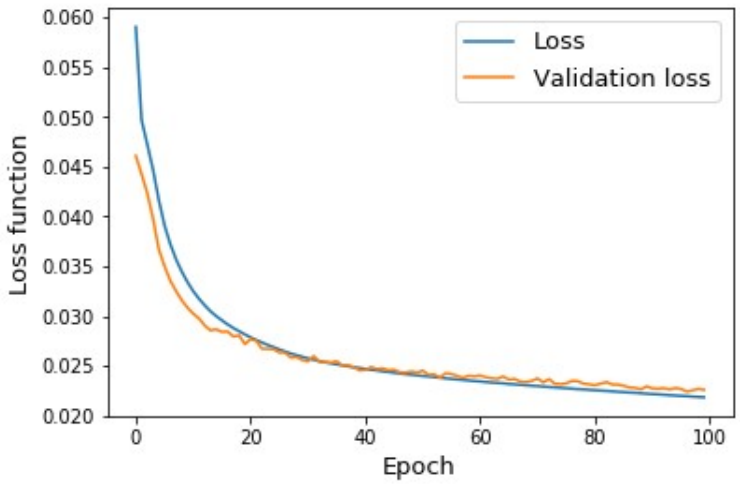

Figure 4.10: Training and validation MAE loss for rod-parameter reconstruction using η = 2e-5, $\beta_1 = 0.9$, $\beta_2 = 0.999$.

The rod-parameter values were used to calculate the accuracy, sensitivity, and specificity. To determine the accuracy of the prediction, the positions and reflectivities were given a 1.0 cm and 10% margin, respectively. A true prediction occurred if the prediction parameters agreed with the true parameters within these margins. A false prediction occurred if any of the parameters disagreed with the true parameters. The accuracy was calculated for each reflectivity combination (Table 4.5). For smaller reflectivities, the network performed poorly and could not locate the smaller secondary response. This is likely due to the small S_{11} signals that accompany lower reflectivities. The network could determine that a smaller reflectivity was present but could not accurately locate the scatterers. This was especially true when the copper rod was present, and the high reflectivity overpowered its lower counterpart.

The rod predictions without the copper response also performed poorly for the lower reflectivities. The network was often unable to determine the locations of the two rods' locations accurately. However, the network could easily locate the responses with 90% and 90% reflectivity models, which is mathematically similar to a 10% and 10% rod model, except scaled by a factor of one-ninth. Training the network with a wide range of reflectivities caused the network to favour higher signals.

Reflectivity Combination	Accuracy	Accuracy (with copper)	Accuracy (without copper)
10% and 100%	21%	32%	17%
30% and 100%	40%	46%	29%
50% and 100%	51%	48%	58%
70% and 100%	68%	85%	58%
90% and 100%	85%	92%	74%

Table 4.5: The accuracy calculated between the network predictions and ground truth rod-parameters for the entire set, those with a copper "positive" response, and those without.

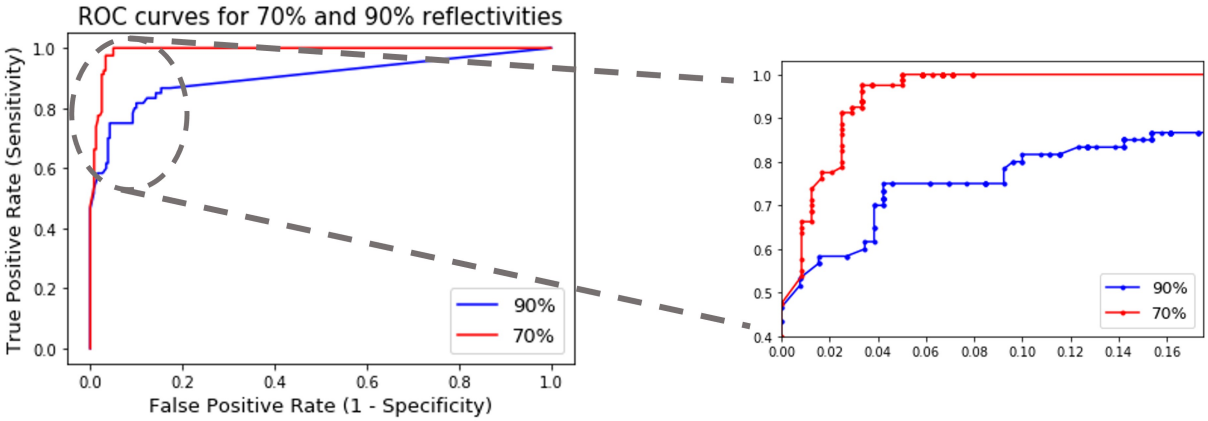

Figure 4.11: ROC curves for the testing sets using 70% reflectivities and 90% reflectivities.

The sensitivities and specificities were calculated for each rod response. In this situation, the copper rods correspond to a "positive" response, whereas the lower reflectivity rods correspond to a "negative" response. The network could distinguish a copper response from a lower reflectivity response for the 10%, 30%, and 50% rod models. Therefore, for a range of intensity thresholds, the network would predict with 100% sensitivity and 100% specificity. As the contrast between the copper and secondary rod decreased, the network had more difficulty distinguishing the reflectivity values. ROC curves were created for the 70% and 90% rod models by varying the threshold that defines a "positive" response from a "negative" response. The 70% reflectivity performed better in terms of its ROC curve. The 90% reflectivity had more difficulty distinguishing the 90% response from the 100% response because the values were within 10% of each other.

Overall, as the secondary reflectivity increased to 90%, the network performed better in terms of accuracy and MSE. However, at 90%, the ability to distinguish the two reflectivities worsened. In the presence of lower reflectivity rods, the network could accurately detect and locate the copper rod responses with 100% sensitivities. For the 10% and 100% model, the time-domain sinograms were similar to the expected sinogram from just a single rod response. Therefore, the copper rod response became more clearly defined as the effects from the second rod decreased. However, the network had difficulty locating the smaller reflectivity response.

4.4 Conclusion

A convolutional neural network was trained to detect the presence of rod objects. The radar model described in Chapter 3 was used to simulate time-domain sinograms from dual rod models. Each rod in the model was assigned one of the following reflectivities: 100% and m%. The second reflectivity m% was varied equally between: 10%, 30%, 50%, 70% and 90%. The 100% reflector was used to represent a copper rod. The contrast between the copper response and secondary response was varied to monitor the effects of this difference.

Two machine learning methods were used to detect and locate the rod responses. In the first method, a convolutional neural network was trained to reconstruct the rod reflectivity model directly from the time-domain sinograms. The second method used a similar convolutional neural network to produce the rod's positions, reflectivities, and sizes.

The convolutional neural networks detected and located the copper rod presence well for both methods. However, the networks, had difficulty identifying the response of the second rod, especially as the reflectivity decreased. The 10% and 30% reflectivity rods produced smaller S_{11} reflections, and the network had difficulty locating and reconstructing the actual intensity. However, the network readily located the copper rod responses with either training method. The network displayed promising results in its ability to locate rod responses within 1 cm for sensitivities as

high as 100%.

Artificial intelligence can be used to automate detection within the physical device. Analytical rod responses can be detected with a convolutional neural network. From here, transfer learning may be used to train with actual scans from the physical device described in Chapter 2. This process can be repeated with numerical and physical breast phantoms, and eventually human subjects. Using artificial intelligence, a portable breast microwave detection device can automate breast abnormality detection allowing women to screen themselves for a preliminary diagnosis.

5. Discussion and Conclusion

5.1 Summary and Discussion

Breast cancer affects millions of women worldwide, and in low- and middle-income countries (LMIC) the access to breast cancer screening is limited, resulting in relatively high mortality rates [5]. While x-ray mammography is widely used for breast cancer detection in developed countries, equipment cost and the lack of human resources and infrastructure in LMIC make it a less than ideal screening tool for marginalized communities. Mammography has a sensitivity of 63 - 95% [5], but sensitivities down to 48% are associated with high-density breasts, and 10-30% of breast cancer cases are not detected with mammography [8]. Mammography uses ionizing radiation that poses a health risk, and the risks and benefits must be balanced. Other breast imaging modalities, such as MRI, MBI and ultrasound, can be used to detect breast cancer, but all have limitations which make their use as a screening tool impractical, particularly in LMIC.

Microwave sensing measures reflected and transmitted microwave signals penetrating the breast and has shown promising results as a safe and low-cost breast cancer detection modality [16]. The microwave interactions depend on the dielectric properties of the breast. Cancerous lesions and fibroglandular breast tissue differ in their complex permittivity and morphology, providing a contrast of approximately 10%, which allows malignant tumours to be detected [17].

To create a compact system that is robust, easy to maintain and low cost, the device described in Chapter 2 uses a static (non-rotating) patch antenna array configured around a circular air cavity (no matching material) which encloses the pendant breast. Data is collected using a series of low-cost NanoVNAs attached to each antenna. Images of the breast can be reconstructed using an analytical radar reconstruction algorithm, such as the delay and sum beamformer (DAS), or

using machine learning approaches. Alternatively, machine learning can be used to diagnose the presence of a malignant lesion directly. Machine learning requires large training sets to obtain sufficient accuracy, and here a radar model may be used to simulate data more efficiently than experimental (or clinical) measurements.

This thesis hypothesizes that advances in microwave and machine learning technologies can be harnessed to create an early breast cancer detection device that is suited for use by women in remote and low-income locations. It sets out to design, develop, optimize and evaluate a prototype portable breast microwave detection device, investigate the feasibility of machine learning reconstruction using rods of different materials, and develop a radar model to facilitate transfer learning.

Chapter 2 focused on optimizing and characterizing the portable microwave system. To maximize the available bandwidth while keeping cost low, patch antennas that operate in the 0.7 – 3 GHz range were matched with a NanoVNA V2-2 with a bandwidth of 50kHz – 3 GHz. Ideally, many antennas should be used to increase the angular sampling, which will increase antenna coupling. To optimize the antenna array, the Envelope Correlation Coefficient (ECC) was calculated from S-parameter measurements. An optimal antenna spacing of 3 mm (26 antennas) was obtained, resulting in an acceptable ECC of less than 0.3 - 0.4.

The backbone of the device was 3D printed, and the antennas and VNA's were suitably mounted on the system. A USB hub provided power and computer communication to the VNAs, and the entire system was shielded with radar-absorbing material to minimize external interference. In contrast to the pre-clinical bed system that uses 72 S11 measurements over 2 - 9 GHz (fractional bandwidth = 1.64) [67], the portable system currently only uses 26 S11 measurements over 0.7 – 3 GHz (fractional bandwidth = 1.58,) which limits the image quality. However, when power measurements between all antennas are implemented, and improved NanoVNAs are installed, an additional 650 power measurements and S11 measurements over 0.7 to 4.4 GHz (fractional bandwidth = 2.01) will be possible at each frequency point. While the power measurements cannot be used directly with the DAS-type reconstructions, the power measurements may provide informa-

tion on attenuation and scattering magnitudes which are likely to be of value in machine learning approaches.

Further improvements can be made to the device design and equipment. Presently, all the antennas form an array in the same plane. For rod scans, shifts in the vertical plane do not affect measurements due to translational symmetry. However, for scans with breast phantoms, the vertical placement of the antennas can play an important role in tumour detection. To better localize lesions, measurements at different cross sections of the breast could be obtained by staggering or stacking the antennas vertically. As the NanoVNA technology improves, the dynamic range and bandwidth of the device will increase. In general, patch antennas at higher frequencies have smaller heights, so more can be stacked vertically. For future work, different patch antennas can be investigated to ensure optimal measurements regarding to size and bandwidth while minimizing equipment costs.

In Chapter 3, the characteristics of the portable device described in Chapter 2 were used to simulate radar measurements. A basic radar model was modified to incorporate multiple scattering, microwave attenuation, and spherical wave propagation. DAS reconstructions were performed on the simulated sinograms. The DAS reconstruction of a rod at [0cm, 0cm] was analyzed to determine the width of the response. The rod responses were, as anticipated, broad due to the 2.3 GHz absolute bandwidth. An intensity profile along the x-axis of the reconstructed image was fit to a Gaussian curve (Fig. 5.1). The standard deviation of this fit was 4.5 cm.

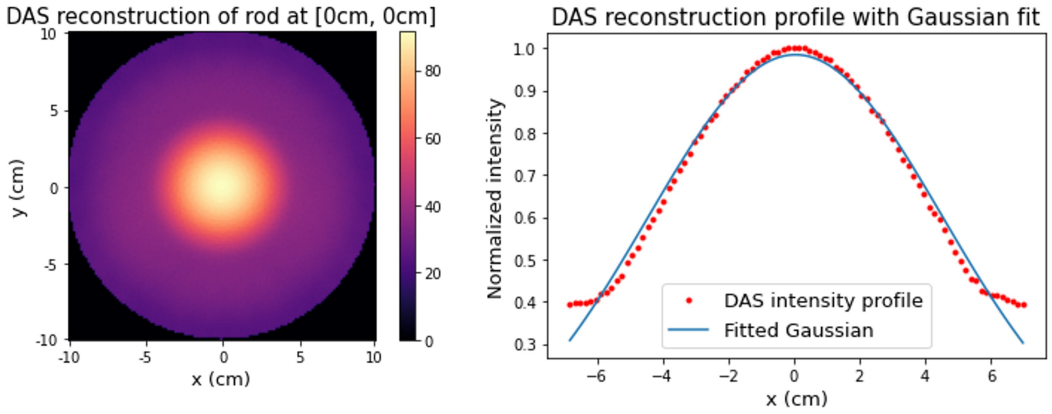

Figure 5.1: DAS reconstruction of the rod at [0cm, 0cm] with a Gaussian fit to the intensity profile along the central x-axis.

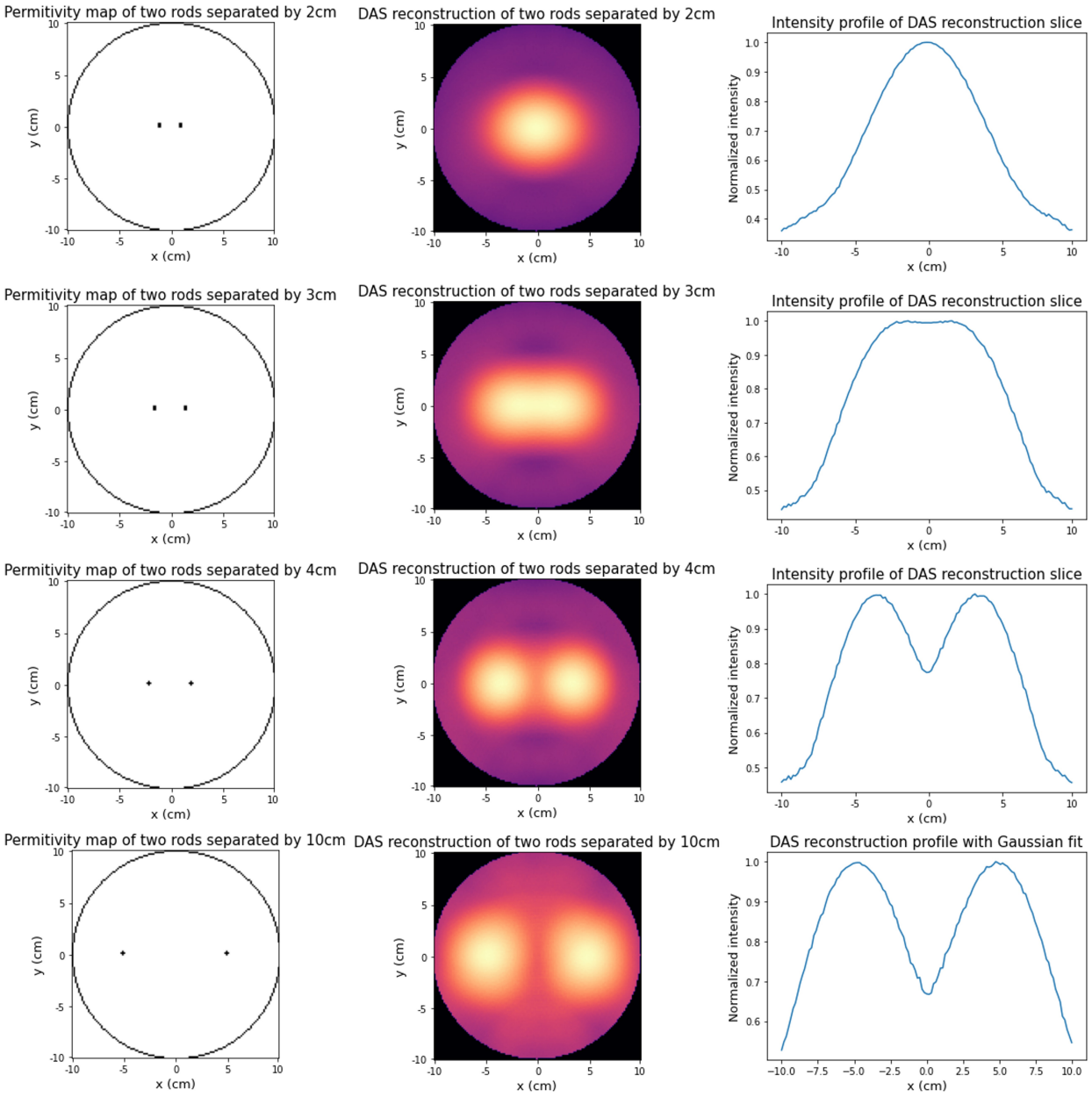

Figure 5.2: DAS image reconstructions and intensity profiles for various rod separations.

Similar simulations and DAS reconstructions were performed on two rods. The distance between the two rods was increased to monitor its ability to distinguish the point scatterers. Intensity profiles along the x-axis were plotted for rod separations of 2 cm, 3 cm, 4 cm, and 10 cm (Fig. 5.2). The two rods were indistinguishable when separated by 2 cm. Separating by 3 cm elongated the response, but it was impossible to distinguish the two scatterers. At 4 cm, the DAS reconstruction

separated the two responses. However, the peak maximums were located 3.3 cm off the central axis instead of 2 cm. At 10 cm, the network accurately separated and located the two responses. From this and the 4.5 cm response with one rod, it is clear that with the current bandwidth, it is difficult to resolve scatterers within 4 cm.

The agreement between the radar model and experiment could be improved by modifying the radar model to improve the accuracy of the simulation. Specifically, frequency dependant permittivity arrays, heterogeneity, antenna gain, and beam patterns can be modelled into the simulation. The secondary scatter component can also be re-modelled to fix assumptions on the scatterers. Improvements to the radar model will be essential to accurately represent measurements with complex breast phantoms.

In Chapter 4, machine learning techniques were used to locate rod responses. Numerical rod phantoms were created using two rods with variable reflectivities. A "positive" copper response was defined by 100% reflectivity, whereas the other rods reflectivities were assigned 10%, 30%, 50%, 70%, or 90%. The rod responses were located through direct image reconstruction and rod parameter detection. The machine learning network could detect and locate the copper rod responses with both methods and could locate the secondary 90% and 70% rod reflectivities better than the lower reflectivities. However, while the network could accurately distinguish the copper responses with the lower reflectivities, the network had difficulties distinguishing the 70% and 90% reflectivities in the presence of the copper rod.

Compared to the DAS reconstructions, these results are promising. For rod separations less than 4 cm, the DAS reconstructions could not distinguish the two responses. On the other hand, despite the narrow bandwidth, the machine learning reconstruction could locate rods as close as 1 cm. Although the network had difficulties locating the lower reflectivity responses, it could detect and locate 90% and 100% responses with an accuracy of 92%. Improving the training performance could increase this accuracy for the smaller reflectivity responses while using larger bandwidths could further improve detection and location accuracy.

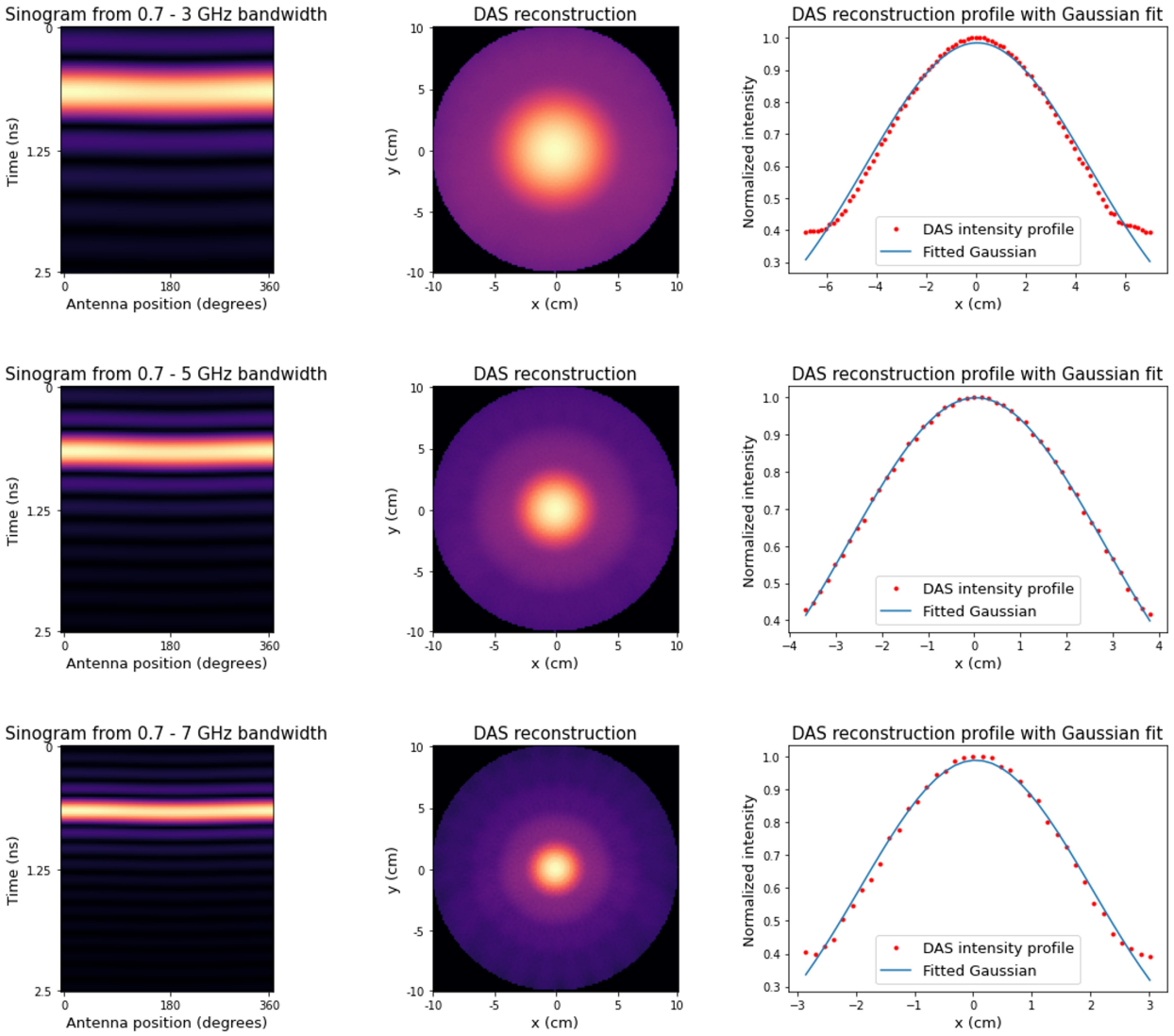

Figure 5.3: Time domain sinograms from a rod at [0cm, 0cm] and DAS reconstructions for different bandwidths.

Research into an optimal bandwidth could improve detection resolution and accuracy. For larger bandwidths, the width of the response decreases. This was tested using the radar model for the following frequency ranges: 0.7 - 3 GHz, 0.7 - 5 GHz, and 0.7 - 7 GHz. The corresponding sinograms, DAS reconstructions, and Gaussian fits are shown in Figure 5.3. The standard deviations of the responses were 4.5 cm, 2.8 cm, and 1.9 cm as the respective bandwidths increased. The radar model can perform similar simulations on complex breast phantoms. Higher frequency attenuation can be modelled by incorporating frequency dependant permittivity arrays. The results

for different bandwidths could be compared using machine learning detection to determine the optimal frequency range for the portable system.

Machine learning techniques could automate detection and localization for the portable device. The inexpensive equipment and small absolute bandwidth of the device make DAS reconstructions impractical due to resolving limitations. However, machine learning techniques were shown to improve the localization accuracy of point scatterers from radar simulated sinograms. Complex breast phantoms can be described as a non-linear sum of point scatterers. Therefore, a machine learning algorithm should improve upon the DAS reconstruction method when trained on complex phantoms. To train such a system would require large data sets. The radar model, with further improvements, could accurately simulate breast phantom sinograms. The simulated sinograms could initially train the network to detect the presence of a breast tumour. Transfer learning could then be applied on actual breast phantom scans from the improved physical device. Additionally, 650 power measurements can be recorded at each frequency. While power measurements are not useful for DAS reconstructions, these values could provide further scattering information for the machine learning algorithm. The DAS reconstruction method fails to incorporate physical aspects into the imaging process, however, a machine learning algorithm may improve the detection and localization accuracies by utilizing these physical aspects to gain more information on the scatterers.

5.2 Conclusion

Access to breast cancer screening should be equally available to all women. However, this is not currently the case due to high costs, lack of portability, and socioeconomic factors [5]. Lack of access to breast cancer screening in northern and First Nation communities in Canada [11] and LMIC [5] contribute to excessive mortality rates . The relatively inexpensive and compact equipment, promising contrast between healthy and cancerous tissue, and lack of ionizing radiation make microwave detection a suitable modality for breast cancer screening. This thesis hypothesized that advancements in microwave and machine learning technologies could be used for early breast can-

cer detection in remote and low-income areas. Three aims were completed to characterize and test this hypothesis.

In Chapter 2, a compact and inexpensive microwave detection device was assembled and characterized. Twenty-six patch antennas were mounted onto a 20 cm diameter cylinder. Each antenna was connected to its own NanoVNA to measure and record S-parameters. The antenna cable time delay and propagation speed were estimated using S_{11} measurements on copper rods. Currently, the device can scan S_{11} measurements from 0.7 - 3 GHz. However, improvements in the technology could increase the bandwidth. Additionally, power measurements may be recorded between any pair of antennas. This would increase the number of measured S-parameters by a factor of twenty-six. Increasing the number of signals recorded by the scatterer will expand our knowledge of the material's properties.

Chapter 3 modified a radar model to simulate realistic time-domain S_{11} data that the physical device would be measure. The model was used to simulate results for numerical rod and breast phantoms. DAS reconstructions were performed on the simulations revealing a single rod uncertainty of 4.5 cm and dual rod resolving distance of 4 cm for this particular bandwidth. The radar model could be further modified to incorporate other physical aspects of the microwave device. This could include heterogeneity, antenna gain and beam pattern, and frequency-dependent dielectric properties. Additionally, the simulator can be modified to model general S_{mn} sinograms. The radar model is crucial in developing accurate time-domain sinograms for machine learning purposes. For future work, numerical breast phantoms and their corresponding sinograms could be used to train a machine learning network to detect cancerous tissue. Scans from the physical device could be used to train the network to incorporate aspects from the actual measurements.

In Chapter 4, a machine learning network was trained to reconstruct images from simulated S_{11} data. Specifically, the network detected and located rods through direct image reconstruction and by producing the rod location and intensity parameters. Each rod model consisted of two rods with reflectivities between 10% to 100%. Both methods showed promising results in locating

point scatterers using the physical device bandwidth and antenna positions. The network could locate high scattering areas for rods with 100% reflectivities. The 90% and 100% rod models were detected and located with accuracies of 92%. These positions were detected for rods as close as 1 cm, improving on the DAS reconstruction resolving capabilities of 4.5 cm. However, the network struggled with the lower reflectivity rods. Modifications on how the problem is defined or investigation into alternative loss functions may be needed to increase the sensitivity of the network to lower reflectivities.

Future modifications to the small microwave device can be employed to improve the resolution and accuracy of measurements. Newer models of the NanoVNAs allow for improved dynamic range and larger bandwidths. Investigation into an optimal bandwidth can be performed using the radar model and machine learning techniques. The effects of improved resolution and increased attenuation could be modelled using frequency dependant permittivity arrays. The bandwidths could be varied to determine optimal frequencies for automated breast cancer detection. From here, optimal patch antennas could be carefully selected to improve performance while maintaining low equipment costs. Machine learning technologies can be used to automate and improve microwave sensing methods. Building on this research will further our knowledge and increase the demand for additional breast cancer screening methods. Through the design, testing, and optimization of a portable microwave sensing device, women in northern and First Nation communities in Canada and LMIC in the international community may have improved access to early breast cancer detection.

A. Appendix

The convolutional neural networks in Chapter 4 were trained many times with different architectures, loss functions, and hyper-parameters. Within this Appendix, there are some examples of network predictions that were not included in Chapter 4.

For the image reconstruction method, the KLD and Poisson loss functions were investigated. In general, the Poisson loss function did not perform well. Using default parameters, the network was not able to converge to a minimum (Fig. A.1). Each pixel predicted zero, likely because 99% of the true pixels are zero. For the KLD loss function, the learning rate played an important role with the reconstruction. Initially, there were no drop-out layers present. For the default learning rate (1e-3), the network was able to locate scatterers, but the shapes were irregular, the intensities were incorrect, and there was over-fitting present (Fig. A.2). Decreasing the learning rate to 1e-5 improved the quality of the reconstruction, however the validation loss was noisy (Fig. A.3). Further decreasing the learning rate to 1e-7 prevented the network to converge to a minimum and produced ring artifacts within the prediction (Fig. A.4). Following this, drop-out layers were used to address over-fitting, and the hyper-parameters were further optimized to improve network performance.

For the rod parameter detection method, the MSE and MAE loss functions were investigated. For the MSE loss, learning rate of 1e-4, batch size of 32, and no drop-out layers, there was over-fitting present and the network had difficulty locating the scatterers (Fig. A.5). For the MAE loss, many modifications to the network and hyper-parameters were made. For a learning rate of 1e-5, 40 batch size, and no drop-out layers, there was over-fitting present and the network had difficulty with the size and location of the scatterers (Fig. A.6). Lowering the learning rate to 5e-6, batch size to 32, and adding drop-out layers improved the validation loss and amount of over-fitting present,

however, the network still struggled to locate both rod responses (Fig. A.7).

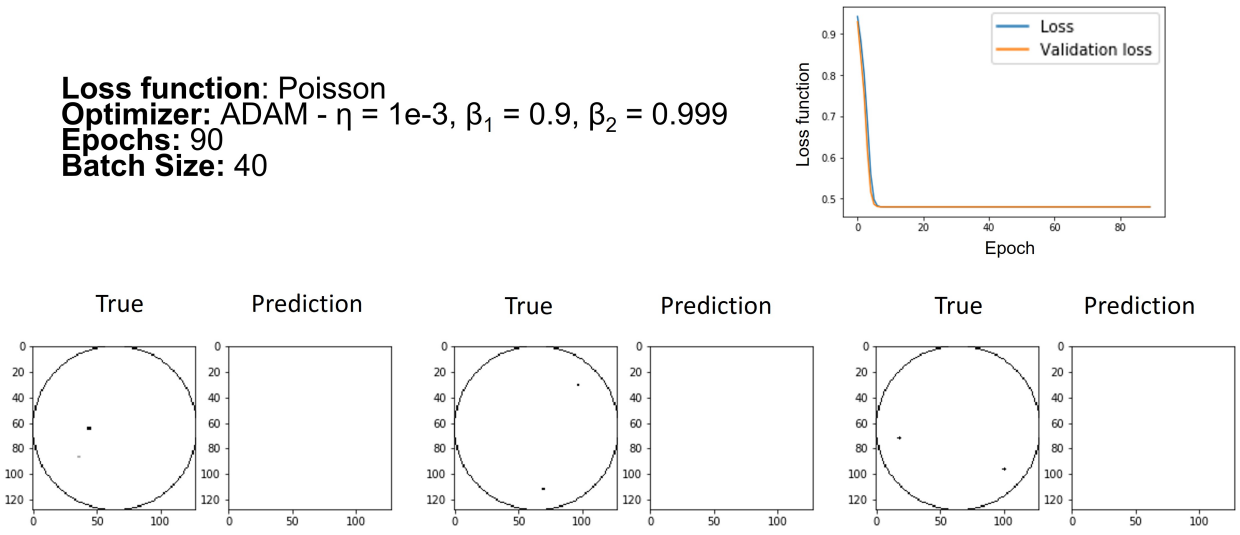

Figure A.1: Machine learning image reconstruction prediction with a Poisson loss function.

Loss function: Kullback Leibler Divergence
Optimizer: ADAM - η = 1e-3, β_1 = 0.9, β_2 = 0.999
Epochs: 100
Batch Size: 40

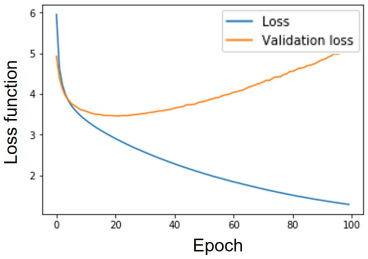

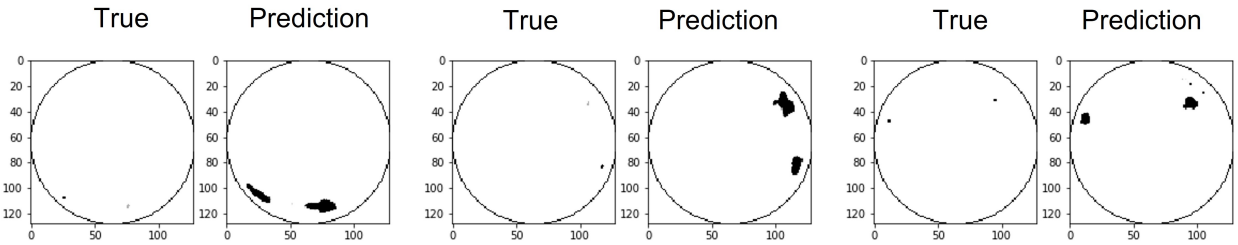

Figure A.2: Machine learning image reconstruction prediction with a KLD loss and 1e-3 learning rate.

Loss function: Kullback Leibler Divergence
Optimizer: ADAM - η = 1e-5, β_1 = 0.89, β_2 = 0.99
Epochs: 90
Batch Size: 32

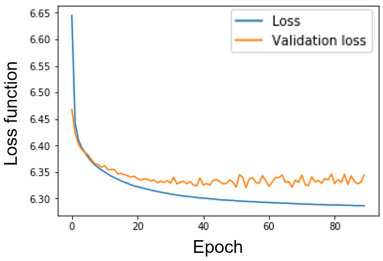

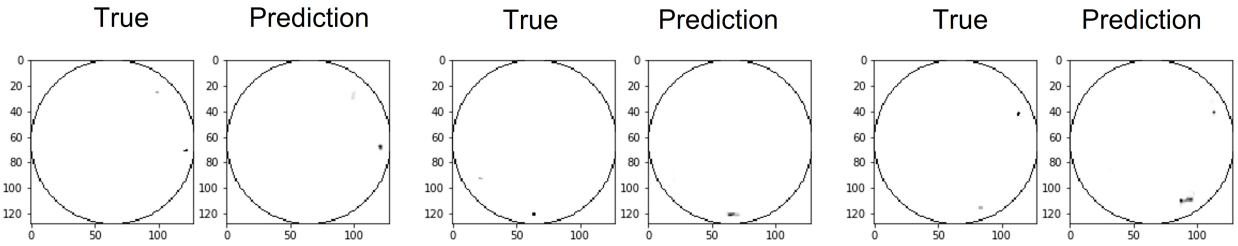

Figure A.3: Machine learning image reconstruction prediction with a KLD loss and 1e-5 learning rate.

Loss function: Kullback Leibler Divergence
Optimizer: ADAM - η = 1e-7, β_1 = 0.9, β_2 = 0.999
Epochs: 110
Batch Size: 32

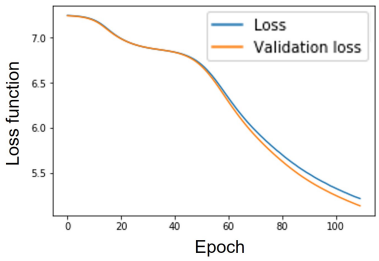

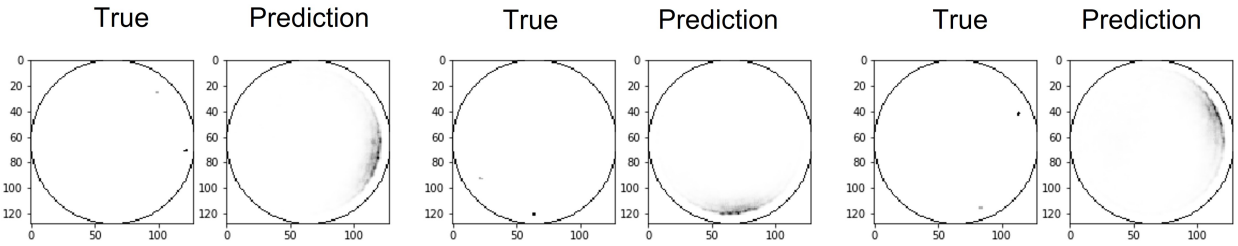

Figure A.4: Machine learning image reconstruction prediction with a KLD loss and 1e-7 learning rate.

Loss function: Mean Squared Error
Optimizer: ADAM - η = 1e-4, β_1 = 0.9, β_2 = 0.999
Epochs: 80
Batch Size: 32

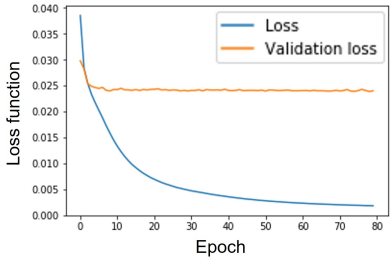

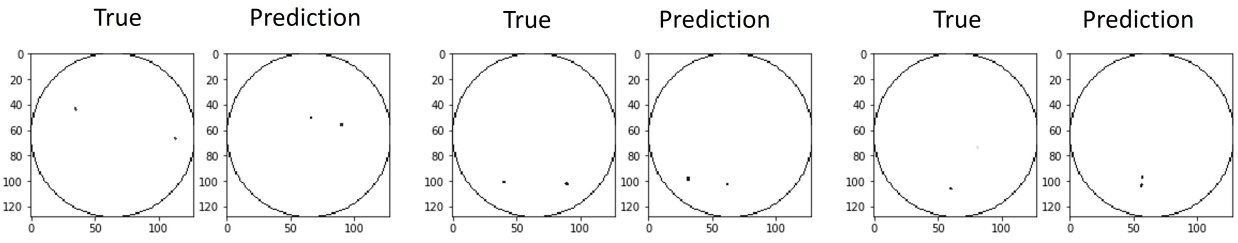

Figure A.5: Machine learning parameter prediction with a MSE loss and 1e-4 learning rate.

Loss function: Mean Absolute Error
Optimizer: ADAM - η = 1e-5, β_1 = 0.899, β_2 = 0.998
Epochs: 80
Batch Size: 40

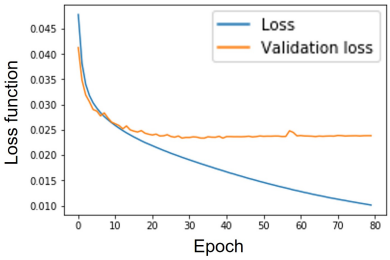

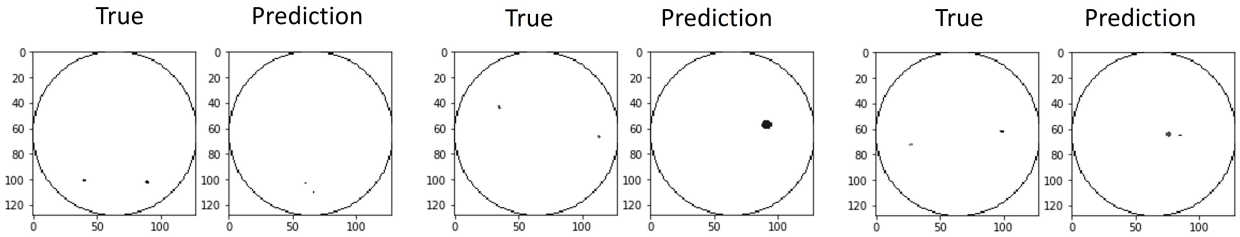

Figure A.6: Machine learning parameter prediction with a MAE loss and 1e-5 learning rate.

Loss function: Mean Absolute Error
Optimizer: ADAM - η = 5e-6, β_1 = 0.9, β_2 = 0.999
Epochs: 90
Batch Size: 32

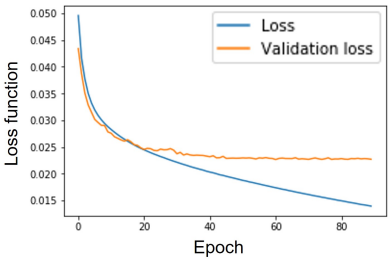

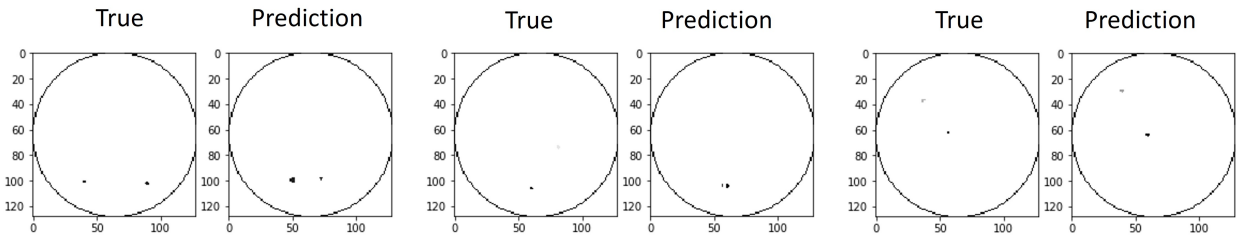

Figure A.7: Machine learning parameter prediction with a MAE loss and 5e-6 learning rate.

References

[1] K. S. Peairs, Y. Choi, R. W. Stewart, and H. F. Sateia, "Screening for breast cancer," *Seminars in Oncology*, vol. 44, pp. 60–72, 2 2017.

[2] V. Malek Pascha, L. Sun, R. Gilardino, and R. Legood, "Telemammography for breast cancer screening: a cost-effective approach in argentina," *BMJ Health Care Informatics*, vol. 28, p. e100351, 07 2021.

[3] L. A. Newman, "Breast cancer screening in low and middle-income countries," *Best Practice Research Clinical Obstetrics Gynaecology*, 2022.

[4] S. Dey, "Preventing breast cancer in lmics via screening and/or early detection: The real and the surreal," *World Journal of Clinical Oncology*, vol. 5, pp. 509–519, 08 2014.

[5] R. A. da Costa Vieira, G. Biller, G. Uemura, C. A. Ruiz, and M. P. Curado, "Breast cancer screening in developing countries," *Clinics*, vol. 72, pp. 244–253, 4 2017.

[6] L. Wang, H. Peng, and J. Ma, "Microwave breast imaging techniques and measurement systems," in *Breast Imaging* (A. M. Malik, ed.), ch. 4, Rijeka: IntechOpen, 2017.

[7] D. R. Brenner, A. Poirier, R. R. Woods, L. F. Ellison, J.-M. Billette, A. A. Demers, S. X. Zhang, C. Yao, C. Finley, N. Fitzgerald, N. Saint-Jacques, L. Shack, D. Turner, and E. Holmes, "Projected estimates of cancer in canada in 2022," *CMAJ*, vol. 194, no. 17, pp. E601–E607, 2022.

[8] A. Modiri, S. Goudreau, A. Rahimi, and K. Kiasaleh, "Review of breast screening: Toward clinical realization of microwave imaging," *Medical Physics*, vol. 44, pp. e446–e458, 12 2017.

[9] S. W. Duffy *et al.*, "Mammography screening reduces rates of advanced and fatal breast cancers: Results in 549,091 women," *Cancer*, vol. 126, no. 13, pp. 2971–2979, 2020.

[10] B. Elias, E. Kliewer, M. Hall, A. Demers, D. Turner, P. Martens, S. Hong, L. Hart, C. Chartrand, and G. Munro, "The burden of cancer risk in canada's indigenous population: a comparative study of known risks in a canadian region," *International journal of general medicine*, vol. 4, pp. 699–709, 10 2011.

[11] M. V. Mazereeuw, A. Yurkiewich, S. Jamal, C. Cawley, C. R. Jones, and L. D. Marrett, "Cancer risk factors and screening in first nations in ontario," *Health Promotion and Chronic Disease Prevention in Canada*, vol. 37, pp. 186–193, 2017.

[12] "Recommendations on screening for breast cancer in average-risk women aged 40–74 years," *CMAJ*, vol. 183, no. 17, pp. 1991–2001, 2011.

[13] L. Wang, "Early diagnosis of breast cancer," *Sensors (Switzerland)*, vol. 17, 7 2017.

[14] M. A. Aldhaeebi, K. Alzoubi, T. S. Almoneef, S. M. Bamatra, H. Attia, and O. M. Ramahi, "Review of microwaves techniques for breast cancer detection," *Sensors (Switzerland)*, vol. 20, 4 2020.

[15] D. O'Loughlin, M. O'Halloran, B. M. Moloney, M. Glavin, E. Jones, and M. A. Elahi, "Microwave breast imaging: Clinical advances and remaining challenges," *IEEE Transactions on Biomedical Engineering*, vol. 65, pp. 2580–2590, 11 2018.

[16] R. Conceicao, M. O'Halloran, and J. Mohr, *An Introduction to Microwave Imaging for Breast Cancer Detection*. Springer Cham, 07 2016.

[17] S. Semenov, "Microwave tomography: review of the progress towards clinical applications," *Philosophical transactions. Series A, Mathematical, physical, and engineering sciences*, vol. 367, pp. 3021–3042, 2009.

[18] A. Mashal, F. Gao, and S. C. Hagness, "Heterogeneous anthropomorphic phantoms with realistic dielectric properties for microwave breast imaging experiments," *Microwave and Optical Technology Letters*, vol. 53, no. 8, pp. 1896–1902, 2011.

[19] E. Porter, J. Fakhoury, R. Oprisor, M. Coates, and M. Popović, "Improved tissue phantoms for experimental validation of microwave breast cancer detection," in *Proceedings of the Fourth European Conference on Antennas and Propagation*, pp. 1–5, 2010.

[20] N. Joachimowicz, C. Conessa, T. Henriksson, and B. Duchêne, "Breast phantoms for microwave imaging," *Antennas and Wireless Propagation Letters, IEEE*, vol. 13, pp. 1333–1336, 12 2014.

[21] D. R. Herrera, T. Reimer, M. S. Nepote, and S. Pistorius, "Manufacture and testing of anthropomorphic 3d-printed breast phantoms using a microwave radar algorithm optimized for propagation speed," in *2017 11th European Conference on Antennas and Propagation (EUCAP)*, pp. 3480–3484, 2017.

[22] M. Abbak, M. Çayören, and I. Akduman, "Microwave breast phantom measurements with a cavity-backed vivaldi antenna," *IET Microwaves, Antennas & Propagation*, vol. 8, no. 13, pp. 1127–1133, 2014.

[23] E. Porter, H. Bahrami, A. Santorelli, B. Gosselin, L. A. Rusch, and M. Popovic, "A wearable microwave antenna array for time-domain breast tumor screening," *IEEE Transactions on Medical Imaging*, vol. 35, pp. 1501–1509, 6 2016.

[24] A. Ashtari, S. Noghanian, A. Sabouni, J. Aronsson, G. Thomas, and S. Pistorius, "Using a priori information for regularization in breast microwave image reconstruction," *IEEE Transactions on Biomedical Engineering*, vol. 57, pp. 2197–2208, 9 2010.

[25] J. D. Shea, P. Kosmas, S. C. Hagness, and B. D. Van Veen, "Three-dimensional microwave imaging of realistic numerical breast phantoms via a multiple-frequency inverse scattering technique," *Medical Physics*, vol. 37, no. 8, pp. 4210–4226, 2010.

[26] S.-H. Son, N. Simonov, H.-J. Kim, J.-M. Lee, and S.-I. Jeon, "Preclinical prototype development of a microwave tomography system for breast cancer detection," *ETRI Journal*, vol. 32, no. 6, pp. 901–910, 2010.

[27] T. Rubæk, P. M. Meaney, P. Meincke, and K. D. Paulsen, "Nonlinear microwave imaging for breast-cancer screening using gauss-newton's method and the cgls inversion algorithm," *IEEE Transactions on Antennas and Propagation*, vol. 55, pp. 2320–2331, 8 2007.

[28] P. Meaney, M. Fanning, T. Raynolds, C. Fox, Q. Fang, C. Kogel, S. Poplack, and K. Paulsen, "Initial clinical experience with microwave breast imaging in women with normal mammography," *Academic radiology*, vol. 14, pp. 207–18, 03 2007.

[29] L. Poli, G. Oliveri, and A. Massa, "Microwave imaging within the first-order born approximation by means of the contrast-field bayesian compressive sensing," *IEEE Transactions on Antennas and Propagation*, vol. 60, no. 6, pp. 2865–2879, 2012.

[30] J. Moll, T. Kelly, D. Byrne, M. Sarafianou, V. Krozer, and I. Craddock, "Microwave radar imaging of heterogeneous breast tissue integrating a-priori information," *International Journal of Biomedical Imaging*, vol. 2014, pp. Article ID 943549, 10 pages, 11 2014.

[31] M. Klemm, J. Leendertz, D. Gibbins, I. Craddock, A. Preece, and R. Benjamin, "Towards contrast enhanced breast imaging using ultra-wideband microwave radar system," in *2010 IEEE Radio and Wireless Symposium (RWS)*, pp. 516–519, 2010.

[32] J. M. Sill and E. Fear, "Tissue sensing adaptive radar for breast cancer detection—experimental investigation of simple tumor models," *Microwave Theory and Techniques, IEEE Transactions on*, vol. 53, pp. 3312 – 3319, 6 2005.

[33] D. Flores-Tapia and S. Pistorius, "Spatial sampling constraints on breast microwave radar scan acquired along circular scan geometries," in *Proceedings - International Symposium on Biomedical Imaging*, pp. 496–499, 2011.

[34] D. Flores-Tapia, O. Maizlish, and S. Pistorius, "Spatial sampling requirements for multistatic breast microwave radar imaging," in *Proceedings of the 2012 International Conference on Electromagnetics in Advanced Applications, ICEAA'12*, pp. 420–423, 2012.

[35] D. Byrne, M. Sarafianou, and I. J. Craddock, "Compound radar approach for breast imaging," *IEEE Transactions on Biomedical Engineering*, vol. 64, no. 1, pp. 40–51, 2017.

[36] M. Klemm, I. J. Craddock, J. A. Leendertz, A. Preece, D. R. Gibbins, M. Shere, and R. Benjamin, "Clinical trials of a uwb imaging radar for breast cancer," in *Proceedings of the Fourth European Conference on Antennas and Propagation*, pp. 1–4, 2010.

[37] E. C. Fear, J. Bourqui, C. Curtis, D. Mew, B. Docktor, and C. Romano, "Microwave breast imaging with a monostatic radar-based system: A study of application to patients," *IEEE Transactions on Microwave Theory and Techniques*, vol. 61, no. 5, pp. 2119–2128, 2013.

[38] W. Yiding, W. Yirong, and H. Jun, "Application of inverse chirp-z transform in wide-band radar," in *IGARSS 2001. Scanning the Present and Resolving the Future. Proceedings. IEEE 2001 International Geoscience and Remote Sensing Symposium (Cat. No.01CH37217)*, vol. 4, pp. 1617–1619 vol.4, 2001.

[39] E. Fear, X. Li, S. Hagness, and M. Stuchly, "Confocal microwave imaging for breast cancer detection: localization of tumors in three dimensions," *IEEE Transactions on Biomedical Engineering*, vol. 49, no. 8, pp. 812–822, 2002.

[40] H. Been Lim, N. Thi Tuyet Nhung, E.-P. Li, and N. Duc Thang, "Confocal microwave imaging for breast cancer detection: Delay-multiply-and-sum image reconstruction algorithm," *IEEE Transactions on Biomedical Engineering*, vol. 55, no. 6, pp. 1697–1704, 2008.

[41] M. Klemm, I. Craddock, J. Leendertz, A. Preece, and R. Benjamin, "Improved delay-and-sum beamforming algorithm for breast cancer detection," *International Journal of Antennas and Propagation*, vol. 2008, 01 2008.

[42] B. J. Erickson, P. Korfiatis, Z. Akkus, and T. L. Kline, "Machine learning for medical imaging," *RadioGraphics*, vol. 37, no. 2, pp. 505–515, 2017. PMID: 28212054.

[43] E. Çallı, E. Sogancioglu, B. van Ginneken, K. G. van Leeuwen, and K. Murphy, "Deep learning for chest x-ray analysis: A survey," *Medical Image Analysis*, vol. 72, p. 102125, 2021.

[44] A. S. Lundervold and A. Lundervold, "An overview of deep learning in medical imaging focusing on mri," *Zeitschrift für Medizinische Physik*, vol. 29, no. 2, pp. 102–127, 2019. Special Issue: Deep Learning in Medical Physics.

[45] L. Shen, L. Margolies, J. Rothstein, E. Fluder, R. McBride, and W. Sieh, "Deep learning to improve breast cancer detection on screening mammography," *Scientific Reports*, vol. 9, pp. 1–12, 08 2019.

[46] M. A. Aldhaeebi, T. S. Almoneef, A. Ali, Z. Ren, and O. M. Ramahi, "Near field breast tumor detection using ultra-narrow band probe with machine learning techniques," *Scientific Reports*, vol. 8, 12 2018.

[47] H. Dhahri, E. Al Maghayreh, A. Mahmood, W. Elkilani, and M. Faisal, "Automated breast cancer diagnosis based on machine learning algorithms," *Journal of healthcare engineering*, vol. 2019, p. 4253641, 11 2019.

[48] R. Conceicao, H. Medeiros, D. Godinho, M. O'Halloran, D. Rodriguez-Herrera, D. Flores-Tapia, and S. Pistorius, "Classification of breast tumour models with a prototype microwave imaging system," *Medical Physics*, vol. 47, 02 2020.

[49] R. Yamashita *et al.*, "Convolutional neural networks: an overview and application in radiology," *Insights Imaging*, vol. 9, 2018.

[50] S. Anwar *et al.*, "Medical image analysis using convolutional neural networks: A review," *J. Med. Syst.*, vol. 42, 2018.

[51] D. P. Kingma and J. Ba, "Adam: A method for stochastic optimization," *CoRR*, vol. abs/1412.6980, 2015.

[52] S. J. Pan and Q. Yang, "A survey on transfer learning," *IEEE Transactions on Knowledge and Data Engineering*, vol. 22, pp. 1345–1359, 2010.

[53] N. R. Epstein, P. M. Meaney, and K. D. Paulsen, "3d parallel-detection microwave tomography for clinical breast imaging.," *The Review of scientific instruments*, vol. 85 12, p. 124704, 2014.

[54] P. Meaney, M. Fanning, D. Li, S. Poplack, and K. Paulsen, "A clinical prototype for active microwave imaging of the breast," *IEEE Transactions on Microwave Theory and Techniques*, vol. 48, no. 11, pp. 1841–1853, 2000.

[55] S. Semenov, R. Svenson, A. Bulyshev, A. Souvorov, A. Nazarov, Y. Sizov, A. Pavlovsky, V. Borisov, B. Voinov, G. Simonova, A. Starostin, V. Posukh, G. Tatsis, and V. Baranov, "Three-dimensional microwave tomography: experimental prototype of the system and vector born reconstruction method," *IEEE Transactions on Biomedical Engineering*, vol. 46, no. 8, pp. 937–946, 1999.

[56] S. Semenov, J. Kellam, Y. Sizov, A. Nazarov, T. Williams, B. Nair, A. Pavlovsky, V. Posukh, and M. Quinn, "Microwave tomography of extremities: 1. dedicated 2d system and physiological signatures," *Physics in medicine and biology*, vol. 56, pp. 2005–17, 03 2011.

[57] K.-C. Kwon, Y.-T. Lim, C. Kim, N. Kim, C. Park, K.-H. Yoo, S.-H. Son, and S.-I. Jeon, "Microwave tomography analysis system for breast tumor detection," *Journal of medical systems*, vol. 36, pp. 1757–67, 06 2011.

[58] C. Gilmore, P. Mojabi, A. Zakaria, M. Ostadrahimi, C. Kaye, S. Noghanian, L. Shafai, S. Pistorius, and J. LoVetri, "A wideband microwave tomography system with a novel frequency selection procedure," *IEEE Transactions on Biomedical Engineering*, vol. 57, no. 4, pp. 894–904, 2010.

[59] M. Asefi, M. Ostadrahimi, A. Zakaria, and J. LoVetri, "A 3-d dual-polarized near-field microwave imaging system," *Microwave Theory and Techniques, IEEE Transactions on*, vol. 62, pp. 1790–1797, 08 2014.

[60] C. Gilmore, A. Zakaria, S. Pistorius, and J. LoVetri, "Microwave imaging of human forearms: Pilot study and image enhancement," *International journal of biomedical imaging*, vol. 2013, p. 673027, 01 2013.

[61] V. Khoshdel, M. Asefi, A. Ashraf, and J. LoVetri, "Full 3d microwave breast imaging using a deep-learning technique," *Journal of Imaging*, vol. 6, no. 8, 2020.

[62] M. Klemm, I. J. Craddock, J. A. Leendertz, A. Preece, and R. Benjamin, "Radar-based breast cancer detection using a hemispherical antenna array—experimental results," *IEEE Transactions on Antennas and Propagation*, vol. 57, no. 6, pp. 1692–1704, 2009.

[63] T. Henriksson, M. Klemm, D. Gibbins, J. Leendertz, T. Horseman, A. W. Preece, R. Benjamin, and I. J. Craddock, "Clinical trials of a multistatic uwb radar for breast imaging," in *2011 Loughborough Antennas Propagation Conference*, pp. 1–4, 2011.

[64] J. Bourqui, J. M. Sill, and E. C. Fear, "A prototype system for measuring microwave frequency reflections from the breast," *Journal of Biomedical Imaging*, vol. 2012, jan 2012.

[65] E. Porter, E. Kirshin, A. Santorelli, M. Coates, and M. Popović, "Time-domain multistatic radar system for microwave breast screening," *IEEE Antennas and Wireless Propagation Letters*, vol. 12, pp. 229–232, 2013.

[66] A. Santorelli, M. Chudzik, E. Kirshin, E. Porter, A. Lujambio, I. Arnedo, M. Popovic, and J. Schwartz, "Experimental demonstration of pulse shaping for time-domain microwave brest imaging," *Progress In Electromagnetics Research*, vol. 133, pp. 309–329, 01 2013.

[67] M. Solis-Nepote, T. Reimer, and S. Pistorius, "An air-operated bistatic system for breast microwave radar imaging: Pre-clinical validation," in *2019 41st Annual International Conference of the IEEE Engineering in Medicine and Biology Society (EMBC)*, pp. 1859–1862, 2019.

[68] T. A. Reimer, "Improving image reconstruction and machine learning methods in breast microwave sensing," Master's thesis, University of Manitoba, 2020.

[69] T. Reimer, M. Solis, and S. Pistorius, "The application of an iterative structure to the delay-and-sum and the delay-multiply-and-sum beamformers in breast microwave imaging," *Diagnostics*, vol. 10, p. 411, 06 2020.

[70] A. Baran, D. Kurrant, A. Zakaria, E. Fear, and J. LoVetri, "Breast imaging using microwave tomography with radar-based tissue-regions estimation," *Progress In Electromagnetics Research*, vol. 149, pp. 161–171, 01 2014.

[71] NanoVNA, "Very tiny handheld vector network analyzer." https://nanovna.com/.

[72] NanoRFE, "Nanovna v2." https://nanorfe.com/nanovna-v2.html.

[73] S. Blanch, J. Romeu, and I. Corbella, "Exact presentation of antenna system diversity performance from input parameter description," *Electronics Letters*, vol. 39, pp. 705 – 707, 06 2003.

[74] M. Klemm, J. A. Leendertz, D. Gibbins, I. J. Craddock, A. Preece, and R. Benjamin, "Microwave radar-based breast cancer detection: Imaging in inhomogeneous breast phantoms," *IEEE Antennas and Wireless Propagation Letters*, vol. 8, pp. 1349–1352, 2009.

[75] R. Nilavalan, A. Gbedemah, I. Craddock, X. Li, and S. Hagness, "Numerical investigation of breast tumour detection using multi-static radar," *Electronics Letters*, vol. 39, pp. 1787–1789, 01 2004.

[76] T. Reimer and S. Pistorius, "An optimization-based approach to radar image reconstruction in breast microwave sensing," *Sensors*, vol. 21, no. 24, 2021.

[77] M. Converse, E. Bond, B. Veen, and C. Hagness, "A computational study of ultra-wideband versus narrowband microwave hyperthermia for breast cancer treatment," *IEEE Transactions on Microwave Theory and Techniques*, vol. 54, no. 5, pp. 2169–2180, 2006.

[78] V. Komarov, S. Wang, and J. Tang, "Permittivity and measurement," *Encyclopedia of RF and Microwave Engineering*, pp. 3693–3711, 01 2005.

[79] S.-Y. Huang, J. M. Boone, K. Yang, N. J. Packard, S. E. McKenney, N. D. Prionas, K. K. Lindfors, and M. J. Yaffe, "The characterization of breast anatomical metrics using dedicated breast ct," *Medical Physics*, vol. 38, no. 4, pp. 2180–2191, 2011.

[80] J. Cui, K. Gong, N. Guo, C. Wu, X. Meng, K. Kim, K. Zheng, Z. Wu, L. Fu, B. Xu, Z. Zhu, J. Tian, H. Liu, and Q. Li, "Pet image denoising using unsupervised deep learning," *European Journal of Nuclear Medicine and Molecular Imaging*, vol. 46, 12 2019.

[81] I. Häggström, C. R. Schmidtlein, G. Campanella, and T. J. Fuchs, "Deeppet: A deep encoder–decoder network for directly solving the pet image reconstruction inverse problem," *Medical Image Analysis*, vol. 54, pp. 253–262, 2019.

[82] G. Fontaine., P. Lindstrom., and S. Pistorius., "Neural network pet reconstruction using scattered data in energy-dependent sinograms," in *Proceedings of the 15th International Joint Conference on Biomedical Engineering Systems and Technologies - BIOIMAGING,*, pp. 35–42, INSTICC, SciTePress, 2022.

[83] B. Zhu, J. Z. Liu, B. R. Rosen, and M. S. Rosen, "Image reconstruction by domain transform manifold learning," *CoRR*, vol. abs/1704.08841, 2017.

[84] N. Koonjoo, B. Zhu, G. Bagnall, D. Bhutto, and M. Rosen, "Boosting the signal-to-noise of low-field mri with deep learning image reconstruction," *Scientific Reports*, vol. 11, 04 2021.

[85] X. Wang, J. Ma, P. Bhosale, J. J. Ibarra Rovira, A. Qayyum, J. Sun, E. Bayram, and J. Szklaruk, "Novel deep learning-based noise reduction technique for prostate magnetic resonance imaging," *Abdominal radiology (New York)*, vol. 46, p. 3378—3386, July 2021.